Measurement of the branching fractions of B0s → KShh decays in LHCb, insights on the CKM angle gamma and monitoring of the Scintillating Fibre Tracker for the LHCb upgrade

Thomas Grammatico

SORBONNE UNIVERSITÉ
École doctorale des Sciences de la Terre et de l'environnement et Physique de l'Univers, Paris (ED 560)

Laboratoire de Physique Nucléaire et de Hautes Énergies (LPNHE, UMR 7585)

Measurement of the branching fractions of $B^0_{(s)} \to K^0_S h^+ h^{(\prime)-}$ decays in LHCb, insights on the CKM angle γ, and monitoring of the Scintillating Fibre Tracker for the LHCb upgrade.

by

Thomas Grammatico

Submitted in fulfillment of the requirements for the degree of

Doctor of Philosophy

Supervised by Prof. Eli Ben-Haïm and Dr. Matthew Charles

Defended on the 27^{th} of January 2022 in front of the committee:

Prof.	Eli	Ben-Haïm	Supervisor
Dr.	Matthew	Charles	Supervisor
Prof.	François	Le Diberder	Referee
Prof	Tim	Gershon	
Dr.	Lydia	Roos	
Dr.	Justine	Serrano	Referee
Dr.	Keri	Vos	

Contents

Contents

Contents

Chapter I

Introduction

The Standard Model of particle physics describes the interactions of the elementary particles. Many of its predictions have now been confirmed to a great precision. With the first observation of the Anderson-Brout-Englert-Guralnik-Hagen-Higgs-Kibble-'t Hooft boson in 2012 by ATLAS [1] and CMS [2], the last missing piece in the Standard Model was found. At present, the model provides a satisfactory description of most of the observed phenomena. Although such a great success has been achieved, a few points indicate that the Standard Model is not the end of the story: it is rather an effective theory of a yet-unknown and more complete underlying theory. Hints pointing to the limitations of the Standard Model are, for example, the fact that it does not describe gravity or the lack of explanation for the mass of the fermions and their hierarchy. We could also cite the fact that the Standard Model alone cannot explain the matter/anti-matter asymmetry observed in the Universe.

In the last few years, anomalies have been observed in the lepton sector by BaBar [3], Belle [4] and LHCb [5]. In the Standard Model, electrons, muons and tau leptons, are subject to the electroweak interaction, which treats them identically, except for differences due to their different masses. This feature of the Standard Model is referred to as Lepton Flavour Universality. However, recent experimental results have indicated possible deviations from the expected behaviour. These "tensions" have been observed, for example, in the ratio $R_{D^{(*)}} = \frac{\mathcal{B}(B^+ \to D^{(*)}\tau^+\nu_\tau)}{\mathcal{B}(B^+ \to D^{(*)}\mu^+\nu_\mu)}$. The conjoint measurements of R_D and R_{D^*} have shown hints of Lepton -Flavour-Universality breaking at a level of about 3σ (see Ref. [6] for the latest HFLAV combination). The recent LHCb measurements of the ratios $R_{K^{*+}} = \frac{\mathcal{B}(B^+ \to K^{*+}\mu^+\mu^-)}{\mathcal{B}(B^+ \to K^{*+}e^+e^-)}$ and $R_{K^0_S} = \frac{\mathcal{B}(B^+ \to K^0_S\mu^+\mu^-)}{\mathcal{B}(B^+ \to K^0_S e^-e^+)}$ have been found to be individually consistent with the Standard-Model predictions at the 1.4 and 1.5σ

level, their combination at the 2σ level [7]. However, interestingly, results of these measurements, as well as those of similar ratios such as R_K and $R_{K^{*0}}$ [8], are all pointing to the same direction: a deficit in decays containing muons compared to those containing electrons [6]. Flavour physics thus continues to play a crucial role in the search for physics beyond the Standard Model.

Charmless 3-body decays of B mesons are dominated by diagrams with loops of virtual particles. Contribution from New-Physics particles in these loops could induce deviations from the Standard Model predictions. In this context, and in particular for the decays under study in this thesis work, *CP* asymmetries and CKM angles are possible quantities to measure in order to perform indirect search for physics beyond the Standard Model.

In Chap. II, I describe the theoretical and experimental contexts of charmless 3-body B-meson decay studies. This is the occasion to briefly remind how *CP* violation arises in the Standard Model in Sec. II.1, where I discuss the different sources of *CP*-violation in the Standard Model and the conditions under which they are enabled. In this subsection I also give a brief review of recent LHCb *CP*-violation studies. I illustrate *CP*-violation measurements by taking the example of the $B^0_s \to K^0_S K^+\pi^-$ amplitude analysis [9]. This amplitude analysis benefited of the results from the $K^0_S h^\pm h'^\mp$ study performed by LHCb with run 1 data [10].

Section II.2 describes how was the Cabbibo mechanism extended to a model with 3 quark families by Kobayashi and Masukawa, through what we know today as the CKM paradigm. I then explain what the unitarity triangle is. This subsection contains some of the prerequisites for the discussion about the extraction methods of the CKM angle γ. It is important to note that measuring the CKM angle β was a main motivation for the development of the first B factories, BaBar and BELLE. I discuss succinctly how this angle can be measured and on how charmless 3-body B-meson decays have contributed to its measurements.

When studying the decay amplitude of charmless 3-body decays of B mesons, more degrees of freedom are involved comparing to 2-body decays. It is convenient to study these decays in the Dalitz plane. In Sec. II.3, I briefly detail why and how charmless 3-body decays of B mesons are studied thanks to Dalitz-plane amplitude analyses. I also describe there the isobar formalism, which was developed to describe 3-body amplitudes by the sum of resonant and non-resonant contributions. I discuss the limitations of this model and possible alternatives. The LHCb collaboration compared alternative formalisms that allow to model the S-wave contribution in the amplitude analysis of the $B^+ \to \pi^+\pi^-\pi^+$ decay [11, 12]. Namely, these are the isobar model, the K-matrix formalism and a quasi-model independent approach. In this subsection

I also discuss the results of this amplitude analysis and the fact that for the most parts, the three approaches were leading to compatible results.

Chapter II ends with a short overview of γ extraction techniques, in Sec. II.4, where I explain how tree-level process are used to measure this quantity. The GLW method [13] suggests to extract γ from B mesons decaying to a charged kaon and a CP-eigenstate D meson. The ADS method [14] generalises the GLW method to cases where the D meson is not a CP eigenstate. In that situation, greater precision on γ can be achieved. Then, I discuss how γ can be extracted from charmless 3-body decays of B mesons. A method suggested by London et al. [15] proposes to extract γ by combining the amplitude analysis measurements from several charmless 3-body B-meson decays. In this subsection, I shortly detail the theoretical framework of my analysis work reported later on in Chap. III. On the one hand, the decay amplitudes of several charmless 3-body B-meson decays is expressed in term of the contributing diagrams, their relative strong phase and γ. On the other hand, it is possible to measure experimental observables from the amplitude analyses of decays of the type $B \to PPP$. They consist of the branching fractions, the direct and the indirect CP asymmetries. If there are more observables than theoretical parameters, it is possible to extract γ from a fit on one or several points in the Dalitz planes of the decays. This is the case under flavour SU(3) assumption, according to which several symmetry states of the amplitude can be build, such as the fully-symmetric and the fully antisymmetric states. I give a brief overview of the diagrammatic analyses of charmless 3-body B-meson decays. I also discuss the implications of the flavour SU(3) assumption.

Chapter III describes the extraction of the CKM-angle γ from charmless 3-body decays of B-mesons. This work is an extension of a study done by a past Ph.D. student, Emilie Bertholet [16], which was based on BaBar published amplitude analyses. It showed that with the fully-symmetric amplitude, the method developed by London et al. yields encouraging results. My contribution was to extend this study to the fully antisymmetric state. In Chap. III I give the specifications of the fully antisymmetric amplitude, detailing which decays contribute to it and how the related amplitude are expressed in terms of topologically distinct diagrams. I discuss the limitations of the fully antisymmetric state, and my attempts to deal with them. I then explain why, in the current situation, extracting γ from the fully antisymmetric amplitude was not feasible. One could expect the situation to improve with more precise descriptions of the decay amplitudes of the processes involved in the fully antisymmetric amplitude study. The LHCb collaboration could contribute to this in the future.

I present the LHCb detector in Chap. IV. The LHCb detector is a single-arm forward spectrometer. It has been specifically designed to study decays of

charmed and bottom particles. I present the LHCb's sub-detectors, their role and how they function. Track reconstruction and particle identification is also briefly described. The LHCb detector is well suited for the $K^0_S h^\pm h'^\mp$ analysis that I discuss in Chap. VI.

As I write these lines, run 3 of the LHC should start in a few months. It was preceded by a long shutdown, during which the LHCb collaboration took the opportunity to updgrade the detector. In Chapter V, I shortly describe the upgrade and detail the LPNHE contribution to the new tracking system. I start the chapter by briefly detailing the run 3 conditions and what motivated the upgrade. The LHCb group in LPNHE is involved in the development of the read-out system of the Scintillating Fiber Tracker (SciFi). I describe this work, and in particular my personal contribution to the development of an expert-level panel that will be used in LHCb's control room, and to the tracker calibration procedure.

I then discuss the $K^0_S h^\pm h'^\mp$ analysis in Chap. VI. This analysis consists in a measurements of the branching fractions of the decays of the type $B^0_{(s)} \to K^0_S h^\pm h'^\mp$. I detail in this section the online selection: a loose selection that is performed at the early stages of the studies in order to save CPU and disk space. This selection is composed by two stages of triggers and the stripping. I then detail the $K^0_S h^\pm h'^\mp$-specific selection that I designed to reduce as much as possible contributions from background events. This selection is composed of 2 multi-variate analyses. At one stage, topological variables are employed to discriminate signal events from combinatorial background events. At the other stage, contribution from mis-identified events is reduced by training a machine-learing tool on particle-identification variables. The multi-variate selections are expected to be correlated; I discuss the 2-dimensional optimisation that is performed to maximise the signal significance over the background contributions. Once the whole selection was applied, I performed a fit to the B-meson invariant mass distribution of the $K^0_S h^\pm h'^\mp$ decays. I fit 56 event categories in a simultaneous fit. The strategy of the fit and its results are detailed in Sec. VI.4. From the fit results, yields for the different categories can be extracted. The ratios of branching fractions relative to that of $B^0_d \to K^0_S \pi^+ \pi^-$ are deduced from the yields that is corrected thanks to the efficiency study in the Dalitz plane. Then, a systematic-uncertainties study is performed to account for systematical bias. The $K^0_S h^\pm h'^\mp$ analysis is related to the amplitude analyses of several of these decays. A few of them were already performed, and others, together with updates, are planned for the near future.

Chapter VII concludes this thesis. I summarise there the outcome of the various aspect of the work I performed during my PhD, and I discuss the

perspectives of the 3-body charmless B-physics studies.

Chapter II

The charmless three-body B-meson decays theoretical framework and experimental background

Flavour physics is a wide sector. We have there many opportunities to challenge the Standard Model and to look for new physics. *CP*-violation effects, CKM elements, branching fraction measurements, and tests for Lepton Flavour Universality are a few examples of the wide variety of the observables we can measure in order to probe for new physics. Studies of charmless decays of the B-meson consists of a part of these efforts.

The study of flavour physics in charmless 3-body B-meson decays allows many variables to be measured, from branching fractions to the resonant structure of the decay (via amplitude analyses). The $K^0_S h^+ h'^-$ study I present in this thesis has two major goals. First, it aims to update the branching fractions of the decays $B^0_{(s)} \to K^0_S h^+ h'^-$ by means of a simultaneous fit to the invariant mass spectra of the B mesons. From these fit results, we can also deduce the distribution of signal events over the Dalitz plane. These steps are necessary before we can move to the second goal: a future amplitude analysis. Describing the decay amplitude over the Dalitz plane is required to study in detail *CP* violation processes in 3-body decays, observe (in some cases for the first time) decays via known resonances, and measure their characteristics. I will cover in Sec. VI the experimental aspects of the measurement of the ratios of $K^0_S h^+ h'^-$ branching fractions.

At the beginning of this chapter I discuss the theoretical framework of charmless 3-body B-meson decay studies. I first discuss *CP* violation in the Standard Model. From the effective Hamiltonian of a neutral oscillating meson

I derive the expression of the evolution over time of this meson and then the expression of the time-dependent *CP* asymmetry. I then detail the different types of *CP* violation in the Standard Model and the conditions under which these effects can arise. I illustrate *CP*-violation effects and their measurements with an example concerning $K^0_S h^+ h'^-$ decays: *CP*-violation measurements in $B^0_s \to K^0_S K^+ \pi^-$ decays [9].

Next, I describe the CKM paradigm, starting with the Cabbibo angle concept before introducing the CKM matrix. I then give details on the unitarity triangle and define its angle. One of the first goals of the first generation of B factories was to measure the CKM angle β. As this is an important part of flavour physics, and 3-body charmless B-meson decay background, I provide a short overview of the theoretical framework and experimental results related to the measurements of the angle β.

I continue by discussing Dalitz-plot amplitude analyses. I then motivate the use of Dalitz plane in the context of three-body decays, and discuss how it is used in amplitude analyses. Decay amplitudes of 3-body processes are most commonly described with the isobar formalism. I introduce this model and then discuss its limitations. Taking the example of a recent LHCb study, the amplitude analysis of $B^+ \to \pi^+\pi^+\pi^-$ decays [11,12], I introduce alternatives to the isobar model, namely the K-matrix [17–19] formalism and a quasi-model-independent [20–24] approach. Amplitude analyses in the Dalitz plane are a central aspect of the phenomenological study that I performed concerning the CKM-angle γ, which is detailed in Sec. III.

I end this chapter by explaining how γ can be measured in tree and loop process in general. I give a short overview of the GLW [13] and ADS [14] methods. The GLW method was introduced to extract γ from B-meson decays to a neutral kaon and a D meson which decays to a *CP* eigenstate. The ADS method generalises it to the case where the D meson decay mode is not a *CP* eigenstate. Then, I discuss a method proposed by Bhattacharya, Imbeault and London [15] to extract γ from charmless 3-body decays of B mesons. There, I introduce the theoretical framework of the study detailed in Chap. III.

II.1 *CP* violation

In the Standard Model, *CP* violation can occur in electroweak processes. I detail in this section the various *CP*-violation effects with the example of a neutral meson, denoted $|P^0\rangle$.

The Hamiltonian describing the evolution over time of neutral mesons is

given by:

$$H = M - \frac{i}{2}\Gamma, \tag{II.1}$$

where M and Γ are 2x2 Hermitian matrices. We have

$$H = \begin{pmatrix} m_{11} - \frac{i}{2}\Gamma_{11} & m_{12} - \frac{i}{2}\Gamma_{12} \\ m_{21} - \frac{i}{2}\Gamma_{21} & m_{22} - \frac{i}{2}\Gamma_{22} \end{pmatrix} \tag{II.2}$$

CPT invariance tells us that $m_{11} = m_{22}$ and $\Gamma_{11} = \Gamma_{22}$. Using the fact that M and Γ are Hermitian matrices, we know that $m_{21} = m_{12}^*$ and $\Gamma_{21} = \Gamma_{12}^*$. The effective Hamiltonian is not Hermitian due to the presence of the Γ terms. In this scenario, the eigenstates are not orthogonal: the fact that the mesons can decay is embedded in the effective Hamiltonian.

Let the eigenstates of the Hamiltonian (Eq. II.1) be:

$$|P_L\rangle = p|P^0\rangle - q|\bar{P^0}\rangle \tag{II.3}$$

$$|P_H\rangle = p|P^0\rangle + q|\bar{P^0}\rangle \tag{II.4}$$

where $|q|^2 + |p|^2 = 1$. Here, L and H stands for light and heavy. Solving the eigenstate problem, we obtain the following relation:

$$\frac{q}{p} = \sqrt{\frac{M_{12}^* - \frac{i}{2}\Gamma_{12}^*}{M_{12} - \frac{i}{2}\Gamma_{12}}} \tag{II.5}$$

We can then express the eigenvalues of the effective Hamiltonian in terms of the matrix elements:

$$m_{1,2} - \frac{i}{2}\Gamma_{1,2} = M_{11} - \frac{i}{2}\Gamma_{11} \pm \frac{p}{q}(M_{12} - \frac{i}{2}\Gamma_{12}) \tag{II.6}$$

where $m_{1,2}$ and $\Gamma_{1,2}$ are the masses and widths of the eigenstates of the effective Hamiltonian. Next, we invert Eq. II.3 and Eq. II.4 to express the flavour states in terms of these states of well-defined mass and lifetime:

$$|P^0\rangle = \frac{1}{2p}(|P_H\rangle + |P_L\rangle) \tag{II.7}$$

$$|\bar{P^0}\rangle = \frac{1}{2p}(|P_H\rangle - |P_L\rangle) \tag{II.8}$$

The evolution over time of an eigenstate of the Hamiltonian is given by the Schrödinger equation [25]:

$$\frac{i\partial|P_{H,L}\rangle}{\partial t} = H|P_{H,L}\rangle = (m_{H,L} - \frac{i}{2}\Gamma_{H,L})|P_{H,L}\rangle \tag{II.9}$$

where $(m_{H,L} - \frac{i}{2}\Gamma_{H,L})$ are the eigenvalue corresponding to the eigenstates $|P_{H,L}\rangle$. The eigenfunction solutions to this equation are well known:

$$|P_L(t)\rangle = e^{-im_L t - \frac{1}{2}\Gamma_L t}|P_L(0)\rangle \tag{II.10}$$

$$|P_H(t)\rangle = e^{-im_H t - \frac{1}{2}\Gamma_H t}|P_H(0)\rangle \tag{II.11}$$

The evolution over time of the flavour eigenstates can then be deduced using Eq. II.7 and Eq. II.8:

$$|P^0(t)\rangle = f_+(t)|P^0\rangle + \frac{q}{p}f_-(t)|\bar{P^0}\rangle, \tag{II.12}$$

$$|\bar{P^0}(t)\rangle = f_+(t)|\bar{P^0}\rangle + \frac{p}{q}f_-(t)|P^0\rangle, \tag{II.13}$$

with

$$f_\pm(t) = \frac{1}{2}(e^{-im_L t}e^{-\frac{1}{2}\Gamma_L t}[1 \pm e^{-i\Delta m t}e^{-\frac{1}{2}\Delta\Gamma t}]). \tag{II.14}$$

In this equation we define Δm and $\Delta\Gamma$ as:

$$\Delta m = m_H - m_L, \Delta\Gamma = \Gamma_H - \Gamma_L. \tag{II.15}$$

Three sources of *CP* violation can arise. The *CP* symmetry can be violated in the decay, in the mixing or in the interference between the decay and the mixing. A time-dependent analysis is sensitive to all the *CP*-violation types. The time-dependent *CP* asymmetry is given by:

$$A_{CP}(t) = \frac{\Gamma_{|\bar{P^0}\rangle\to f}(t) - \Gamma_{|P^0\rangle\to f}(t)}{\Gamma_{|\bar{P^0}\rangle\to f}(t) + \Gamma_{|P^0\rangle\to f}(t)} = \frac{-C_f\cos(\Delta m t) + S_f\sin(\Delta m t)}{\cosh(\frac{\Delta\Gamma}{2}t) + A_f^{\Delta\Gamma}\sinh(\frac{\Delta\Gamma}{2}t)} \tag{II.16}$$

Defining $\lambda = \frac{q}{p}\frac{\bar{A}_f}{A_f}$, the *CP* violation in the decay is quantified by:

$$C_f = \frac{1 - |\lambda|^2}{1 + |\lambda|^2}. \tag{II.17}$$

Direct *CP* violation can be measured even when we integrate over time.

The *CP* violation in the interference between mixing and decay is quantified by:

$$S_f = \frac{2\Im(\lambda)}{1 + |\lambda|^2}. \tag{II.18}$$

and then we can define:

$$A_f^{\Delta\Gamma} = -\frac{2\Re(\lambda)}{1 + |\lambda|^2}. \tag{II.19}$$

I now detail the conditions under which each *CP*-violation type can occur.

II.1.1 The different types of *CP* violation

Direct *CP* violation in the decay occurs when the decay rate of a particle to a given final state differs from the decay rate of its antiparticle to the charge conjugate of the final state, i.e.:

$$\Gamma(P^0 \to f) \neq \Gamma(\bar{P^0} \to \bar{f}) \tag{II.20}$$

This situation occurs if there is a difference between the magnitudes of the amplitudes of these two decays, A_f and $\bar{A}_{\bar{f}}$. The main requirement for this to happen is that at least 2 diagrams should contribute to the decay. In that case we have:

$$\mathcal{A}_f = \mathcal{A}_1 e^{i(\phi_1+\delta_1)} + \mathcal{A}_2 e^{i(\phi_2+\delta_2)}, \tag{II.21}$$

$$\bar{\mathcal{A}}_{\bar{f}} = \mathcal{A}_1 e^{i(-\phi_1+\delta_1)} + \mathcal{A}_2 e^{i(-\phi_2+\delta_2)}, \tag{II.22}$$

The condition $|\mathcal{A}_f| \neq \left|\bar{\mathcal{A}}_{\bar{f}}\right|$ is fulfilled under the following conditions:

- The amplitudes $\mathcal{A}_1$ and $\mathcal{A}_2$ of both diagrams are not null
- The strong relative phases δ_1 and δ_2 are different

- The weak phases ϕ_1 and ϕ_2 are different

This type of *CP* violation is accessible to charged and neutral hadrons, including baryons.

Neutral meson oscillation is also a potential source of *CP* violation. In the case where the probability for $|P^0\rangle$ to oscillate into a $|\bar{P^0}\rangle$ is different from the opposite process, we are in presence of *CP* violation through mixing. This is possible if $\left|\frac{p}{q}\right| \neq 1$. This type of *CP* violation is not observed in B^0 oscillation as in that case, $\left|\frac{p}{q}\right| \sim 1$. It is the main source for *CP* violation in K^0 decays.

CP violation can also occur through interference between decay and mixing. If the final state f is a *CP* eigenstate, then it is accessible to both $|P^0\rangle$ and $|\bar{P^0}\rangle$. *CP* violation in the interference between the mixing and the decay can then happen if $\Im(\lambda) \neq 0$. We see from Eq. II.18 that $S_f \neq 0$ in that situation.

A practical case: the example of *CP*-violation measurements in $B_s^0 \to K_S^0 K^+\pi^-$ decays

The study of $B_s^0 \to K_S^0 K^+\pi^-$ decays performed by LHCb [9] is the first amplitude analysis of this mode. It is untagged and time-integrated. This analysis was performed on the data sample collected by LHCb during 2011 and 2012. This amplitude analysis benefited from the $K_S^0 h^+ h'^-$ study performed on Run 1 data [10]: the distribution of the signal events over the Dalitz plane is determined from the B-meson mass fit thanks to the ${}_s\mathcal{P}lot$ technique described in Sec VI.5. In this amplitude analysis, the final states $K_S^0 K^+\pi^-$ and $K_S^0 K^-\pi^+$ are studied separately but their amplitude models are fitted simultaneously. It is then possible to test for direct *CP* violation by comparing the amplitude model of the two final states. No significant *CP*-violation effects were observed in this study. With sufficient data, extending the analysis to a time-dependent and tagged study could bring valuable insights into *CP* violation of all types in $B_s^0 \to K_S^0 K^+\pi^-$ decays.

CP-violation effects are not the only measurements that can be performed in the studies of charmless 3-body decays. With studies growing in complexity, it is also possible to have access to CKM quantities.

II.2 CKM matrix

In 1963, Cabbibo introduced the concept of quark mixing [26]. This formalism was developed in order to preserve weak universality and to explain why strange mesons had a longer life time then expected. Analogously to what was exposed

previously in Sec. II.1, the Cabbibo angle was used to express mass eigenstates as a mixing of flavour eigenstates. We have:

$$d' = d\cos\theta_c + s\sin\theta_c, \tag{II.23}$$
$$s' = -d\sin\theta_c + s\cos\theta_c, \tag{II.24}$$

where d and s are the quark flavour eigenstates and d' and s' are the mass eigenstates. The quark mixing can also be expressed as a the rotation matrix between the basis of the mass eigenstates and the basis of the flavour eigenstates:

$$\begin{pmatrix} d' \\ s' \end{pmatrix} = \begin{pmatrix} \cos\theta_c & \sin\theta_c \\ -\sin\theta_c & \cos\theta_c \end{pmatrix} \begin{pmatrix} d \\ s \end{pmatrix}, \tag{II.25}$$

This 2x2 matrix has no irreducible complexe phase, and so the two-generation quark-mixing picture could not explain *CP* violation in weak decays. Hence, Kobayashi and Masukawa stated that three quark generations were necessary, when at that time only three quarks were known. They generalised the Cabbibo conception of quark mixing to the case of three quark generations [27]. The CKM matrix reads:

$$\begin{pmatrix} d' \\ s' \\ b' \end{pmatrix} = \begin{pmatrix} V_{ud} & V_{us} & V_{ub} \\ V_{cd} & V_{cs} & V_{cb} \\ V_{td} & V_{ts} & V_{tb} \end{pmatrix} \begin{pmatrix} d \\ s \\ b \end{pmatrix} \tag{II.26}$$

We should note that the CKM matrix is unitary:

$$V_{CKM}^{\dagger} V_{CKM} = V_{CKM} V_{CKM}^{\dagger} = 1. \tag{II.27}$$

The number of real parameters of the CKM matrix is $2n^2$ where n is the number of families of quarks. The number of free parameters is reduced by a few constraints. Taking into account CKM matrix unitarity and the fact that relative phases between the various quarks can be arbitrary, we are left with $(n-1)^2$ free parameters. With three families of quarks, four parameters are left free: we have three angles and one *CP*-violating phase (performing the same exercise for the two-generation case initially studied by Cabbibo, n=2, would give a single mixing angle, the Cabbibo angle, and no *CP*-violating complex phase.)

Unitarity triangle

As already mentioned, the CKM matrix is, in the Standard Model, unitary. We can derive nine relations from this fact. Six of the latter can be represented as a triangle in the complex plane. In the Standard Model, as already mentioned, there are three generations of quark and thus their coupling involves only one irreducible phase. This leads to the fact that each of the six unitarity triangles has the exact same area. *CP* violation is embed in the formalism if the triangle has a non zero area. Among the 6 existing unitarity triangles, the unitarity triangle has been chosen to contain B^0-meson transitions and oscillations:

$$V_{ud}V_{ub}^* + V_{cd}V_{cb}^* + V_{td}V_{tb}^* = 0 \tag{II.28}$$

This relation is related to THE unitarity triangle. In the complex plane, this triangle is described by CKM matrix elements and we can define its angles as:

$$\alpha = \phi_2 \equiv arg[-\frac{V_{td}V_{tb}^*}{V_{ud}V_{ub}^*}], \tag{II.29}$$

$$\beta = \phi_1 \equiv arg[-\frac{V_{cd}V_{cb}^*}{V_{td}V_{tb}^*}], \tag{II.30}$$

$$\gamma = \phi_3 \equiv arg[-\frac{V_{ud}V_{ub}^*}{V_{cd}V_{cb}^*}]. \tag{II.31}$$

The three angles, as well as the lengths of the sides of the triangle can be probed experimentally. The position of the vertex of the triangle, or whether the triangle closes or not, are to be checked when looking for New Physics. Indeed, in the presence of New Physics, the individual measurements of each of the CKM angles could be affected by additional contributions. The internal consistency of the CKM picture could be broken by these effects. The constraints on the CKM unitarity triangle in the $(\bar{\rho},\bar{\eta})$ plane are shown in Fig. II.1, where $\bar{\rho} + i\bar{\eta} = -\frac{V_{ud}V_{ub}^*}{V_{cd}V_{cb}^*}$.

I now discuss shortly one important aspect of flavour physics: the measurements of the CKM angle β. The CKM angle β can be extracted from $b \to c\bar{c}s$ transitions using the so-called golden decay modes. The term "golden" refers to the fact that in these decays, the signals are theoretically and experimentally clean and the fact that due to large branching ratios, large statistics are in general available. The most precise measurements of β have been achieved thanks to these channels. Most of the decays of this type are decays consisting of a charmonium and a neutral kaon in the final state and forming a *CP*

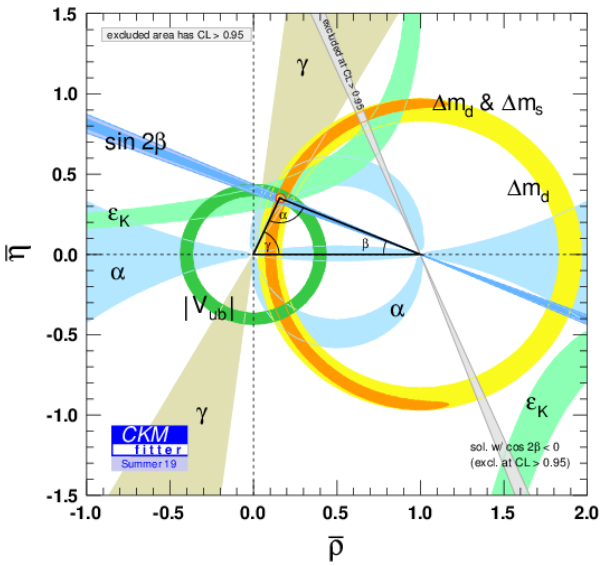

Figure II.1: Constraints on the CKM unitarity triangle in the ($\bar{\rho}$,$\bar{\eta}$) plane, produced by the CKM fitter collaboration [28].

eigenstate, such as $B^0 \to J/\psi K_s^0$, $B^0 \to \psi(2S)K_s^0$ or $B^0 \to \chi_{c1}K_s^0$. The CKM angle β describes *CP* violation in the interference between the decays, with or without oscillation. From Eq. II.16 and in the context of $b \to c\bar{c}s$ transition decay, the time-dependent *CP* asymmetry is expressed as:

$$\mathcal{A} = S\sin(\Delta m_d \Delta t) - C\cos(\Delta m_d \Delta t). \tag{II.32}$$

In this case, the ratio $\frac{q}{p}$ is

$$\frac{q}{p} = \frac{V_{td}V_{tb}^*}{V_{td}^*V_{tb}}. \tag{II.33}$$

We then have

$$\lambda = \eta_f \frac{V_{td}V_{tb}^*}{V_{td}^*V_{tb}} \frac{V_{cd}^*V_{cb}}{V_{cd}V_{cb}^*}, \tag{II.34}$$

which results in C = 0 and, $S = -\eta_f \sin(2\beta)$, where η is the *CP* eigenvalue of the final state. In the golden modes, $\sin(2\beta)$ is then proportional to the *CP* violation in the interference between the decay and the oscillation.

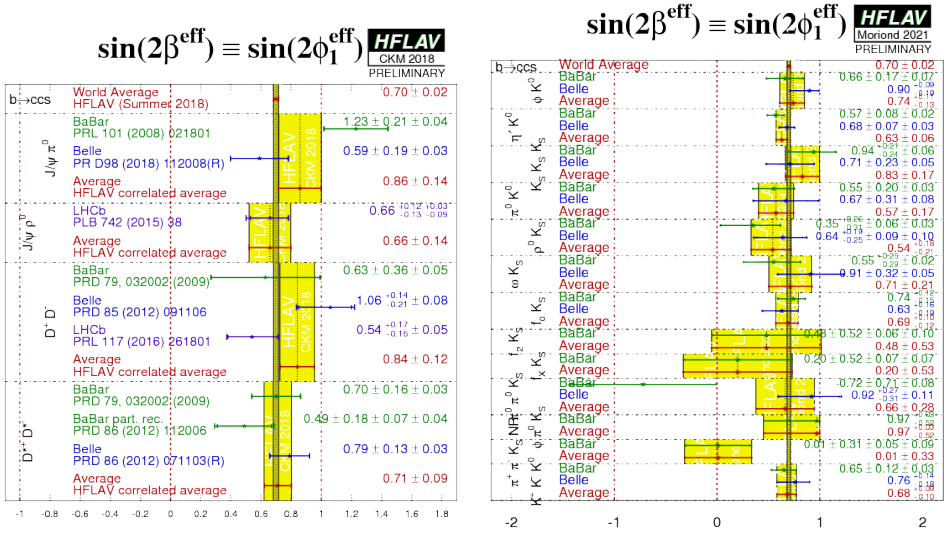

Figure II.2: Averaged values for $\sin(2\beta)$ (left) and $\sin(2\beta_{\text{eff}})$ (right) produced by the HFLAV collaboration. We see the two variables are now compatible with each other within experimental uncertainties [6], it was not the case years ago.

The CKM angle β can also be extracted from decays dominated by $b \to q\bar{q}s$ penguin transitions, e.g. charmless 3-body decays of B mesons. In the standard model, the *CP* violation in the interference between the decay and the mixing is expected to have the same magnitude in $b \to q\bar{q}s$ and $b \to c\bar{c}s$ transitions. When extracting β from process dominated by loops, the effective phase measured in these studies may deviate from the tree-level phase due to new physics particles intervening in the loops. To express this, the quantity extracted from loop-dominated process is called β_{eff}.

All recent measurements of $\sin(2\beta_{\text{eff}})$ are compatible with $\sin(2\beta)$ results within uncertainties [6]. Figure II.2 shows the most recent HFLAV averages together with the measurements on $\sin(2\beta)$ and $\sin(2\beta_{\text{eff}})$ that contributed to these averages.

This is an example of how studies of decay amplitude of 3-body decays can help to challenge again the Standard Model predictions, through CKM parameter or *CP*-violation measurements. I discuss in the next section amplitude analyses in the Dalitz plane.

II.3 Amplitude analyses and Dalitz planes

The study of the decay amplitudes of hadrons has always been one of the probes for testing our knowledge of particle physics and for looking for new processes. For example, the study of β decays of cobalt-60 showed that the parity, P, is maximally violated [29,30], and neutral-kaon decay measurements brought the first evidence of CP-violation effects [31].

In 2-body decays to pseudo-scalars, the energy in the final state is well determined. Indeed, rules of momentum and energy conservation are enough to fix all the degrees of freedom of the final state, up to an arbitrary rotation. By contrast, in decays to 3-body final states like $K^0_S h^+ h'^-$, momentum and energy preservation requirements are not enough to fully constrain the energy of the final state products.

We consider the decay of a scalar particle to 3 (pseudo)scalar particles. The system has 3 arbitrary rotation angles that can be fixed. Once momentum and energy conservation have been accounted for, we are left with 2 degrees of freedom. Hence, the decay amplitude of charmless 3-body B-meson decays needs to be described by two variables, and the corresponding plane is called the Dalitz plane. Structures can appear in the 2-dimensional decay amplitude and the interpretation is simplest if we represent it with two variables such that the decay amplitude's phase-space term is constant. In this well chosen 2-dimensional space we are able to study the dynamical structures of the decay amplitude. Such structures result from resonances and their interference. The variables that give a flat phase-space are the squared invariant masses of pairs of particles from the decay final state. This representation, firstly introduced by Dalitz [32], was further extended to the relativistic case by Fabri [33]. For 3-body decays of scalar particles, the differential decay probability reads:

$$d\Gamma = \frac{1}{(2\pi)^3 32 M^3} |A|^2 dm^2_{12} dm^2_{23}. \tag{II.35}$$

M is here the mass of the decaying particle, and m_{12} and m_{23} are respectively the invariant mass of the pair of particles 1, 2 and 2, 3.

Several empirically-motivated descriptions of 3-body decay amplitudes over the Dalitz plane exist, I detail in the next subsection one of these, the isobar formalism.

II.3.1 The isobar formalism

The most common description of 3-body decay amplitudes, the isobar formalism, relies on a coherent sum of contributions, often expressed as the sum of 2-body

resonances with a non-resonant contribution over the Dalitz plane of the form:

$$A(m_{12}^2, m_{23}^2) = \sum_r a_r e^{i\phi_r} A_r(m_{12}^2, m_{23}^2) + a_{NR} e^{i\phi_{NR}} A_{NR}(m_{12}^2, m_{23}^2). \quad \text{(II.36)}$$

In the equation above, the a_X coefficients are the magnitudes and ϕ_X are the phases of the resonant (r) or the non-resonant (NR) contributions. We consider in this section a meson decaying to three particles, denoted 1, 2, and 3. We assume that the resonance is produced in the channel of the pair of particles 1,2. The isobar formalism was developed to describe interactions between nuclei or interactions of nuclei with pions [34]. Later on it has been generalised to describe all 3-body decay amplitudes [35]. The amplitude of each resonance is represented as the product of form factors F_p and F_r with a resonance propagator, $T_r \times W_r$:

$$A_r = F_p \times F_r \times T_r \times W_r. \quad \text{(II.37)}$$

In this formalism, W_r is the angular dependence of the resonance. As for T_r, it is the dynamical function of the resonance. Then, F_p and F_r are the form factors of the parent particle and the resonance respectively.

Angular dependence W_r

The angular dependence of the resonance decay is described by Zemach tensors [36]. With J being the spin of the intermediate state:

$$W_r = 1 \text{ for } J = 0, \quad \text{(II.38)}$$

$$W_r = -2(p \times q) \text{ for } J = 1, \quad \text{(II.39)}$$

$$W_r = \frac{4}{3}[3(p \times q)^2 - (|p||q|)^2] \text{ for } J = 2. \quad \text{(II.40)}$$

In these equations, q is the momentum of one of the daughters of the resonance and p is the momentum of the bachelor particle.

Dynamical function T_r

The relativistic Breit-Wigner [37] is a suitable lineshape when we are dealing with narrow (but finite-width) resonances:

$$\text{Tr} = \frac{1}{m_r^2 - m_{12}^2 - i m_r \Gamma_{12}}, \quad \text{(II.41)}$$

where m_r is the mass of the resonance and Γ_{12} is the mass-dependent width defined as:

$$\Gamma_{12} = \Gamma_r(\frac{q_{12}}{q_r})^{2J+1}(\frac{m_r}{m_{12}})F_r^2, \tag{II.42}$$

where Γ_r and J are the width and spin of the resonance. q_{12} is defined as the momentum of the daughter particles in the rest frame of particles 1 and 2. In this equation, q_r is the momentum that the final state particles would have in the rest frame of a resonance of mass m_r.

Alternative distributions can be used. For example, ρ contributions are usually described thanks to a Gounaris-Sakurai distribution [38]. The Flatté distribution has been created to describe f_0 resonances [39].

Form factors F_p and F_r

These form factors are described by Blatt-Weisskopf barrier radius parameters [40]. They are expressed as following, depending on J, the spin of the resonance:

$$\text{When } J = 0,\ F = 1, \tag{II.43}$$

$$\text{When } J = 1,\ F = \sqrt{\left(\frac{1 + R^2 q_r^2}{1 + R^2 q_{12}^2}\right)}, \tag{II.44}$$

$$\text{When } J = 2,\ F = \sqrt{\left(\frac{9 + 3R^2 q_r^2 + R^4 q_r^4}{9 + 3R^2 q_{12}^2 + R^4 q_{12}^4}\right)}, \tag{II.45}$$

where R is the radial parameter of the decaying meson. Typical values of this parameters are at the order of 1 to 5 GeV^{-1}. The form factor F is normalised so that it is equal to 1 when $q_r = q_{12}$

II.3.2 Isobar-formalism limitations and alternatives

Although the isobar formalism is conceptually simple and has been successful in many past studies, it has limitations. First of all, it is not satisfactory on a theoretical level. Indeed, using several Breit-Wigner distributions in the propagator leads to non-conserved probability currents. On the experimental level, the isobar formalism is a model-dependent approach. When describing an amplitude with a model, an uncertainty related to this approach should be included, which may not be trivial to do.

The strong dynamics of the resonances is not easily determined from experimental or theoretical inputs. A poor knowledge of the strong-interaction

parameters of the resonances would lead to an imprecise modelling of the decay amplitude.

We also note that in the case of S-waves, the Breit-Wigner-like model of the decay amplitude contributions often used in the isobar formalism is not satisfactory. In fact, S-waves are composed of many broad and overlapping contributions whereas models similar to the Breit-Wigner lineshape are well suited for narrow resonances.

The limitations of the isobar model also impact the modelling of the non-resonant contributions, which can cover the whole Dalitz plane. When studying charm decays, this contribution is typically relatively small. However, due to the large phase space, the situation is quite the opposite in B-meson decays, especially into charmless final states, since charmless resonances generally have a small mass compared to that of the B meson. Experimentally, in most cases, the non-resonant contribution is often described as a single isobar component with a smooth lineshape (a flat or exponential distribution, for example). This choice is not motivated by any particular theoretical input; in most of the channels, the non-resonant contribution is poorly understood theoretically and could even consist of several contributions.

Alternatives have been developed to deal with the isobar model limitations. S-wave contributions can be described through the K-matrix formalism [17–19]. In this approach, the unitarity of the 2-body scattering matrix is preserved (which is not the case in the isobar formalism). The K-matrix formalism relies on the hypothesis that the contribution described in this formalism does not interact with other final states contributing to the decay amplitude. The amplitude is then given by:

$$\mathcal{A}_{u(s)} = \sum_u [I - iK(s)\rho(s)]^{-1}_{uv} P_v(s). \tag{II.46}$$

In this expression, $s = m^2_{12}$ is the squared invariant mass of the particle pair 1 and 2, I is the identity matrix, K is the matrix describing the scattering process, ρ is the diagonal phase-space matrix, and P is the production vector. The indices u and v represent the the production and scattering channels, they take values between 1 and 5, where $1 = \pi\pi$, $2 = K\bar{K}$, $3 = \pi\pi\pi\pi$, $4 = \eta\eta$, and $5 = \eta\eta'$.

A recent LHCb study compared several approaches to describe the S-wave component of $B^+ \to \pi^+\pi^+\pi^-$ [11, 12], by including an S-wave component described by three different approaches: the isobar model, the K-matrix formalism [17–19] and a quasi-model-independent (QMI) procedure [20–24]. The quasi-model-independent procedure is based on a binning of the phase space.

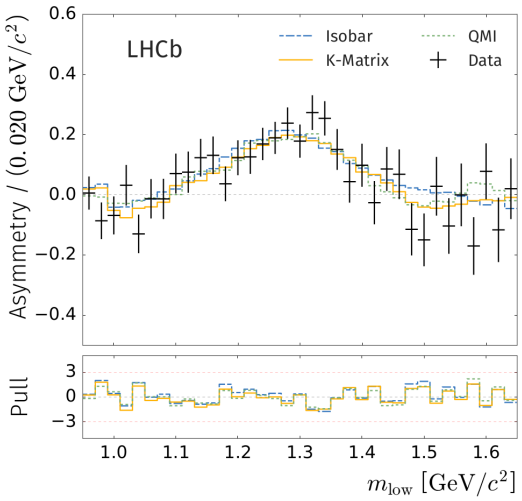

Figure II.3: Figure from an LHCb analysis of $B^+ \to \pi^+\pi^+\pi^-$ [11, 12], showing measured *CP* as a function of the smaller of the two $\pi^+\pi^-$ invariant mass in data (points), along with three models. The amplitude analysis of the $B^+ \to \pi^+\pi^+\pi^-$ described a S-wave component with three different approaches: the isobar model, the K-matrix formalism and a quasi-model-independent approach. Fits performed with all three approaches lead to a good agreement with the data and with each other [11, 12].

The fits to the decay amplitude obtained with all three approaches are in good agreement with the data and with each other as shown in Fig. II.3.

Establishing a correct description of the decay amplitude is the occasion to look for new resonance states or measure the parameters, and to determine the relative magnitudes and phases of their amplitudes. I can illustrate this with a recent example from LHCb: an amplitude analysis of the $B_s^0 \to K_S^0 K^+\pi^-$ decays [9].

A practical case: the amplitude analysis of the $B_s^0 \to K_S^0 K^+\pi^-$ decays

The amplitude analysis of the $B_s^0 \to K_S^0 K^+\pi^-$ decays, performed by LHCb [9] was the first amplitude analysis of these decays. It is untagged and time-integrated. This analysis was performed on the data sample collected by LHCb during 2011 and 2012. The distribution of the signal events over the Dalitz plane is obtained thanks to the sWeights that are extracted from the run 1 $K_S^0 h^+ h'^-$ study. Figure II.4 shows the Dalitz-plot distribution of the $B_s^0 \to K_S^0 K^+\pi^-$ decays once the background contributions have been subtracted and the efficiency corrected. To summarise briefly the procedure,

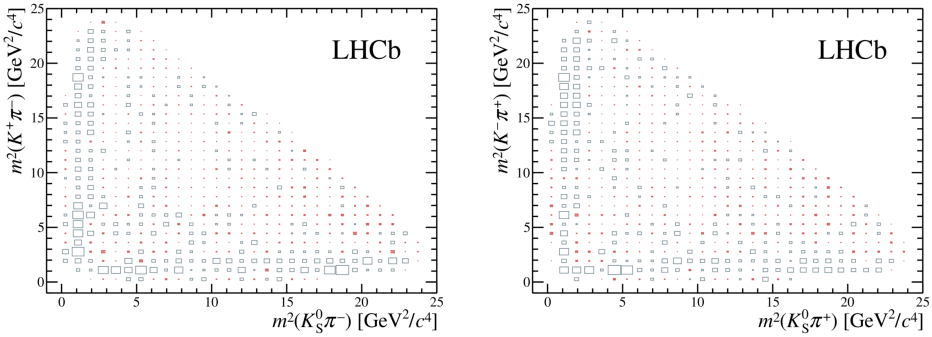

Figure II.4: Figure from an LHCb analysis of $B^0_s \to K^0_S K^+\pi^-$ showing the dalitz-plot distribution of the $B^0_s \to K^0_S K^+\pi^-$ signal events at the left and $B^0_s \to K^0_S K^-\pi^+$ at the right. The background contributions have been subtracted and the efficiency has been corrected thanks to the studies performed during the Run 1 $K^0_S h^+ h'^-$ analysis [9].

the description of the resonance content of the Dalitz plane is constructed by adding or removing contributions and by studying their effect on the fit to the Dalitz plane with the aim of finding a model that gives a good description of the data with the fewest resonant contributions. The baseline model of the $B^0_s \to K^0_S K^+\pi^-$ decays consist of the $K^*(892)^{0,+}$,$K^*_0(1430)^{0,+}$ and $K^*_2(1430)^{0,+}$ resonances. With these measurements the branching fractions of $B^0_s \to K^*(892)^{\pm}K^{\mp}$ and $B^0_s \to K^*(892)^0 K^0$ has been updated whereas the branching fractions of $B^0_s \to K^*_2(1430)^{\pm}K^{\mp}$ and $B^0_s \to K^*_2(1430)^0 K^0$ have been measured for the first time. The fit fractions of the study are converted into branching fractions by multiplying them with the known branching fraction of $B^0_s \to K^0_S K^+\pi^-$. Their values measured by LHCb [9] are:

$$\begin{aligned}
B(B^0_s \to K^*(892)^{\pm}K^{\mp}) &= (12.4 \pm 0.8 \pm 0.5 \pm 2.7 \pm 1.3) \times 10^{-6},\\
B(B^0_s \to K^*(892)^0 K^0) &= (13.2 \pm 1.9 \pm 0.8 \pm 2.9 \pm 1.4) \times 10^{-6},\\
B(B^0_s \to K^*_2(1430)^{\pm}K^{\mp}) &= (3.4 \pm 0.8 \pm 0.4 \pm 5.4 \pm 0.4) \times 10^{-6},\\
B(B^0_s \to K^*_2(1430)^0 K^0) &= (5.6 \pm 1.5 \pm 0.6 \pm 7.0 \pm 0.6) \times 10^{-6},
\end{aligned}$$

where the uncertainties are respectively statistical, systematic related to experimental and model uncertainties, and due to the uncertainty on $B(B^0_s \to K^0 K^{\pm}\pi^{\mp})$.

II.4 Measuring γ from charmless 3-body decays

I discuss in this chapter how the CKM phase γ can be extracted from charmless 3-body decays. I first give a brief overview of the methods that are commonly used when measuring this angle from tree-level process to final states containing a charmed hadron. I detail then how γ can be extracted from 3-body charmless decays of B mesons following a method developed by Bhattacharya, Imbeault and London [15]. The experimental aspect is further detailed in Chap. III.

Measuring γ from tree-level and loop-level process

The CKM angle γ is one of the least constrained angle from the CKM unitarity triangle. It is defined as

$$\gamma \equiv arg[-\frac{V_{ud}V_{ub}^*}{V_{cd}V_{cb}^*}]. \tag{II.47}$$

The most recent world average [6] gives:

$$\gamma = (66.2^{+3.4}_{-3.6})^\circ. \tag{II.48}$$

It is produced by combining results from BaBar and LHCb.

Couplings to the top quark are not involved in the definition of γ. Thus, γ can be extracted thanks to decays happening at the tree level. The first method I discuss uses the interference between the $b \to c$ and $b \to u$ transitions.

The GLW method [13] offers an opportunity to extract cleanly the CKM angle γ. In this method, the weak phase γ is extracted from B-meson decays to a neutral *CP*-eigenstate D-meson and a charged kaon, namely $B^\pm \to D^0_{1,2}K^\pm$. The *CP*-even and -odd eigenstates are expressed in terms of the flavour eigenstates as $D^0_{1,2} = \frac{D^0 \pm \bar{D}^0}{\sqrt{2}}$. We disentangle these CP eigenstates thanks to their decay products. We note that

$$\sqrt{2}A(B^+ \to D^0_1 K^+) = A(B^+ \to \bar{D}^0 K^+) + A(B^+ \to D^0 K^+) \tag{II.49}$$

$$\sqrt{2}A(B^- \to D^0_1 K^-) = A(B^- \to \bar{D}^0 K^-) + A(B^- \to D^0 K^-). \tag{II.50}$$

The amplitude of the $B^\pm \to D^0_1 K^\pm$ decay can be written as

$$\sqrt{2}A(B^+ \to D^0_1 K^+) = |A|\, e^{i\gamma} e^{i\delta} + \left|\bar{A}\right| e^{i\bar{\delta}} \tag{II.51}$$

$$\sqrt{2}A(B^- \to D^0_1 K^-) = |A|\, e^{-i\gamma} e^{i\delta} + \left|\bar{A}\right| e^{i\bar{\delta}}. \tag{II.52}$$

If we take into account that the *CP* symmetry is conserved in $B^{\pm} \to D^0(\bar{D^0})K^{\pm}$, we have

$$\begin{aligned} \left|A(B^+ \to D_1^0 K^+)\right|^2 - \left|A(B^- \to D_1^0 K^-)\right|^2 = \\ 2\left|A(B^+ \to \bar{D^0} K^+)\right| \left|A(B^+ \to D^0 K^+)\right| sin(\bar{\delta} - \delta) sin(\gamma) \end{aligned} \tag{II.53}$$

where δ and $\bar{\delta}$ are the strong phases of the final states. Measuring the decay amplitudes involved in this relation allows one to extract γ. There is an ambiguity on the sign of γ from this relation. From *CP*-violation in K decays, we know that $\sin\gamma$ is positive. There is also a second unknown, namely the strong phase difference ($\bar{\delta}$ - δ). The latter is removed by combining several measurements of decays of the form $B^{\pm} \to D_{1,2}^0 X^{\pm}$ where X is for example K, $K^0\pi$,...

Experimentally, 4 ratios are accessible from which we can extract γ. They consist of 2 ratios of amplitudes of the *CP*-even and *CP*-odd state with the favoured decay of the D-meson, such as $D \to K\pi$:

$$R_{1,2} = 2\frac{\Gamma(B^- \to D_{1,2}^0 K^-) + \Gamma(B^+ \to D_{1,2}^0 K^+)}{\Gamma(B^- \to D_{\text{fav}}^0 K^-) + \Gamma(B^+ \to D_{\text{fav}}^0 K^+)}. \tag{II.54}$$

On the other hand, the *CP*-asymmetry in the case where the charged B-mesons are decaying to a *CP*-even or a *CP*-odd eigenstates are described as

$$A_{1,2} = \frac{\Gamma(B^- \to D_{1,2}^0 K^-) - \Gamma(B^+ \to D_{1,2}^0 K^+)}{\Gamma(B^- \to D_{1,2}^0 K^-) + \Gamma(B^+ \to D_{1,2}^0 K^+)}. \tag{II.55}$$

Using Eq. II.49, we can write $R_{1,2}$ and $A_{1,2}$ as

$$R_{1,2} = 1 + r_B^2 \pm 2r_B \cos(\delta_B)\cos(\gamma) \tag{II.56}$$

$$A_{1,2} = \frac{\pm 2r_B \sin\delta_B \sin\gamma}{1 + r_B^2 \pm 2r_B \cos(\delta_B)\cos(\gamma)}, \tag{II.57}$$

where r_B is the ratio of decay amplitudes and δ_B is the relative strong phase between $B^+ \to D^0 K^+$ and $B^+ \to \bar{D^0} K^+$.

This method has two major limitations: γ is measured within some ambiguities and the precision that can be achieved on the γ extraction is limited by the sizeable differences in the amplitude of the $B^{\pm} \to \bar{D^0} X^{\pm}$ and the $B^{\pm} \to D^0 X^{\pm}$ process. Indeed, the precision on the measurement is a function of the ratio of amplitudes of these process, such as:

$$r_B = \left|\frac{A(B^- \to \bar{D^0} K^-)}{A(B^- \to D^0 K^-)}\right| \sim 0.1 \tag{II.58}$$

An alternative method was suggested in order to achieve a better level of precision on the measurement of γ. The ADS method [14] generalised the GLW method to D-mesons not only decaying to *CP* eigenstates but also to flavour-specific final states. With this new inclusion, favoured $\bar{D}^0$ decays to a final state and doubly Cabbibo suppressed D^0 decays to the same final state both participate to the measurement. In that situation, the amplitudes are at around the same level and we can achieve a better precision on the extraction of γ. The *CP*-violation effects are also larger in this scenario.

In that situation and contrary to what was obtained in the case of the GLW method, the measurement of the decay rate and the *CP* asymmetry require that the hadronic parameters of the D meson are known. The observables that are derived are

$$R_{ADS} = r_B^2 + r_D^2 + 2r_B r_D \cos(\delta_B + \delta_D)\cos\gamma \tag{II.59}$$

$$A_{ADS} = 2\frac{r_B r_D \sin(\delta_B + \delta_D)\sin\gamma}{r_B^2 + r_D^2 + 2r_B r_D \cos(\delta_B + \delta_D)\cos\gamma} \tag{II.60}$$

where r_D and δ_D are respectively the ratio of magnitudes and a strong phase such that

$$\frac{\mathcal{A}(D^0 \to f)}{\mathcal{A}(\bar{D}^0 \to f)} = r_D e^{i\delta_D}. \tag{II.61}$$

The GGSZ method [41] relies on 3-body D-meson decays. Such decays present quite large decay rates. In this method, r_B, δ_B and γ are extracted from a fit to the D-meson Dalitz-plane distribution thanks to the the interference between the D and the $\bar{D}$ such as

$$A_{B^+}(m^2_{K^0_S\pi^+}, m^2_{K^0_S\pi^-}) = \bar{A}_D + r_B e^{i(\delta_B+\gamma)} A_D. \tag{II.62}$$

and

$$A_{B^-}(m^2_{K^0_S\pi^+}, m^2_{K^0_S\pi^-}) = A_D + r_B e^{i(\delta_B-\gamma)} \bar{A}_D. \tag{II.63}$$

I have reviewed the most common methods employed to extract γ from 2- and 3-body decays to final state containing a charmed hadron. I cover now the theoretical framework of the extraction of γ from 3-body charmless B-meson decays, which I will use in Chap. III.

Extracting γ from 3-body charmless B-meson decays

A method was proposed by Bhattacharya, Imbeault and London [15] to extract the CKM phase γ from 3-body charmless B-meson decays. In this approach,

the decay amplitudes contributing to 3-body B-meson decays of the type $B \to K\pi\pi, B \to KK\bar{K}, B \to K\bar{K}\pi, B \to \pi\pi\pi$ are expressed as topologically distinct diagrams. This is analogous to the 2-body scenario. Gronau et al. [42] showed that 2-body decays amplitudes can be expressed with the help of only 9 diagrams. We should note that among these diagrams, the annihilation diagrams - there exist 3 of them - are expected to have a small contribution compared to other types of diagrams, so they are then neglected in the following discussion.

The 6 remaining types of diagrams (for 2-body decays) are the following: the tree amplitudes T and C (colour-favoured and colour-suppressed respectively), the gluonic penguin amplitudes P_{tc} and P_{uc}, and the colour-favoured and colour-suppressed electroweak-penguin amplitudes P_{EW} and P_{EW}^{C}.

Extending this process to 3-body decays, extra transitions are available, and thus extra types of diagrams need to be introduced. To distinguish diagrams with a $b \to s$ transition from $b \to d$, the former are denoted with a prime. Diagrams contributing to 3-body decay require a pair of quark to be popped from the vacuum. In most cases it is assumed that this pair is either $u\bar{u}$ or $d\bar{d}$. In the cases where the popped pair is $s\bar{s}$, the diagrams are distinguished by an s subscript. Then, when the pair of quarks is popped between 2 final-state quarks, excluding the spectator quark, the diagram possesses a subscript "1" ; the subscript "2" denotes a diagram for which the pair of quarks has been popped between the spectator quark and another quark.

The next distinction between 2-body and 3-body scenarios is the momentum dependence of the diagrams. When a B-meson decays to 2 particles, their momenta are equal in magnitude in the rest frame and thus the diagrams are not momentum-dependent. This does not hold for 3-body B-meson decays. In such case, the diagram amplitudes depend on the momentum of the particles involved in the process.

Lastly, one should note that in the case where $B \to P_1P_2P_3$ is a process going to a flavour-specific final state, and in the situation where P_2 and P_3 are identical under isospin, for example, the decay amplitude should be symmetric. Indeed, the P_2P_3 pair has either a CP-even or CP-odd symmetry, hence the decay amplitude has to be respectively symmetric or antisymmetric when permuting P_2 and P_3. With that in mind, the symmetric amplitude reads:

$$\mathcal{A}_{sym} = \frac{1}{\sqrt{2}}(A(m^2_{P_1P_2}, m^2_{P_1P_3}) + A(m^2_{P_1P_3}, m^2_{P_1P_2})) \tag{II.64}$$

The antisymmetric amplitude is given by:

$$\mathcal{A}_{antisym} = \frac{1}{\sqrt{2}}(A(m^2_{P_1P_2}, m^2_{P_1P_3}) - A(m^2_{P_1P_3}, m^2_{P_1P_2})) \tag{II.65}$$

To extract γ from 3-body charmless B-meson decays, we can use the decay of the form $B \to K\pi\pi, B \to KK\bar{K}, B \to K\bar{K}\pi, B \to \pi\pi\pi$. The (symmetric or antisymmetric) decay amplitudes of these process will be expressed in terms of the diagram amplitudes, their relative strong phases and a weak phase γ, treating separately situations where the final state is a *CP*-even or a *CP*-odd eigenstate. I give as an example the antisymmetric decay amplitude of the $B^+ \to K^+\pi^+\pi^-$ expressed as

$$\begin{aligned} A(B^+ \to K^+\pi^+\pi^-)_{|A\rangle} = &-T'_2 e^{i\gamma} - C'_1 e^{i\gamma} + \tilde{P}'_{ut} e^{i\gamma} + \tilde{P}'_{ct} \\ &- P'_{EW1} - \frac{1}{3} P'^C_{EW1} - \frac{2}{3} P'^C_{EW2}. \end{aligned} \tag{II.66}$$

A set of experimental observables is also available. It consists of the branching fractions, the direct *CP* asymmetries and the indirect *CP* asymmetries (where available) of the decay modes mentioned earlier. If we have more observables than theoretical variables, we can extract γ from a fit. This requirement is fulfilled under the assumption of flavour SU(3) symmetry [43]. With this assumption, the particles in the final states are identical under flavour. The corresponding amplitude should then be symmetrised. Because we have 3 particles in the final states, there are 6 possible symmetrisations of the Dalitz plane: the fully symmetric state, the fully antisymmetric state and the mixed states. Moreover, under the SU(3) assumptions, relations exist between the electroweak penguin and the tree diagrams:

$$\begin{aligned} P_{EWi} &= \kappa T_i, \\ P^C_{EWi} &= \kappa C_i, \end{aligned}$$

where κ is expressed as follows if the Wilson coefficients [44] follow $C_1/C_2 = C_9/C_{10}$:

$$\kappa \equiv -\frac{3}{2} \frac{\left|\lambda_t^{(s)}\right|}{\left|\lambda_u^{(s)}\right|} \frac{C_9 + C_{10}}{C_1 + C_2}.$$

With this set of assumptions and relations, the number of theoretical parameters is reduced and γ can be extracted from a fit.

The method described in this subsection has the quality of being sensitive to new physics. Indeed, charmless 3-body B-meson decays receive large contribution from loop process to which new particles or interactions could contribute. Indirect searches for new physics can thus be performed with this method since in the presence of new physics γ values extracted with this method could be shifted from the Standard Model expectations.

The next section gives more details on the experimental application of the method, the choice of the decays to be studied and the feasibility of the γ extraction in the context of the fully-antisymmetric state.

Chapter III

Extraction of the CKM phase γ using charmless 3-body decays of B mesons

The extraction of the CKM phases α, β and γ enables a robust test of the Standard Model. Studying these quantities with various methods provides a better understanding of the Standard Model and by testing for inconsistencies in Standard Model predictions such as $\alpha+\beta+\gamma=\pi$ brings many opportunities to observe New Physics. I will discuss here the extraction of the CKM phase γ. The most recent world average [6] is:

$$\gamma = (66.2^{+3.4}_{-3.6})^{\circ}.$$

This CKM phase, which is a key parameter when constraining the unitarity triangle, still has relatively large uncertainties. The most common method of extracting this CKM parameter is based on 2-body decays, where tree processes are dominant, such as $B \to Dh$ decays, where h is a pion or a kaon and B is either a B_d or a B_u meson. The related relative theoretical uncertainties are very small, of the order of 10^{-7}.

The CKM phase γ can also be extracted from charmless 3-body decays of B mesons. In these processes, loop diagrams contribute to the decay amplitudes, which results in increased sensitivity to new physics by comparison with $B \to Dh$ decays. In this chapter we will focus on charmless $B \to PPP$ decays, where the pseudoscalar P is either a pion or a kaon. The method uses the assumption of SU(3) symmetry, under which these two particles, K and π, are the same. One can then obtain different symmetry states from combinations of the amplitudes, for example fully symmetric and fully antisymmetric states.

We will describe the method employed to measure γ from $B \to PPP$ decays in section III.1. In Ref. [16], it was shown that extracting γ with the fully

symmetric state provided encouraging results. Six values were found, one being compatible with the Standard Model $\gamma = 68.9^{+8.6}_{-8.6} \pm 2.4^\circ$. In section III.2 I present my study of γ extraction using the antisymmetric state and discuss why this is not feasible with the experimental inputs presently available.

III.1 Introduction to the method used to extract the CKM phase γ with charmless 3-body decays of B mesons

The extraction of the CKM phase γ we present here relies on charmless 3-body decays of B mesons, more precisely $B \to PPP$ decays, where P is a pseudoscalar meson and B is either a B_d or a B_u meson. For each of these decays, the amplitude will be expressed in terms of the diagrams that contribute to it. To be able to extract γ from a fit (see section III.2), there must be at least as many experimental observables as theoretical parameters.

To help meeting this requirement, the number of theoretical parameters may be reduced by imposing flavour $SU(3)$ symmetry. Under this approximation, the final-state particles are identical and therefore we need to symmetrise the corresponding Dalitz plane. A transformation can be applied to each Dalitz-plane amplitude to convert it into amplitudes with different symmetry properties. This transformation relies on the permutations of the final state particles; six of them exist. With these permutations, six states can be built: fully symmetric $|S\rangle$, fully antisymmetric $|A\rangle$ and four mixed states $|M_i\rangle$:

$$|S\rangle = \frac{1}{6}(|123\rangle + |312\rangle + |231\rangle + |321\rangle + |132\rangle + |213\rangle), \tag{III.1}$$

$$|A\rangle = \frac{1}{6}(|123\rangle + |312\rangle + |231\rangle - |321\rangle - |132\rangle - |213\rangle), \tag{III.2}$$

$$|M_1\rangle = \frac{1}{12}(2|123\rangle + 2|132\rangle - |312\rangle - |321\rangle + |231\rangle - |213\rangle), \tag{III.3}$$

$$|M_2\rangle = \frac{1}{4}(|312\rangle - |231\rangle - |321\rangle + |213\rangle), \tag{III.4}$$

$$|M_3\rangle = \frac{1}{4}(-|312\rangle - |321\rangle + |231\rangle + |213\rangle), \tag{III.5}$$

$$|M_4\rangle = \frac{1}{12}(2|123\rangle - 2|132\rangle - |312\rangle + |321\rangle - |231\rangle + |213\rangle). \tag{III.6}$$

Several decay modes contribute to each symmetry state. For each decay mode, the amplitude is expressed in term of γ and the diagrams that contribute to it. As detailed in Sec. II.4 and explained in Ref. [45], the amplitude

can be considered to consist of the following components: the gluonic-penguin amplitudes P_{ut} and P_{ct}, the colour-favoured and colour-suppressed tree contributions $T_{1,2}$ and $C_{1,2}$, and the colour-favoured and colour-suppressed electroweak penguin amplitudes $P_{EW1,2}$ and $P^C_{EW1,2}$. This allows us to write relations between experimentally measurable quantities and the theory parameters we will fit, including γ. We can build up to three observables from each measured amplitude:

$$\begin{aligned} X(m^2_{12}, m^2_{13}) &= \left|\mathcal{M}(m^2_{12}, m^2_{13})\right|^2 + \left|\overline{\mathcal{M}}(m^2_{12}, m^2_{13})\right|^2, \\ Y(m^2_{12}, m^2_{13}) &= \left|\mathcal{M}(m^2_{12}, m^2_{13})\right|^2 - \left|\overline{\mathcal{M}}(m^2_{12}, m^2_{13})\right|^2, \\ Z(m^2_{12}, m^2_{13}) &= Im\left[\left|\mathcal{M}^*(m^2_{12}, m^2_{13})\right| \left|\overline{\mathcal{M}}(m^2_{12}, m^2_{13})\right|\right]. \end{aligned} \tag{III.7}$$

The observable X is associated with the decay amplitude, Y with the direct CP-asymmetry and Z with the indirect CP-asymmetry.

Under flavour $SU(3)$ symmetry and assuming that the Wilson coefficients obey to

$$\frac{C_1}{C_2} = \frac{C_9}{C_{10}},$$

as described in Ref. [45], the penguin diagrams contributing to the theoretical expression of the $B \to PPP$ decay amplitude are proportional to the tree diagrams (see Sec.II). In the case of the antisymmetric state, we have

$$\begin{aligned} P_{EWi} &= \kappa T_i, \\ P^C_{EWi} &= \kappa C_i, \end{aligned}$$

which reduces again the amount of free parameters.

We will now study the antisymmetric state in detail.

III.2 Study of the Antisymmetric state

In order to extract γ, several $B \to PPP$ decays are considered. They consist of the modes $B \to \pi\pi\pi$, $B \to K\pi\pi$, $B \to KK\pi$ and $B \to KKK$. When two or more identical particles are present in the final state, the antisymmetric state has a null amplitude. Also, as both K^0 and $\overline{K}^0$ are reconstructed as $K^0_S \to \pi^+\pi^-$, they are considered as the same particle. With this in mind, we are left with five distinct decay modes when studying the antisymmetric state:

$$\begin{aligned} B^+ \to K^+\pi^+\pi^-, B^+ \to K^0\pi^+\pi^0, B^0 \to K^0\pi^+\pi^-, \\ B^0 \to K^+\pi^0\pi^-, B^0 \to K^0K^+K^-. \end{aligned}$$

Considering only the antisymmetric symmetry state $|A\rangle$, the amplitudes of these decays are expressed as:

$$\begin{aligned}
A(B^+ \to K^+\pi^+\pi^-)_{|A\rangle} &= -T'_2 e^{i\gamma} - C'_1 e^{i\gamma} + \tilde{P}'_{ut} e^{i\gamma} + \tilde{P}'_{ct} \\
&\quad - P'_{EW1} - \frac{1}{3} P'^C_{EW1} - \frac{2}{3} P'^C_{EW2}, \\
\sqrt{2} A(B^+ \to K^0\pi^+\pi^0)_{|A\rangle} &= -T'_1 e^{i\gamma} - C'_2 e^{i\gamma} - 2\tilde{P}'_{ut} e^{i\gamma} \\
&\quad - 2\tilde{P}'_{ct} - P'_{EW2} - \frac{1}{3} P'^C_{EW1} - \frac{2}{3} P'^C_{EW2}, \\
A(B^0 \to K^0\pi^+\pi^-)_{|A\rangle} &= -T'_1 e^{i\gamma} - C'_1 e^{i\gamma} - \tilde{P}'_{ut} e^{i\gamma} - \tilde{P}'_{ct} \\
&\quad - P'_{EW1} - \frac{2}{3} P'^C_{EW1} - \frac{1}{3} P'^C_{EW2}, \\
\sqrt{2} A(B^0 \to K^+\pi^0\pi^-)_{|A\rangle} &= T'_1 e^{i\gamma} - T'_2 e^{i\gamma} - C'_2 e^{i\gamma} + 2\tilde{P}'_{ut} e^{i\gamma} \\
&\quad + 2\tilde{P}'_{ct} - P'_{EW2} + \frac{1}{3} P'^C_{EW1} - \frac{4}{3} P'^C_{EW2}, \\
A(B^0 \to K^0 K^+ K^-)_{|A\rangle} &= T'_2 e^{i\gamma} - C'_1 e^{i\gamma} - \tilde{P}'_{ut} e^{i\gamma} - \tilde{P}'_{ct} \\
&\quad + \frac{1}{3} P'^C_{EW1} + \frac{2}{3} P'^C_{EW2}.
\end{aligned} \tag{III.8}$$

Thanks to these equations we can express the observables listed in Eq. III.7 in terms of the diagrams and the theory parameters that we want to fit. The observables X and Y, which are associated with the decay rate and the direct CP asymmetry, are relevant for all five decay modes; Z, which is related to the indirect CP asymmetry, is only meaningful for modes where a neutral B meson decays into a final state that is its own CP conjugate. In the present case this includes $B^0 \to K^0\pi^+\pi^-$ and $B^0 \to K^0 K^+ K^-$. We have then 12 observables.

We now count the theory parameters. In Eq. III.8, we see that 6 classes of diagrams contribute to the amplitudes: $\tilde{P}'_{ut}$, $\tilde{P}'_{ct}$, $T'_{1,2}$ $C'_{1,2}$, $P'_{EW1,2}$ and $P'^C_{EW1,2}$. These are complex terms: we have 6 magnitudes and 5 relative imaginary phases. We also count γ.

The twelve available observables can then be expressed in terms of twelve theoretical quantities. Since the number of observables is equal to the number of free parameters, the CKM phase γ can be determined. Noting that $|P_{ut}| \approx \lambda^2 |P_{ct}|$, where $\lambda \approx 0.22$ is the Wolfenstein parameter, P_{ut} can be neglected, reducing the number of free parameters by two and improving, in principle, the stability of the fit. This also gives room for an extra flavour SU(3)-breaking parameter, $\left|\alpha_{SU(3)}\right|$. This parameter can be used to control the proportion of flavour SU(3)-breaking. The assumption that SU(3)-flavour holds was made in Ref. [45]. If this parameter is found to be around 1, this assumption is valid.

III.2 Study of the Antisymmetric state

As a first step towards the γ extraction, we should measure the observables at one or several points in the Dalitz plane of each decay. For most of the decay modes listed above, LHCb did not publish any amplitude analysis yet. The model of the Dalitz-plane amplitude that we use to measure the observables is therefore taken from BaBar results (Refs. [46–50]). The amplitudes are described with the isobar model, as detailed in Sec. II. This model describes the amplitude over the Dalitz plane as a sum of resonant and non-resonant intermediate modes. Each of these contributions is taken as the product of a *CP*-violating term, $c_i^{\pm}$, and a *CP*-conserving term, $F_j(m_{13}^2, m_{23}^2)$:

$$A^{\pm} = \sum_j^N c_j^{\pm} F_j(m_{13}^2, m_{23}^2). \tag{III.9}$$

Here, A^+ is the amplitude of the B-meson decay, A^- is the decay amplitude of the charged-conjugate particle. For a given component, the *CP*-violating term is constant over the Dalitz plane, unlike the *CP*-conserving term. From BaBar studies (Refs. [46–50]), we know which intermediate modes contribute, and what are the magnitudes and phases of the corresponding *CP*-violating terms. In order to compute the amplitude distributions of the all 5 decays contributing to the antisymmetric state, given the inputs from BaBar , we use the package Laura++ [51]. From these computed amplitudes, we can compute the observables X, Y and Z (defined in Eq. (III.7)). We know how to measure the observables and we know their expressions in terms of diagrams and γ. In principle, we should be able to extract γ from the information available.

But first, we should note that the phase γ does not depend on the decay dynamics. Hence, performing the fit at several points in the Dalitz plane is equivalent to performing multiple measurements of γ; combining information from several chosen points in the Dalitz plane should, in principle, reduce the statistical uncertainties. However, due to the limited available statistics, the Dalitz-plane amplitude is describe by isobar parameters that are measured with a finite precision. These parameters have then uncertainties. Moreover, when the same isobar component contributes at multiple points in the Dalitz plane, the amplitudes at those points will be correlated. We propagate the uncertainties on the isobar parameters to compute the uncertainties on the observables X, Y and Z. From these uncertainties, correlations are computed. The fit does not have an infinite precision, hence strong correlations between the measurements at various points over the Dalitz plane harm the fit stability.

In practice, before we perform a fit on several DP coordinates, we should make sure that the correlations between the observables at those points are small

enough that the fit will converge. In most cases, the BaBar publications provide the covariance matrices for the parameters of the various isobar components used in their amplitude analyses. When this is not the case, we neglect the isobar parameters' correlations. The covariance matrix for the observables can be obtained with (III.10), using the formalism described, for example, in the book *Statistics*, by Barlow [52]

$$V_{\text{obs}}(s_{12}, s_{13}) = G(s_{12}, s_{13}) V_{\text{isobar}} \tilde{G}(s_{12}, s_{13}), \tag{III.10}$$

where $V_{\text{obs}}(s_{12}, s_{13})$ is the covariance matrix for the observables X, Y and Z, G is the covariance matrix of the observables and V_{isobar} is the covariance matrix for the isobar parameters, as given in BaBar publications. In the simplistic scenario where we extract γ on one single point over the Dalitz plane with only one resonance that is described by the two parameters a_0 and a_1, the covariance matrix G is

$$G(s_{12}, s_{13}) = \begin{pmatrix} \frac{\partial X(s_{12},s_{13})}{\partial a_0} & \frac{\partial X(s_{12},s_{13})}{\partial a_1} \\ \frac{\partial Y(s_{12},s_{13})}{\partial a_0} & \frac{\partial Y(s_{12},s_{13})}{\partial a_1} \\ \frac{\partial Z(s_{12},s_{13})}{\partial a_0} & \frac{\partial Z(s_{12},s_{13})}{\partial a_1} \end{pmatrix}. \tag{III.11}$$

This can be generalised to n points over a Dalitz plane containing several resonances described by m parameters:

$$\begin{aligned} V_{obs}((s_{12}, s_{13})_1, ..., (s_{12}, s_{13})_n) = \\ G((s_{12}, s_{13})_1, ..., (s_{12}, s_{13})_n) V_{isobar} \tilde{G}((s_{12}, s_{13})_1, ..., (s_{12}, s_{13})_n)), \end{aligned} \tag{III.12}$$

with

$$G((s_{12}, s_{13})_1, ..., (s_{12}, s_{13})_n) = \begin{pmatrix} \frac{\partial X(s_{12},s_{13})_1}{\partial a_0} & \cdots & \frac{\partial X(s_{12},s_{13})_1}{\partial a_m} \\ \vdots & \ddots & \vdots \\ \frac{\partial Z(s_{12},s_{13})_n}{\partial a_0} & \cdots & \frac{\partial Z(s_{12},s_{13})_n}{\partial a_m} \end{pmatrix}. \tag{III.13}$$

We can thus calculate the uncertainties on the observables X, Y, Z. We can also derive the correlations between observables measured at different points. This is sufficient information to compute the χ^2 or a set of theory parameters to be consistent with the experimental results at a set of points in the Dalitz plane. By minimising the χ^2, we can fit the theory parameters to the data.

Clearly, the choice of Dalitz plane points plays a key role. We aim to find sets of several points with reasonable correlations, so that the fit's covariance matrix among the theory parameters is positive definite.

To get the χ^2 profile as a function of γ, we perform a scan. We fix γ to consecutive values, spaced by 1°, in the interval [0°, 360°] and for each value of γ perform fits where the other theoretical quantities are free to vary. For each fixed value of γ, 100 fits are performed, with random initial values of the free parameters, and the fit with the smallest χ^2 is kept. This procedure greatly improves the probability to find the global minimum of χ^2 for each fixed value of γ. Fits that do not properly converge are rejected, as well as fits for which the correlation matrix is forced to be positive definite. The resulting χ^2 profile for the antisymmetric state is shown in Fig. III.1.

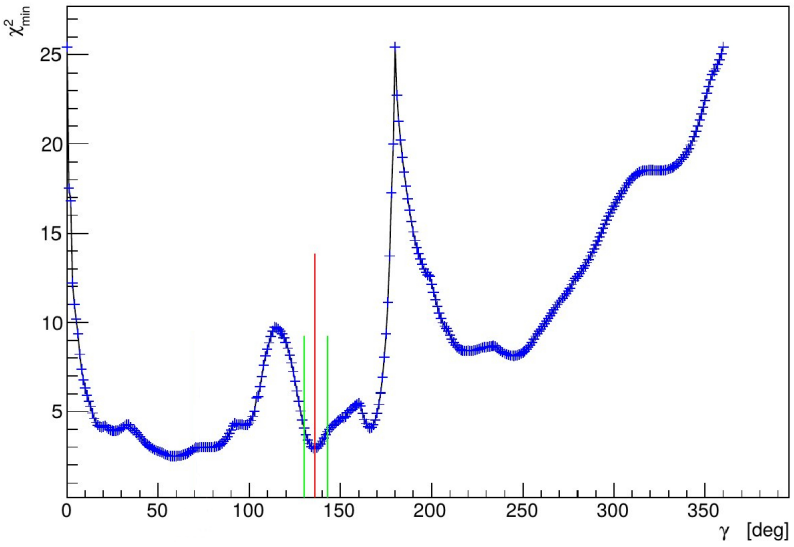

Figure III.1: χ^2 profile as a function of γ. With a 1° interval we fix γ to consecutive values in [0°, 360°]. For value, we perform 100 fits with the other theory parameters free, with their initial values randomised. The χ^2 profile is drawn by plotting the smallest χ^2 for each fixed γ value. The red line points to a possible value for γ. The green lines illustrate how we extract the statistical uncertainties from the χ^2 profile.

We then extract the minima obtained in the χ^2 profile. For each point in the χ^2 profile, we fit a cubic spline to extract the minima. When the fit converges, the minimum of the spline is considered as a solution of the γ extraction. When a minimum is deep enough, we can derive its statistical uncertainties. This is done by taking the χ^2 at the minimum and increasing its value by one unit of χ^2. Two points should correspond to this new value in the minimum well.

These correspond to the upper and lower uncertainties associated to the γ value at the considered minimum. If such values do exist, we are in the presence of a well defined minimum. This process is performed around 500 times, with the positions and uncertainties of the minima remeasured each time, to ensure the robustness of the results. Figure III.5 shows the histogram of the distribution of the minima extracted from 500 γ scans.

The process described above should be applied to each of the symmetry states described in Sec. III.1. It was applied successfully to the fully symmetric state in Ref. [16]. My work consisted of extending the method to apply to the antisymmetric state and, using a similar procedure, to obtain constraints on γ. The first step was to implement the BaBar amplitude model for $B^+ \to K^0_S\pi^+\pi^0$ decays, as other modes had been already implemented in the framework during the fully symmetric state study. With the Dalitz-plane model given in Ref. [50], I used the Laura++ package to encode and regenerate the Dalitz-plane distributions. Then, to ensure that we can compare the amplitude and that the observables we compute are meaningful, we have to normalise the amplitude. This is done using the normalisation factor N,

$$N = \sqrt{\frac{2}{\tau_B}\frac{\mathcal{B}}{\int\int |\mathcal{M}(s_{12},s_{13})|^2 + \left|\overline{\mathcal{M}}(s_{12},s_{13})\right|^2 ds_{12}ds_{13}}} \tag{III.14}$$

where $\mathcal{B}$ is the branching fraction of the mode that we want to normalise, τ_B is the lifetime of the neutral or charged B meson, as the integral runs over the Dalitz plane phase space.

The next step is to build the actual antisymmetric state. The Dalitz plane can be cut in six regions, corresponding to the six permutations of the daughter particles from Eq. III.1. For the fully symmetric and fully antisymmetric state, these 6 regions each contain the same information. Thus, we consider only one sixth of the plane.

In the case of the antisymmetric state, when we apply the antisymmetrisation of the Dalitz plane (Eq. III.2), contributions with an even spin are removed from the final amplitude. In the amplitude models, most of the broad non-resonant contributions are scalar ($J = 0$). We are then left mostly with narrow resonances, close to the boundary of the Dalitz plane (see Fig. III.2). For example, the isobar contribution content of $B^0 \to K_sK^+K^-$ is given in Tab. I [46]. Using the amplitudes of the antisymmetric state, I was able to compute the associated observables X, Y and Z(Eq. III.7). From Eq. III.8, I derived the expressions of each observable for each decay mode. They are detailed in App. A.1.

We now want to perform the extraction of γ using the fit procedure described

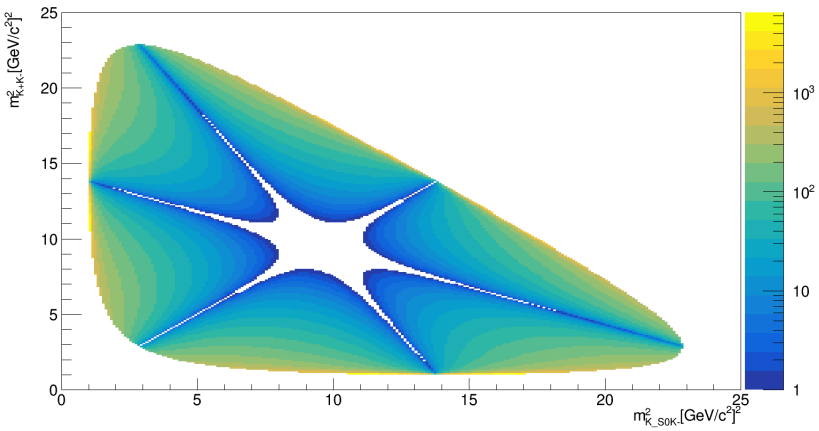

Figure III.2: The amplitude in the case of the fully antisymmetric state for one example mode, $B^0_d \to K^0_S K^+ K^-$

Contribution	Spin	mass [MeV/c^2]	width [MeV/c^2]
$\phi(1020)$	1	1019.455	4.26
$f_0(980)$	0	965	N/A
$f_0(1500)$	0	1505	109
$f'_2(1525)$	2	1525	73
$f_0(1710)$	0	1720	135
χ^0_c	0	3414.75	10.3
$S-wave$	0	N/A	N/A
$P-wave$	1	N/A	N/A

Table I: List of contribution for $B^0 \to K_s K^+ K^-$, from BaBar analysis [46]

before with as many points in the Dalitz plane as possible. As discussed below, it was not possible to find more than two points in the Dalitz plane with small enough correlations between their measured observables to ensure stable fits. As the correlation were on an average quite high, I decided to choose set of 2 points between which the correlation was lower than 90%. By comparison, the criterion in the fully-symmetric study was to choose set of 3 points with a correlation below 70%. A part of my work consisted in finding a method to identify and combine points with small enough correlation in the case of the antisymmetric state. For example, I tried to choose points in the Dalitz plane over a non-homogeneous grid. I implemented a grid that became finer as the amplitude gradient rose greater. This test is shown on Fig. III.3. No solution was found to use sets of more than two points. When using sets of

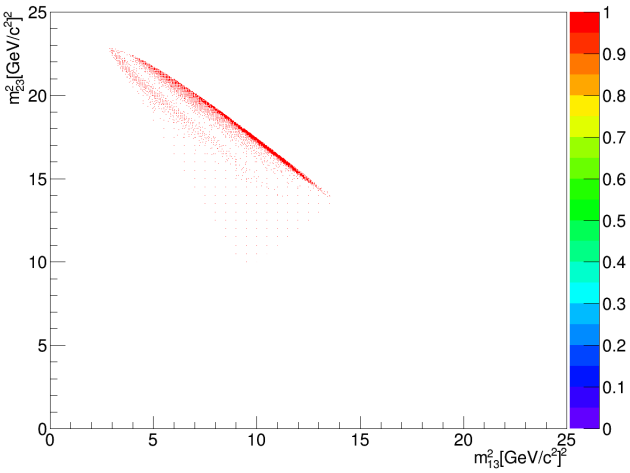

Figure III.3: Grid of points from which are picked the set of points at which γ is extracted. This grid is constructed so that the density of points grows greater with the amplitude gradient. I assumed that the meaningful information I would like to access is contained in regions were the amplitude was sizeable. As such, I built a grid that was finer where the variation in amplitude was important.

two points, it appeared that both of these points were most of the time chosen along the same resonances. This is illustrated in Fig. III.4. Each one of the red point is associated with one of the blue point. We see that each set of points with correlation below 90% were found in comparable region. In this configuration, we extract the same information over and over; we were not performing independent γ fits. This makes intuitive sens given that in most of the isobar models only 1 or 2 components with odd spin are present.

Given the limited information, most of the minima observed in the χ^2 profile are ill-defined, even with a single Dalitz-plane point. There is no robust minimum (Fig. III.5) obtained from the χ^2 profiles that can be extracted from the fit to the antisymmetric state as most of them had badly-behaved uncertainties. We can still try to interpret the results shown in Fig. III.1. Noting that a difference of 10 χ^2 units between 2 minima gives a P-value of around 1.6×10^{-3}, region with a χ^2 that are 10 χ^2 units away from the lowest χ^2 are excluded region. From Fig. III.1, the lowest χ^2 is of about 2 to 3 χ^2 units. We see first that the region above 180° seems disfavoured. With the criterion we discussed just now, the region above 280° is excluded. It is obvious that this discussion over just one single γ scan cannot be generalised. Nonetheless we can deduce from this reasoning that the study of the fully-antisymmetric state could contribute to the extraction of γ by excluding region of the γ scans. If we

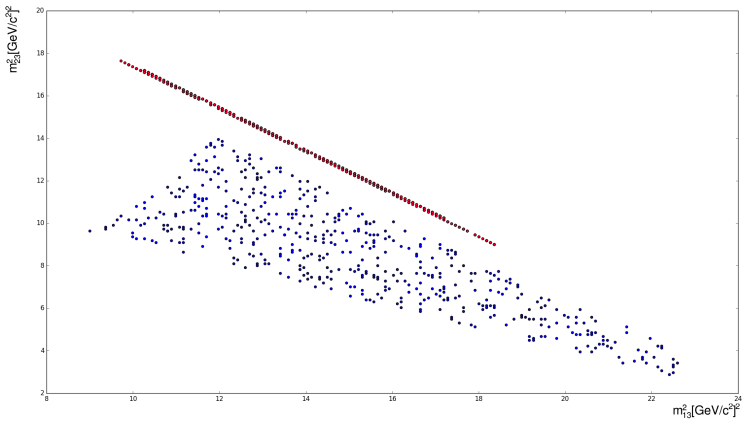

Figure III.4: I ran an algorithm to match together 2 points with correlation below 90%. We see that these points are chosen in the same kind of region - most of the time, one point is picked along a narrow resonance close to the edge of the Dalitz plane, the second point is then picked closer to the centre where the amplitude are usually quite low.

were to see repeatedly on a vast majority of the γ scans the behaviour shown in Fig. III.1, such conclusion could be drawn. Combining the fully-antisymmetric state with the fully-symmetric state could exclude some of the γ values that were found during the previous study.

This study has shown that extracting γ from a fit in the context of the antisymmetric state presents several pathologies. With the present available data, too little information can be extracted from the antisymmetric state. As most of the isobar contributions are vanishing when we build the antisymmetric state, the study is plagued by strong correlations and thus unstable fits. Even when stable fits were obtained, they were few well defined minima (see Fig. III.1), and these shallow minima have large uncertainties. This leads us to conclude that the contribution of the antisymmetric state alone to the extraction of γ is not significant.

III.3 Conclusion

We discussed in this chapter a method used to extract the CKM phase γ from a fit, relying on charmless 3-body decays of the B-meson, as described in Ref. [15]. The suggested method involves $B \to PPP$ decays. From the assumption

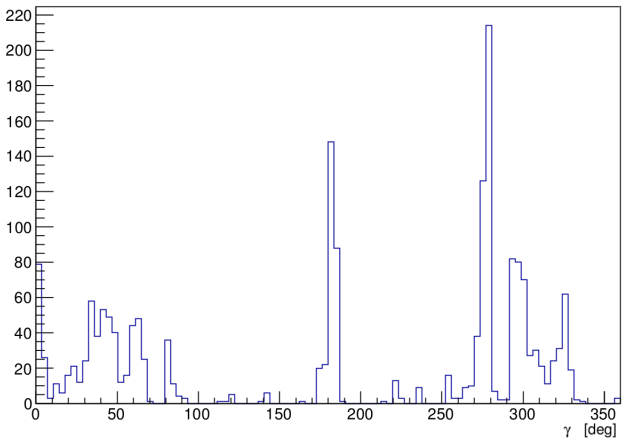

Figure III.5: Frequency of γ minima found in the context of the antisymmetric state, summing over 500 tests. This result was produced thanks to 500 sets of one single point.

that SU(3)-flavour holds, several symmetry state can be built. We focused on the antisymmetric state. Each amplitude of a decay that contribute to the antisymmetric state can be expressed as a set of diagrams, relative phases and γ. We used the amplitudes measured by BaBar (in Ref. [46–50]) to compute observables at various points in the Dalitz plane for the decays mentioned earlier. By expressing these observables in terms of the theoretical quantities that contribute to the amplitudes, we can obtain constraints on γ. The study I performed has shown that the antisymmetric state was not providing enough information to extract γ from a fit given the available experimental inputs. The antisymmetric state is prone to strong correlations between observables measured on several points over the Dalitz plane

We discuss a few points that could contribute to the production of probing results. The mixed states haven't been studied yet. Their study could bring new insight on the extraction of γ using the process we discussed in this chapter. Combining the symmetric state and the antisymmetric state could be a way to extract γ with a contribution from the antisymmetric state. It could help reducing the degeneracy of the measured γ values. Due to the timescale of my PhD, these perspectives could not be explored.

With the incoming run 3, we can expect new amplitudes analysis and new exciting results from the LHCb collaboration. A new description of the decay amplitudes of the mode we used in this study, with an increased statistics might also contribute to the feasibility of the antisymmetric state study.

Chapter IV

The LHCb experiment

The study of elementary particles and their interactions requires precise measurements of their properties. A detector such as LHCb has sub-detectors dedicated to measuring particular aspects of particles, such as their energy or, for charged particles, their trajectory. The information collected by these sub-detectors is then combined to identify particles and reconstruct the complete decay chain. We present in this chapter how the events that are necessary to LHCb studies are produced in the LHC and then collected by the LHCb detector.

In Sec. IV.1, a description of the Large Hadron Collider is given. The LHCb detector, its sub-detectors and its trigger system are then described in Sec. IV.2

IV.1 The LHC

The Large Hadron Collider [53] is the largest and highest-energy facility built to date to study elementary particles and their interactions. It has been built at CERN in Geneva in the tunnel in which LEP was formerly operating. The injection chain that was implemented for LEP is partly reused for the LHC. The Large Hadron Collider has been designed to accelerate protons and lead ions from 450 GeV to up to 6.5 TeV energies in the 27 km-long tunnel. Hadrons are accelerated at the LHC thanks to 16 radio-frequency cavities. 8.3T dipole superconducting magnets are bending the beam. Quadrupole superconducting magnets are employed to keep the beam focused and to correct its trajectory. The LHC beam energy was increased over the data-taking periods, which are devided into runs. Between each run, a long shutdown is held in order to fix or upgrade the accelerator and the detectors. Data have been collected by LHCb in 2011 and 2012 - we call this period the run 1 (small amounts of data were

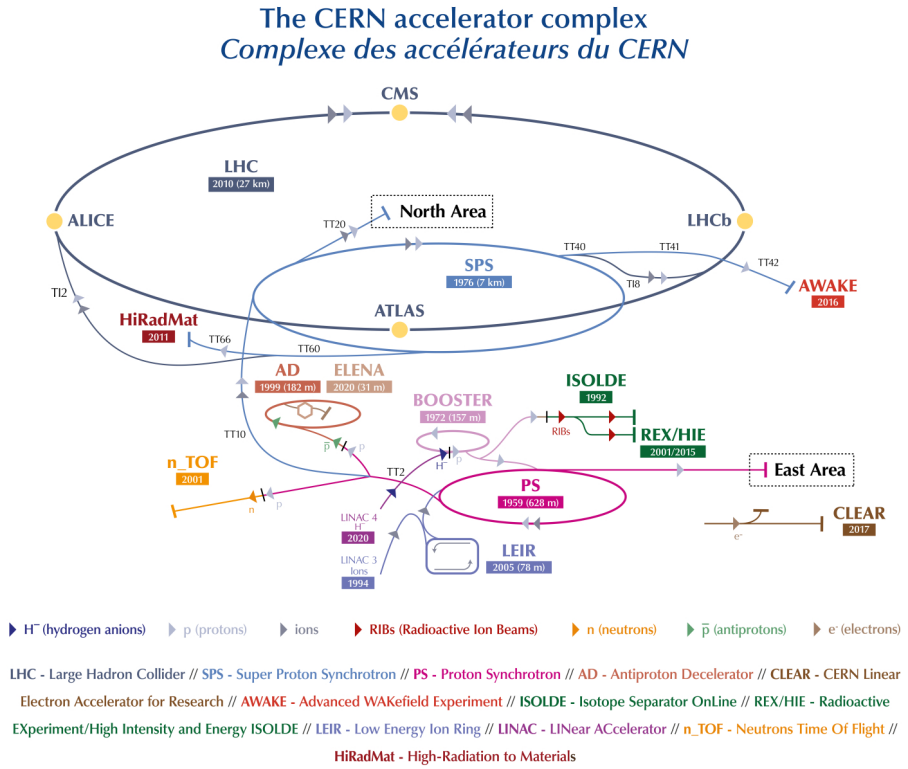

Figure IV.1: CERN accelerator complex. The four main experiments are shown along the LHC ring [54]

.

collected in 2009 and 2010 but are not used in this thesis, nor in other recent analyses). The energy at the interaction point was respectively 7 and 8 TeV. Then, collection happened from 2015 to 2018 - the run 2 - at 13 TeV.

The injection system of the LHC relies on a few smaller accelerators. The protons source is produced from ionised hydrogen gas. They are first accelerated to a 50 MeV energy by a linear accelerator, LINAC2. Then, the Proton Synchrotron Booster or PSB accelerates the protons to 1.4GeV. This synchrotron is also responsible for splitting the protons in bunch of around 10^{11} particles. The bunch separation at this point is set to an interval in-between bunch of about 25 ns. Right before they are injected into the LHC, the bunches are accelerated to an energy of 450 GeV thanks to the Super Proton Synchrotron or SPS. Figure IV.1 shows a schematic of the CERN accelerator complex.

LHC possesses 4 interaction points. Point 1 and 5 are respectively where the ATLAS [55] and the CMS [56] detectors stand. These experiments are general-purpose detectors. They participate to Higgs physics measurements as well as search for New Physics and top quark studies. They are also sensitive to flavour physics decays. On the 2 other interaction points lie ALICE [57] (point 2), dedicated mostly to heavy-ion collisions and quark-gluon plasma study, and LHCb [58] (point 8). LHCb is a spectrometer designed to study flavour physics. In the next section, we describe in further details the LHCb detector.

IV.2 The LHCb detector

The LHCb detector is a single-arm forward spectrometer. It is designed to cover only the region where b and c quark pairs are mostly produced. Indeed, the LHC has large beauty and charm cross-sections. Noting that the total cross-section of $p\bar{p}$ interactions is still way larger, studies performed with LHC collisions have usually large background. The LHCb detector is dedicated to the detection of beauty and charm decays: these types of decay usually have a secondary vertex well displaced from the primary vertex or interaction point. They also have generally a high transverse momentum. So far, 2 runs of data have been collected. From 2011 to 2012, a $3fb^{-1}$ integrated luminosity has been delivered to LHCb. The second run, from 2015 to 2018, has seen $6fb^{-1}$ of collected data. The integrated luminosity for each data-taking period is shown in Fig. IV.2.

LHCb's coordinate system is defined as follows: the z-axis is parallel to the beam axis. It is orientated from the VELO towards the muon stations. The y-axis is pointing upward in that system. With this definition, the magnetic field is bending in the xz plane. The geometry of the detector covers an angular acceptance of 15-300mrad in the plane where the magnet is bending the trajectories. In the perpendicular plan with respect to the plane we just mentioned, the angular acceptance is 15-250mrad. Figure IV.3 shows a view of the LHCb detector in the bending plane.

IV.2.1 The magnet

The LHCb detector has a dipole magnet situated downstream from the Tracker Turicensis stations. Its role is to bend the trajectories of all charged particles flying through the detector. This is achieved by generating a magnetic field perpendicular to the beam axis. The momentum of charged particles is mea-

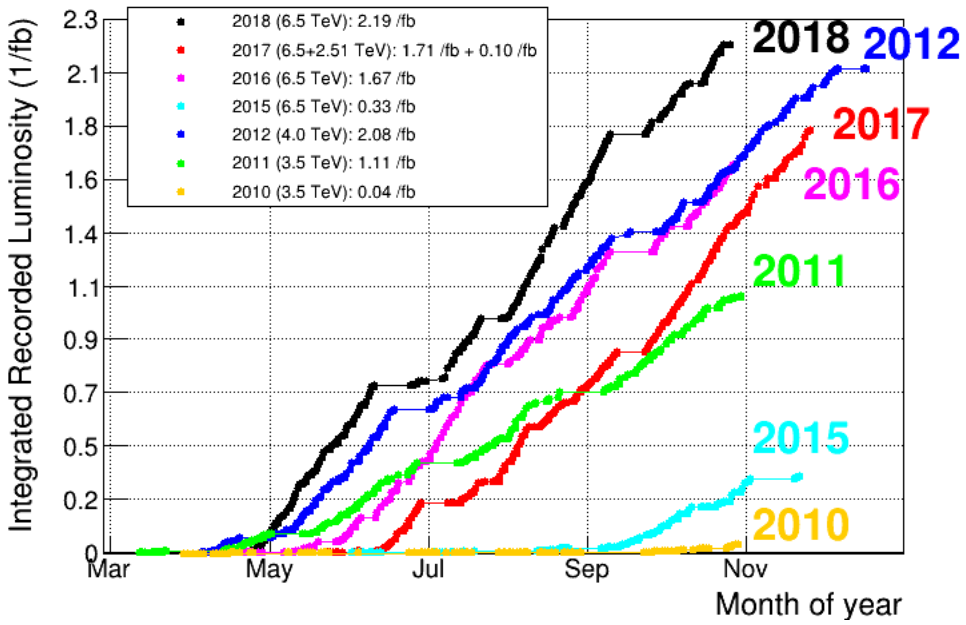

Figure IV.2: Integrated luminosity in fb^{-1} for each data-taking period.

sured thanks to the curvature of their trajectories. For a 10m-long track, the integrated bending power is at a level of 4 Tm. This allows to achieve a 5% relative precision on the momentum, to values up to 200GeV.

In order to evaluate possible detection asymmetries, the magnet can be operated in 2 magnetic field orientations, MagUp and MagDown. The magnet is composed by an iron yoke that maintains 2 saddle-shaped aluminium coils as shown in Fig. IV.4.

IV.2.2 Track reconstruction

The track reconstruction [60] is handled by the tracking system. The tracking system is the set of sub-detectors that were designed to reconstruct the trajectories of charged particles. We call these trajectories "tracks". Charged particles interacting with the material of these sub-detectors will leave hits in them. The tracks of the charged particles are then reconstructed thanks to the position of the hits. The momentum of a track is an observables that can be deduced from then bending of a track under the action of the magnet field. The tracking system's sub-detectors are:

- the VELO or Vertex Locator [61]. It is located around the interaction

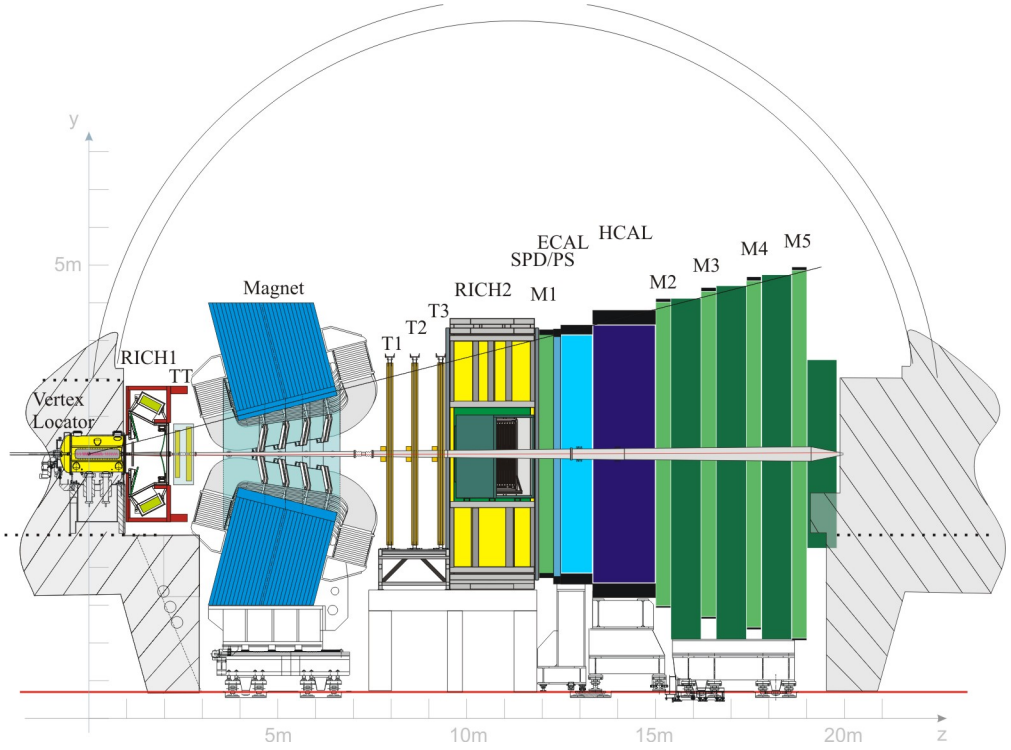

Figure IV.3: LHCb detector view in the bending plane. [59]

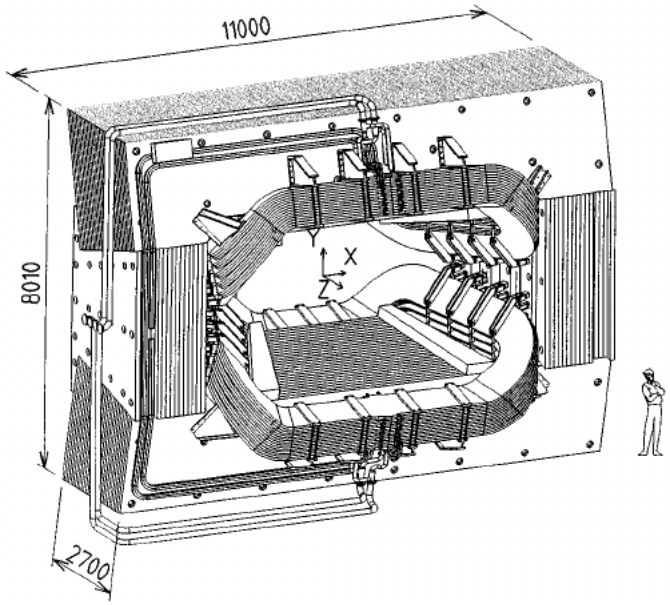

Figure IV.4: Schematics of the LHCb magnet.

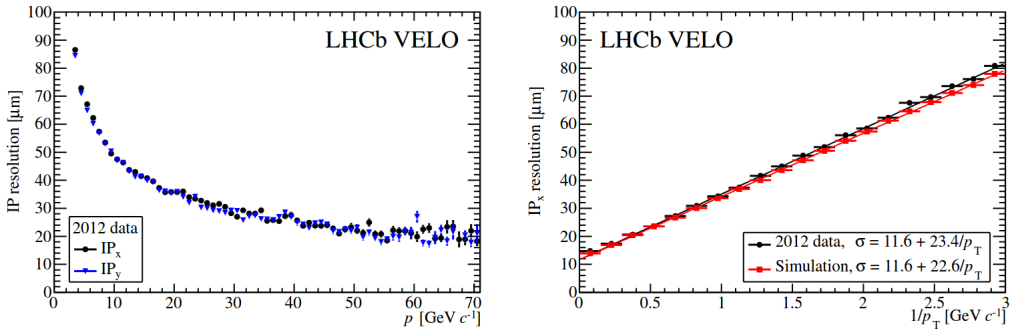

Figure IV.5: Resolution of the impact parameter. The left plot shows this quantity as a function of the momentum p of a track, the left plot shows the resolution of the impact parameter as a function of $1/p_T$. [62]

point

- the Tracker Turicensis, upstream from the magnet.
- the T-stations (T1, T2, T3). They are situated downstream from the magnet and are composed by the Inner Tracker and the Outer Tracker

We cover in the following sub-sections a broader discussion on each of these sub-systems.

The VErtex LOcator

The VErtex LOcator or VELO [61] is a silicon detector placed around the interaction region. Its aim is to measure precisely tracks of charged particles in this region in order to locate the primary and secondary vertices. The VELO is capable of separating the many vertices in the interaction region thanks to its resolution on the smallest distance of approach of a track to a vertex - we call this observable the impact parameter. The precision on this parameter is a function of the transverse momentum. Figure IV.5 shows the resolution of the impact parameter as a function of p and p_T.

The VELO is made of 21 stations aligned along the axis of the beam in the interaction region's direct neighbourhood as shown in Fig. IV.6. Each of these stations are composed by two semi-circular modules. The latter contain 2 types of sensor. The radial distance from the z axis, r, is measured by R sensors. The azimutal angle ϕ is measured by Φ sensors. Figure IV.7 shows a schematic of these sensors. Both types of sensors are built so that the silicon strips are

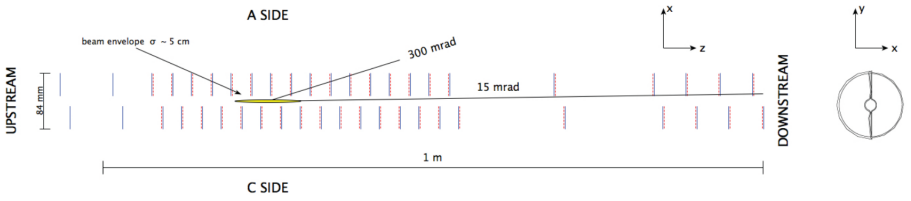

Figure IV.6: Transverse scheme of the VELO in the xz plane, at $y = 0$. The solid blue line are the R sensors, the dashed red line represent the Φ censors. The VELO is represented in its closed position. [62]

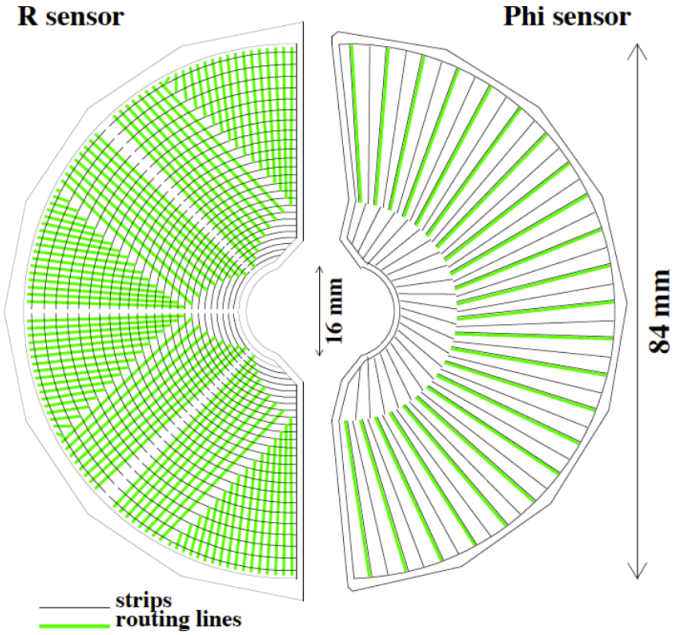

Figure IV.7: View of the Φ and R sensors. [62]

oriented in the direction of the coordinate the sensor is meant to measure. A track is "reconstructible" if a hit is left on at least 3 VELO stations.

The VELO has been built to ensure that any track within LHCb acceptance would fulfil this requirement. The VELO is designed to measure charged track coordinates as close as possible to the interaction region. To ensure that instability in the beam do not damage permanently the VELO, the stations can be retracted 35mm away from the beam.

Last, instantaneous luminosity measurement can be supported by the VELO. Indeed, 2 extra stations are situated upstream of the interaction point for that

purpose.

The Tracker Turicensis

The Tracker Turicensis detector or TT stations is a silicon tracker positioned upstream from the magnet. It is located downstream from the RICH1 sub-detector and covers the whole LHCb acceptance. It is composed by 4 layers of silicon micro-strip sensors. These layers are 150cm wide and 130cm high. The sensors them-selves are 9.64 cm wide, 9.44 cm long, and 500 µm thick. The layers are arranged in a particular geometry. They are disposed in a "x-u-v-x" layout in order to achieve a reasonably low resolution. The x-layers are vertical layers whereas the u- and v-layers are respectively rotated by a $+5°$ and $-5°$ - as well known as stereo angle. The TT stations have a central role in reconstructing tracks of long-lived particles such as neutral kaons. Indeed, such particles can decay outside of the VELO. The TT detector is also useful when reconstructing low-momentum-tracks and improves their quality.

Tracking stations

Downstream from the magnet are located 3 tracking stations, T1 to T3. Similarly to what has been done for the TT stations, each tracking station is made of 4 layers, placed in a x-u-v-x layout. Each of these stations is divided in an Inner Tracker and an Outer Tracker.

The Inner Tracker [63] is a silicon-based tracker. It is built of micro-strip. This technology ensures a finer granularity in the region close to the beam axis where large a occupancy is expected. The resolution of this sub-detector is comparable to the resolution of the TT stations.

The Outer Tracker [64] [65] covers the remaining LHCb-acceptance region that is left uncovered by the Inner Tracker. This region is expected to have a lower occupancy compared to what happens in the Inner Tracker region. Again, it is composed of 4 "x-u-v-x" layers. The occupancy is low enough so that these layers are made of drift-tubes - a coarser granularity is enough in this region of the detector. The drift-tubes are gaseous straw tubes. They re 2.4m long and their diameter is of 4.9mm. Double layers of such straw tubes are in place in each of the 4 layers, they are filled with argon (70%), CO_2 (28.5%) and O_2 (1.2%). This gas mixture ensures a drift time below 50 ns - it is low enough to cope with the bunch-crossing rate. The resolution of this technology is of about $200\mu m$. The position of an ionising particle is measured by the drift-time of the ions that are created when such particle pass through the tubes, ionising its content.

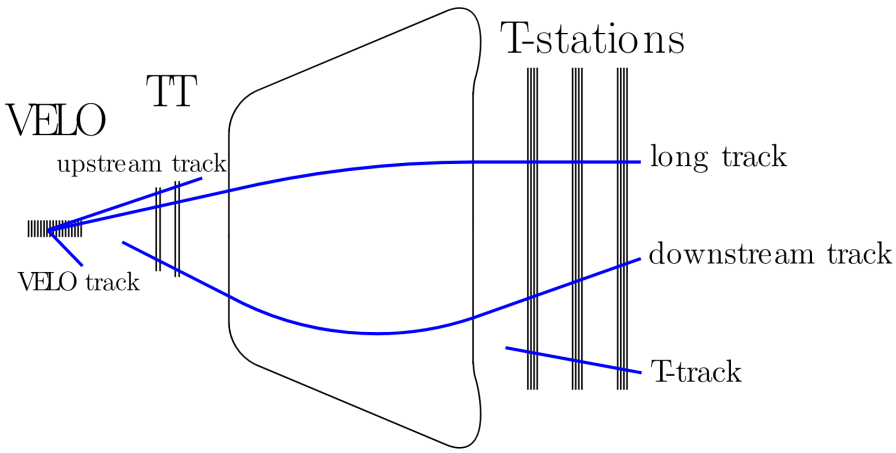

Figure IV.8: Track types in LHCb. [66]

Track types in LHCb

The tracks are reconstructed thanks to the combination of measurements done by each tracking sub-detector. Each sub-detector has its own precision on the track reconstruction. LHCb has then a classification to discriminate tracks depending on where they are in the detector. There are several classes of tracks, for example: Long tracks, Downstream tracks, T tracks and Muon tracks. Long tracks are tracks that deposited energy in at least the VELO and the T-stations. This type of tracks fly through the whole tracking system. Longtracks are used extensively in the $K^0_S h^+ h'^-$ analysis described in Chap. VI.As for the Downstream tracks, they go through the TT- and the T-stations but no hit are found in the VELO. These tracks are very useful when studying long-live particle such as neutral kaons. The different track types are illustrated in Fig. IV.8

IV.2.3 Particle identification

Particle identification in LHCb is done by the 2 Ring-Imaging Cherenkov (RICH) detectors, the hadronic (HCAL) and electromagnetic (ECAL) calorimeters, and the muon detector.

The RICH identifies charged particles thanks to the measurement of Cherenkov radiation angle of the particle going through them. Muon are identified by tracks in the muon chambers. The deposits of energy in the ECAL are used to find electrons and photons. Photons are classified as such thanks to the fact that they do not deposit any hit in the SPD and PS: a deposit in

the ECAL without any hit in the SPD or PS is most likely due to a photon. Charged particles are identified thanks to the combination of information of each sub-detectors into a multivariate analysis. The output of this machine learning tool are ProbNN and the $K^0_S h^+ h'^-$ analysis depends on them. The following sections cover in detail how each sub-detector is operated.

The Ring-Imaging Cherenkov detectors

The Ring-Imaging Cherenkov detectors or RICHs [67] are the sub-detectors responsible for the particle identification of charged hadrons: pions, kaons and protons. Information from these sub-detectors are combined with information from the calorimeters and the muon chambers in order to perform identification of leptons. The RICHs measure the angle with which the Cherenkov rings are produced. Indeed, when a particle flies through a material at a speed higher than the speed of light in the medium, a ring of Cherenkov light is emitted. Photons are emitted with an angle θ_c:

$$\cos\theta_c = \frac{1}{n\beta}$$

where n is the refractive index of the medium and β is the ratio between the particle velocity and the speed of light. The particle is then identified thanks the measurement of this ratio together with its momentum from which we deduce its mass. The Cherenkov angle as a function of the momentum for isolated tracks is shown in Fig. IV.9 The LHCb detector possesses 2 RICHs detectors, RICH1 and RICH2. Each detector is filled with a specific medium (or radiator) in order to be able to identify particles in various momentum regime. RICH1 is filled with C_4F_{10} that as a refractive index of n = 1.0014. In that situation, RICH1 is dedicated to the low and intermediate momentum region (2-40 GeV) over the full LHCb acceptance. RICH2 is composed of CF_4 for which the refractive index is n = 1.0005. This sub-detector covers the high-momentum region (15-100 GeV) on a portion of the LHCb acceptance (15-120 mrad). Both RICHs have a similar optical system. Mirror on the sides of the sub-detector reflect the emitted Cherenkov light towards hybrid photo-detectors, lying outside of the LHCb acceptance. With this system, the amount of material through which the particles should fly through is reduced.

Muon stations

In LHCb, 5 muon chambers are dedicated to muon identification. This information is then used in the trigger system. Muons are flying through most of

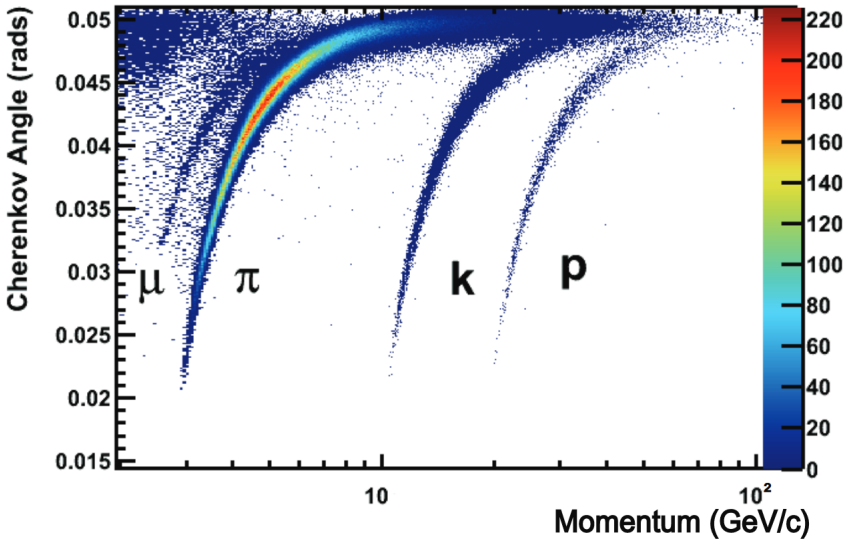

Figure IV.9: Cherenkov angle as a function of the track momentum p for isolated tracks in the C_4F_{10} radiator. [67]

the detector without being absorbed due to their low rate of energy loss. One of these chambers is placed before the HCAL. It ensures a better resolution of the transverse momentum of muons. For the other stations, most particles will have decayed before reaching them or they will have been absorb by the materials of the HCAL. The muon chamber closest to the interaction point is made of Gas Electron Multipliers as these are more robust to radiations. The 4 others chambers are Multi-Wire proportional chambers. In the interstice between each of these 4 stations, lie a layer of thick iron absorber to stop any remaining hadron.

IV.2.4 Calorimeters

The calorimeters are dedicated to the identification of electrons, photons and pions and to the measurement of the energy and position of the particles that fly through them. There are 2 calorimeters in LHCb: the electromagnetic calorimeter, ECAL, and the hadronic calorimeter, HCAL. On top of these 2 sub-detectors, the Preshower or PS and the Scintillating Pad Detector or SPD provides identification of neutral particles.

The SPD helps improving the separation of electrons and photons. The background generated by charged pions is reduced thanks to the PS. They are made out of lead scintillating pads that are 15 mm thick. This thickness

corresponds to 2.5 interaction length of an electron or a photon whereas it corresponds to 0.06 X_0 in the case of hadrons.

The ECAL is positioned right after the PS. It is made of 66 2mm-thick lead planes. In between each lead plane lies a scitillating pads of 4mm. These pads are perpendicular to the beam axis. The total thickness of the sub-detector corresponds to 25 interaction length of electrons and photons. The resolution of this sub-detector is at the level of $(10/\sqrt{E} \bigoplus 1.5)\%$ for E in units of GeV.

The HCAL is measuring the energy of incoming hadrons by absorbing it. It is composed of 26 layers of thin iron plates and scintillating tiles. These layers are set parallel to the beam axis. The energy resolution of this sub-detector is of $(80/\sqrt{E} \bigoplus 10)\%$, E in GeV.

IV.2.5 Trigger system

At the LHC, the luminosity and the collision rate are high enough so that we cannot write every single collision to disk. In order to save disk space, the LHCb trigger system has been implemented. It selects events that could contain interesting information for the physics analyses performed by the LHCb collaboration.

The LHCb trigger system is divided into 2 categories: hardware and software levels, more details are provided in Fig. IV.10. The L0 trigger is the only hardware level trigger in the trigger system. At this stage, the event rate is reduced to a level below 1 MHz. It is the largest frequency at which the LHCb detector can be read out. To ensure that the decision made by this trigger are taken fast enough, only partial information from the detector are implied in the decision. Mainly 4 L0 trigger lines have been designed: L0Hadron, L0Electron, L0Photon and L0Muon. Triggering is done by estimating the transverse energy deposited in the calorimeters. In the case of the muon, the transverse momentum estimated by the muon chambers is responsible for the trigger decision.

Then, the software level trigger is implemented in 2 sub-level, HTL1 and HLT2. In the case of these higher level triggers, a basic reconstruction of the events is performed. HLT1 performs a more simplistic reconstruction than HLT2: the trigger decision is made thanks to information from the VELO and the T-stations. The p_T, p, the distance to the PV and the track quality allow the HLT1 to perform a first filtering of the collected events. This ensure a low enough rate so that HLT2 can trigger on a full reconstruction of the events. This procedure reduce the data flow from around 1MHz to a few kHz. At this stage, a wide range of trigger decisions or trigger lines is available. The $K^0_S h^+ h'^-$ analysis relies on inclusive topological HLT lines [68]. These lines are

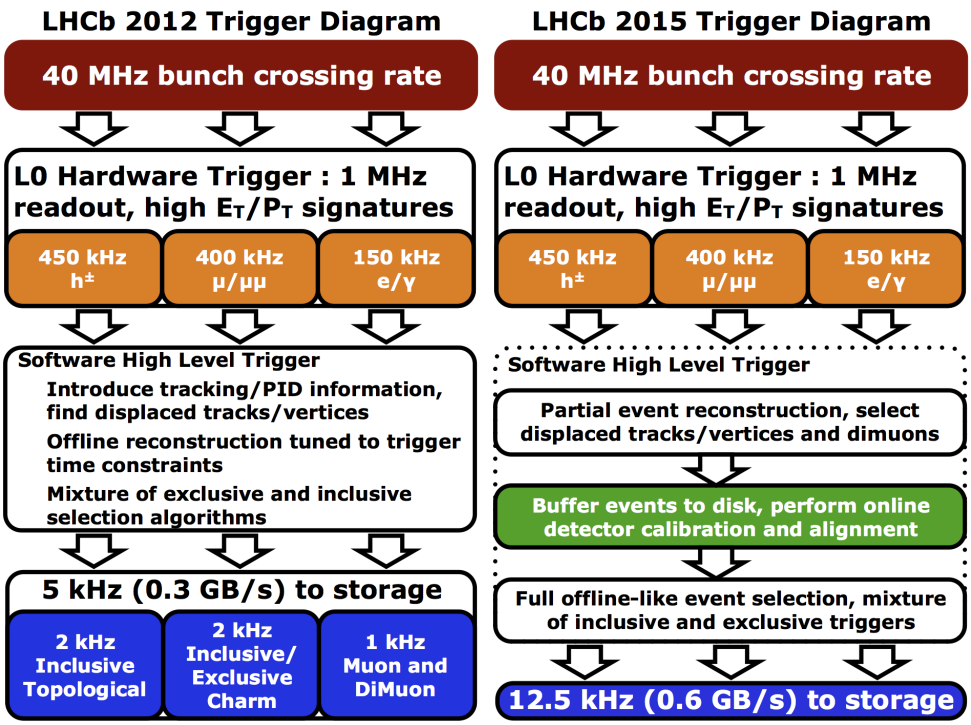

Figure IV.10: Run 1 (left) and run 2 (right) LHCb trigger system

designed to trigger on any generic n-body b-hadron decays.

Each trigger object should be associated with a signal track. A TOS event or Trigger On Signal event is an event for which the trigger decision was made on an event from the signal we want to study. The TIS or Trigger Independant of Signal category means that the trigger was activated by other particles in the event. Since multiple trigger lines can fire, the two categories are not mutually exclusive.

IV.2.6 Monte Carlo Simulation

Simulated data are necessary to study the efficiency of the selection of a physics analysis. They are also participating to the training of multivariate selections that allow to reduce the contribution from background events.

The PYTHIA [69] generator is responsible for the simulation of the collision. It generates also the decays of the particles produced in these collisions. A specific LHCb configuration [70] is implemented in PYTHIA 8. The content of the protons involved in the collisions is described by a parton distribution

function. The distribution is given as a function of the transverse momentum. PYTHIA handles the generation of the partons showering as well as their hadronisation and interactions. EVTGN [71] package is responsible for the decays of hadronic particles. The final states radiation are simulated by the PHOTOS [72] generator. The GEANT4 toolkit [73] [74] simulate the LHCb detector: it handles the interactions between the particles and the detector and the detector response. Reference [75] gives a description of the GEANT4 implementation to simulate the LHCb detector.

We presented in this chapter the LHCb detector as it was when collecting run 1 and run 2 datasets. The LHCb collaboration is now preparing for a new data-taking period. We present briefly in the next chapter the new detector. We discuss more particularly the new downstream tracker, the scintillating fibre tracker, and the upgrade developments to which I participated.

Chapter V

The Scintillating Fibre Tracker

The LHCb collaboration collected an integrated luminosity of 5.4 fb^{-1} during run 2, from 2015 to 2018, which brings the total amount of data registered to 9 fb^{-1}. This performance gave the opportunity to the collaboration to bring hints for physics beyond the standard model. In particular, tensions were observed in lepton flavour universality tests [7, 76] and the Kπ-puzzle was confirmed with an unprecedented precision [77]. Precision measurements of standard model processes were also achieved, such as the $B_s^0 \to \mu^+\mu^-$ decay rate and effective lifetime [78], measurements of CKM parameters, observation of *CP* violation in charm sector [79] and more.

Run 2 was clearly a successful data-taking period with respect to the collected integrated luminosity and the physics studies that were performed. Furthermore, the broad physics programme of LHCb could give more insights on possible scenarios of new physics, via more sensitive channels, as well as more precision measurements of standard model parameters. All this provides a strong motivation to enlarge the available data set.

The LHCb collaboration plans to start a new data-taking period in 2022 after a long shutdown of more than three years, during which the upgraded detector is being installed. During the upcoming LHC runs: run 3, from 2022 to 2024, and run 4, from 2028 to 2030, the LHCb collaboration aims to operate its detector at an instantaneous luminosity of $\mathcal{L} = 2 \times 10^{33}$ cm^{-2} s^{-1} [80], which is five times larger than that of the previous runs. At this rate, the LHCb collaboration plans to accumulate 50 fb^{-1} by 2030 [80].

The measurements discussed above, among others, have potential for bringing hints of physics beyond the standard model. According to the logic of indirect searches of new physics, the discovery potential depends on the sample size. In general, LHCb's new-physics searches are limited by the statistical

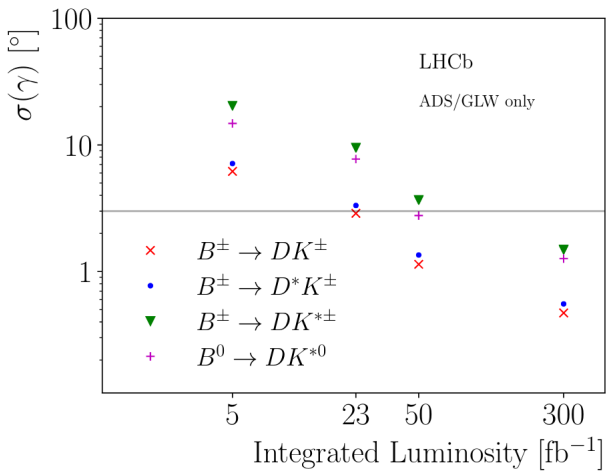

Figure V.1: Extrapolation of the precision on γ as measured according to the ADS/GLW methods. The horizontal grey line is the expected Belle II sensitivity at an integrated luminosity of 50 ab^{-1} [81].

uncertainty. With the planned 50 fb^{-1} integrated luminosity, precision on the $B_s^0 \to \mu^+\mu^-$ effective lifetime could reach a 8% level, to be compared to the 22% [81] precision obtained with the run 2 data. At the end of the run 4, the precision achieved on R_K and R_{K^*} could be almost one order of magnitude better than what is available today. Figure V.1 shows an extrapolation on the measurement of the CKM angle γ. From ADS and/or GLW analyses, the sensitivity on γ is expected to be around one order of magnitude better when the integrated luminosity would reach 50 fb^{-1}.

The upgraded detector is, to some extant, a new experiment operating with a new logic. It has a full software trigger system that reads out the detector at the bunch-crossing rate of 30 MHz. To cope with the larger rates and occupancy, a few subdetectors, as the scintillating fibres (SciFi) tracker, has been changed and others have undergone major upgrades.

The LHCb group at LPNHE was implied in two aspects of this upgrade: the first-level trigger system and the readout (back end) electronics of the SciFi detector. I participated in the latter, more precisely in the development of monitoring and calibration.

Sec. V.1 is dedicated to a brief description of the LHCb upgrade, and Sec. V.2 brings more details on the design of the SciFi tracker: we briefly present there the layout of the subdetector and the challenges that it has to meet. We then introduce the characteristics and material of the scintillating fibres. This second section ends with a description of the electronics of the

subdetector. Then, in Sec. V.3, we discuss the developments of the monitoring and the calibration to which I contributed. These developments have been performed thanks to the supervisory control and data acquisition application WinCC OA. We introduce this tool first. Then, we present the monitoring panel that has been developed at LPNHE. The SciFi working group developed an algorithm to calibrate the subdetector. At the end of the section we introduce this algorithm and discuss the developments and updates done at LPNHE.

V.1 The LHCb upgrade

The first point to mention about the LHCb upgrade is the increase in the efficiency of the trigger system in order to better benefit from the delivered luminosity, with less limitations. One main ingredient in order to achieve this is the replacement of the hybrid hardware and software trigger system by a full software trigger system, that will read out the detector at the 30 MHz rate of bunch crossing. The front-end electronics are being updated accordingly. This implies that the full event needs to be reconstructed and sent to the data collection farms at a rate compatible with the bunch crossing rate.

In addition, in order to cope with the increased rate and occupancy, LHCb has undergone a major upgrade of nearly all the subdetectors.

The upgraded VELO will consist of 26 planar stations of hybrid silicon pixel detectors (to be compared to the 21 stations in the original detector, each station was made of a double layer of silicon micro-strip sensors). In total, 41 million pixels compose this new subdetector. The detector will be operated even closer to the beam than before. The active area will be as close as 5.1mm to the beam (versus 8.2mm before). The thickness of the material that separates the detector from the beam will be reduced. These two last points allow an improvement of the impact parameter resolution compared to the original detector.

The Upstream Tracking station is set in place of the TT subdetectors. The layout of this new subdetector consists of four detection layers composed by silicon microstrip detectors, comparably to what was done for the original detector. Similarly to the situation before the upgrade, the region of the subdetector where the highest particle densities are expected are populated by shorter strips. However, the upgrade subdetector is now composed by 537 000 strips (compared to 143 000 previously). This finer grained detector allows for a reduction in the rate of the wrongly reconstructed track candidates.

The scintillating fibres (SciFi) tracker replaces the T-stations. Its geometry will be relatively similar to what was done for the tracking station. In both

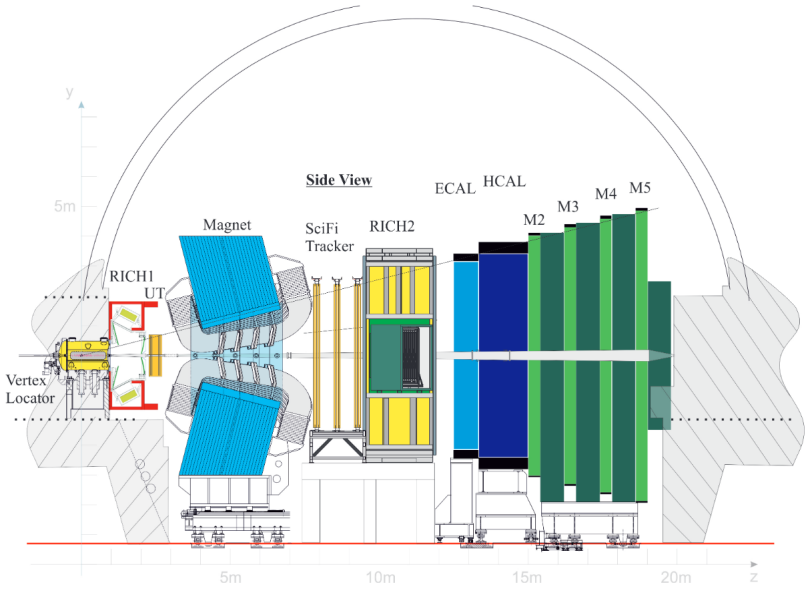

Figure V.2: Schematical view of the LHCb upgraded detector [80].

case, the downstream tracker is composed by three tracking stations, each stations being composed by four planar detection layers. Each detection layer are composed now by scintillating fibres ; we note that the former downstream tracker was made of two technologies: the inner tracker was a silicon micro-strip detector while the outer tracker was made of straw drift-tubes. The scintillating fibres of the new subdetector are 250 μm thick and 2.5m long.

The new RICH subdetectors will be using the same gas radiators that was used in the original RICHs. The RICH 1 will see a new light-collecting system.

The calorimeters from before the upgrade are kept as they are. The PS/SPD system will be removed as its purpose was to provide information to the L0 hardware trigger.

The M1 station of the muon system is removed for the upgrade as it was serving hardware trigger purpose only. The other stations are kept and only the innermost region of the M2 station is being upgraded to cope with the new data-taking conditions.

Figure V.2 shows a scheme of the LHCb upgraded detector.

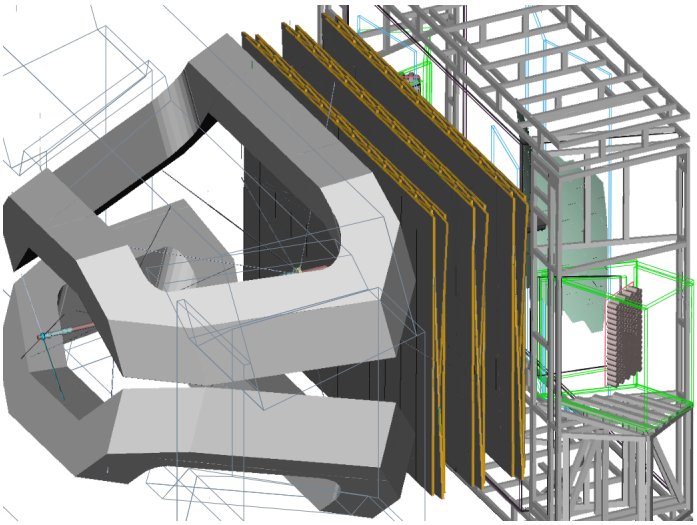

Figure V.3: The Scintillating Fibre Tracker or SciFi tracker is situated upstream from the magnet and downstream from RICH2. It is made of 3 tracking stations. Each of these stations is composed of 4 independent layers. These layers contain the active material, e.g. 250 μm thick and 2.5 m long scintillating fibres [80].

V.2 The Scintillating Fibre Tracker design

As I am writing these lines, the SciFi tracker is being installed. Like the old tracking stations that it replaced, the SciFi is situated between the magnet and the RICH 2, as shown in Fig. V.3. It covers the whole LHCb acceptance. It is made of 2.5 m long scintillating fibres [80], the diameter of which is 250 μm [80]. The scintillating fibres are read-out by Silicon Photo-multipliers, or SiPMs. The latter are contained in "Read-out Boxes" placed at the top and the bottom of the subdetector. They are lying outside of the detector acceptance in order to reduce the interaction with the material that particle flying through the detector can undergo.

The SciFi tracker is made of 3 tracking stations (T1-3), each of which is composed of 4 independent layers. Comparably to the tracking stations, these layers are arranged in a x-u-v-x disposition where x are layers where the fibres are oriented vertically, and the other layers are angled by so called stereo angles of +5° and -5° for u and v, respectively. In total, 128 modules compose the SciFi tracker.

The SciFi tracker has to meet few requirements. It is expected to have a high hit efficiency to ensure a well-performing particle tracking. It has been designed to have an as large as possible hit efficiency ($\approx$ 99% [80]), while

keeping a noise cluster rate reasonably low, at the level of $\leq$10% of the signal rate. The spatial resolution should be reasonably good in the bending plane of the magnet to allow for precise momentum measurements. The sub-detector has a spatial resolution that is better than or equal to 100 μm [80]. As discussed above, a low material density within the acceptance is required to minimise scattering effects. The mean interaction length is $\mathrm{X}/X_0 \leq 1\%$ [80] per detection layer.

The tracker can operate at a 40MHz bunch-crossing rate. It should maintain good performance on track reconstruction during the whole LHCb upgrade lifetime, despite the fact that radiation affects its performance.

Scintillating fibres

Scintillating plastic fibres are the active material of the SciFi tracker. As previousely mentioned, they have a diameter of 250 μm [80]. Scintillation happens when an ionising particle deposits energy in the SciFi polymer. Such a polymer has a poor light yield. To improve the scintillation efficiency, an organic fluorescent dye is added to the polystyrene. In order to limit the re-absorption of the scintillation photons, a second dye is used as a wavelength shifter. Similarly to what happens in optic fibres, photons are propagated along the scintillating fibres due to a difference between the core and the coating refraction factors.

SiPMs

Silicon photo-multipliers, or SiPMs, are solid-state photon detection devices that collect the signal produced in the scintillating fibres. They were built to have a high photo-detection efficiency. Their low cost allows to build a large tracking device.

Front-end and back-end electronics

The front-end electronics is responsible for the digitisation of the SiPMs signal at a 40 MHz frequency. It is located outside of the acceptance of the detector. Its core front-end chip is the PACIFIC (low Power Asic for the SCIntillator FIbres traCker) that has the function of digitising analogue signal received from the SiPMs. Each chip is dedicated to the clusterisation of 128 SiPM channels. Thanks to a light injection system, precise measurements of the gain can be performed in-between runs.

The front-end cards contains also Field Programmable Gate Arrays or FPGAs, which are responsible for the clusterisation of the hits in the SciFi

tracker. The cluster size is limited to four channels. This ensures that we minimise the use of logic resources in the FPGAs. They also suppress noise from false hits (zero suppression).

Finally, a GigaBit Transceiver ASICs or GBT ASICs handle the encoding of the clusterisation data and its distribution to the back-end electronics through optical links.

TELL40 are back-end read-out electronic boards. They receive the data packets from the front-end as encoded by the GBT, through optical links. Each TELL40 board can handle up to 24 GBT optical links. it realigns the data packets following their Bunch Crossing ID or BCID. The data flow can be monitored at the level of the TELL40 boards. Then, events that pass the Low-Level Trigger are sent to the DAQ farm as Multi-Event Packets (MEP) through output optical links where the events will be further processed for triggering.

V.3 SciFi monitoring and PACIFIC calibration

I participated in the development of an online application to be used in the control room to monitor the SciFi data processing. I also contributed to the update of the PACIFIC calibration process at the software level. First, I discuss the tools that were employed for these developments. I then detail my personal contributions.

V.3.1 WinCC OA and the JCOP framework

The monitoring and operation of the SciFi is performed thanks to the WinCC OA application. The LHCb LPNHE group is responsible for developing and maintaining an expert-level monitoring panel for the backend in WinCC OA.

WinCC OA (previously known as PVSS) is a supervisory control and data acquisition, or SCADA, system developed by Siemens. This SCADA system can operate with large distributed systems such as the multiple sub-detectors of a particle-physics detector. It is aimed to build control systems dedicated to the interaction, for example with a detector (i.e. monitoring, alarm display,...). It is also possible to build a user interface thanks to WinCC OA, such as the panel that will be described below.

Systems in WinCC OA are organised around managers. This ensures a great scalability of systems due to the fact that managers can be spread across several machines.

The Event Manager is the core manager of any WinCC project, There is only one instance of this type per project, which is aimed at assuring the communication between the other managers thanks to 'events'.

The database manager handles a database that keeps track of the status of a system. This is done by storing in a database the most recent known states of variables in a system, as well as the state of other features such as alarms.

Then, User-Interface managers allow to design panels and write panel scripts. These scripts can be executed when an interaction with a panel occurs or when the panel is opened by the user for example. They also handle the display of these panels when the project is running as well as executing scripts linked to panels' widgets. User-Interface managers interact with the Event Managers to display relevant information and communicate users input to the system.

Scripts that do not need keyboard input or screen output are handled by the Control Manager. It is also responsible to run scripts triggered by events.

Then Driver Managers are employed in order to convert values or transform the data type (hexadecimal to binary for example).

Building a large system with redundancy is made easy by the JCOP framework. Indeed, the JCOP framework allows to create a set of tools in order to build a control system and to share it. This set can contain all the scripts, software and panels necessary to monitor and operate a sub-detector for example. JCOP makes the deployment of panels to a new set-up easy.

V.3.2 Monitoring Panel

I participated in the development of an expert-level monitoring panel that allows the monitoring of several SciFi parameters in the LHCb control room. WinCC OA can access in real time the SciFi FPGA addresses where the value of these parameters are stored. The panel is developed on a mini-DAQ 2 system. A mini-DAQ is a minimal testing board, containing a TELL40 board and a GBT server, that was used in the LPNHE to develop and test the SciFi software and firmware. All the developments related to the SciFi panel were produced and tested on the LPNHE mini-DAQ 2 system before we tested them on the actual SciFi set-up. The panel has been included in the JCOP framework as a component. This allowed to deploy it on setups at CERN to test its behaviour with the sub-detector's front-end. Figure V.4 shows the panel and illustrates its functions. One of them is to monitor the statistics of the sub-detector, such as the output rate or number of output events. The panel also gives the status of the sub-detector. For example, if an error occurs, the error register value allows to identify the nature of the error. Another part of this panel is dedicated to calibration, which is described in the next paragraph.

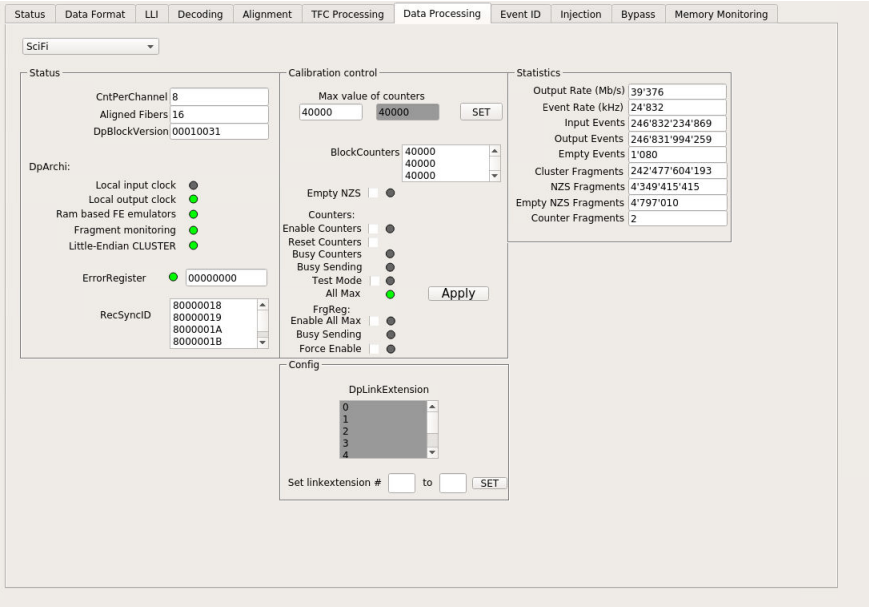

Figure V.4: Screenshot of the dedicated SciFi panel. It has been designed to monitor statistics of the sub-detector (number of events, events rate,...), check the error status and control the calibration process.

V.3.3 The calibration

The calibration of the PACIFIC is performed in between data-taking runs thanks to the so called "step-runs". These are employed to obtain a conversion between the ADC unit, given as an output of the PACIFIC chips, and the corresponding number of photo-electrons from the SiPMs.

The calibration of the PACIFIC modules proceeds as follows. Pulsed light is injected in the sub-detector by the light-injection system at each step during a step-run. The amplitude of the output signal from the SiPMs is compared to a threshold. This threshold is set to consecutive values in a range of ADC (Analogue-to-Digital Converters) outputs, each value corresponding to a step. At each step, the number of events collected at the step's threshold value is measured. This produces at the end of the step run the light spectrum shown on Fig. V.5. Once the full range of threshold values has been studied, the threshold scan S-curve can be produced. The S-curve shown at the bottom of Fig. V.5 is produced by computing for each threshold value the difference between the total number of events and the sum of events bellow the threshold, normalised to the unity. As the threshold increases, the difference described above decreases. The signal from the injected light causes the decreasing ratio

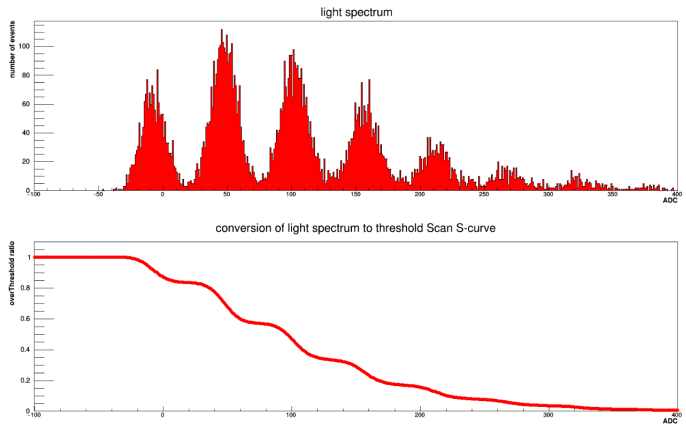

Figure V.5: Example of a light spectrum (top) and an S-curve (bottom) produced during a threshold scan. Threshold scans are performed in order to calibrate the PACIFIC module. Thanks to this calibration, we can obtain an equivalence between the ADC units and the number of photo-electron received from the SiPMs [82].

to take the shape of an "S-curve": the threshold scan follows a step function as shown in Fig. V.5. The first peak in the light spectrum corresponds to noise. Then, the signal can only trigger the emission of an integer number of photo-electrons. Each sharp transition line tells us that signals above the corresponding threshold will trigger the emission of a given number of extra photo-electrons, corresponding to the position of the photo-electron peak. From this process, called a threshold scan, we can obtain a conversion from ADC units to number of emitted photo-electrons. From a fit to the threshold scan, detector characteristics are extracted such as the SiPM gain or the light yield for example. The threshold is then set to match the requirement of the clustering algorithm. Indeed, the threshold needs to be set to limit the count of false hits without compromising to much the hit efficiency.

Step runs can be performed in various configurations. For example, they can be performed automatically. At the end of each step, the new threshold is set automatically and the data-taking is performed. I participated in updating and maintaining the step-run procedure. The main goal was to have this process running with the final FPGA firmware. Alternative configurations were also implemented to allow for debugging or to reduce the bandwidth used by the step run process.

Chapter VI

Measurements of the branching fractions of $B^0_{(s)} \to K^0_S h^+ h'^-$

The LHCb collaboration has been performing a broad study of the properties of B mesons, and has found tensions with the Standard Model. For example, the ratio R_K (see Ref. [76]) is currently measured to be approximately 3σ from the Standard Model prediction, following a pattern of other hints of new physics. Further studies of this quantity may challenge the Lepton Flavour Universality embedded in the Standard Model. However, this is just one example of a heavy flavour measurement sensitive to new physics. The B-meson sector is rich in observables that might present discrepancies with the SM predictions. Many of these quantities are still to be studied, and many b-hadron decays are still unobserved. In the case of suppressed decays, such as decays of b-hadrons to charmless final states, an important first step is to determine the decay rates, in the form of branching fractions.

This analysis aims to measure the branching fraction of B^0 and B^0_s decays of the form $B^0_{(s)} \to K^0_S h^\pm h'^\mp$ where h and h' are either a kaon or a pion, relatively to the $B^0 \to K^0_S \pi^+ \pi^-$ branching fraction. A previous iteration of this analysis was performed on the run 1 data collected by LHCb, using a data set of 3 fb^{-1}. The results were published in Ref. [10]. The ratios of branching fractions of all the $K^0_S h^+ h'^-$ decays relatively to the $B^0 \to K^0_S \pi^+ \pi^-$ branching fractions were measured. The $B^0_s \to K^0_S K^+ K^-$ decay is left unobserved as the significance of this signal was found to be at a level of 2.5σ. The results that were obtained are the following, where it is clear that the ratio of the branching fractions of $B^0_s \to K^0_S K^+ K^-$ over that of $B^0 \to K^0_S \pi^+ \pi^-$ was measured to be compatible with 0:

$$\frac{\mathcal{B}(B^0 \to K^0_S K^+ \pi^-)}{\mathcal{B}(B^0 \to K^0_S \pi^+ \pi^-)} = 0.123 \pm 0.009\,(\text{stat}) \pm 0.015\,(\text{syst}),$$
$$\frac{\mathcal{B}(B^0 \to K^0_S K^+ K^-)}{\mathcal{B}(B^0 \to K^0_S \pi^+ \pi^-)} = 0.549 \pm 0.018\,(\text{stat}) \pm 0.033\,(\text{syst}),$$
$$\frac{\mathcal{B}(B^0_s \to K^0_S \pi^+ \pi^-)}{\mathcal{B}(B^0 \to K^0_S \pi^+ \pi^-)} = 0.191 \pm 0.027\,(\text{stat}) \pm 0.031\,(\text{syst}) \pm 0.011\,(f_s/f_d),$$
$$\frac{\mathcal{B}(B^0_s \to K^0_S K^+ \pi^-)}{\mathcal{B}(B^0 \to K^0_S \pi^+ \pi^-)} = 1.70 \pm 0.07\,(\text{stat}) \pm 0.11\,(\text{syst}) \pm 0.10\,(f_s/f_d),$$
$$\frac{\mathcal{B}(B^0_s \to K^0_S K^+ K^-)}{\mathcal{B}(B^0 \to K^0_S \pi^+ \pi^-)} \in [0.008 - 0.051]\,\text{at a } 90\%\,\text{confidence level.}$$

In this chapter, we present an update of the analysis that includes data taken during run 1 and run 2, measuring the ratios of branching fractions with a much larger data set. We expect that with this increased integrated luminosity, the decay $B^0_s \to K^0_S K^+ K^-$ will be observed for the first time, and that the precision on the ratios of branching fractions will be greatly improved.

We begin this chapter with a brief discussion on the analysis strategy (Sec. VI.1). We then present in Sec. VI.2 the trigger and stripping selection: the loose selection applied to events at the very first stages of the data taking process. This selection is implemented so that we write on disk only the events that may contain physics that is relevant to LHCb studies. In Sec. VI.3 we present the dedicated $K^0_S h^+ h'^-$ selection. It is a based on a multivariate analysis (MVA) that aims to maximise the $K^0_S h^+ h'^-$ signal significance over the background contribution. We detail the results of the MVA and its optimisation. The logic behind the selection is quite similar to what was done in the previous analysis, where a multivariate analysis was also performed to separate signal events from combinatorial background. In the present analysis, we improve the selection by implementing boosted decision trees to discriminate background from crossfeed events. Once we have chosen the selection cuts on the MVA output so that we maximise the significance of signal events over background events, a simultaneous fit to the B-meson invariant mass is performed, as detailed in Sec. VI.4. The key benefit of the $K^0_S h^+ h'^-$ simultaneous mass fit is the constraints that it allows to set on crossfeed yields. Next, sWeights are derived from the fit results. They are weights that we use to describe the distribution of the signal and background events in the square Dalitz-plane. Further details can be found in Sec. VI.5. Measuring branching fractions requires a detailed knowledge of the efficiency distribution over the Dalitz plane. The efficiency maps we build take into account effects such as LHCb

acceptance, pre-selection and selection cuts. We also correct the Monte Carlo samples to take into consideration any discrepancies between the data and simulated events. The efficiency and Monte Carlo correction studies are detailed in Sec. VI.6. We discuss the systematic uncertainties in Sec. VI.7. Results are given in Sec. VI.8.

VI.1 Discussion on the analysis strategy

The aim of the present analysis is to update the measurements of the branching fractions of the decays $B^0_{(s)} \to K^0_S K^\pm \pi^\mp$, $B^0_s \to K^0_S \pi^+ \pi^-$, and $B^0_{(s)} \to K^0_S K^+ K^-$, relative to that of $B^0 \to K^0_S \pi^+ \pi^-$. It is an update of an earlier LHCb analysis, performed using the run 1 data sample, corresponding approximately to an integrated luminosity of 3 fb^{-1} [10]. In this previous analysis, the significance of the measured signal yield for the decay $B^0_s \to K^0_S K^+ K^-$ was found to be only 2.5σ, and a 90% confidence level interval was set for the branching fraction, relative to that of $B^0 \to K^0_S \pi^+ \pi^-$. Figure VI.1 shows the fit to the $B^0_{(s)} \to K^0_S K^+ K^-$ invariant mass distribution from this previous paper, corresponding to a data sample from 2011, with downstream K^0_S. As the $B^0_s \to K^0_S K^+ K^-$ decay mode has not been observed yet, in the present analysis we blind its region in the fit to the data.

The measurement of the branching fractions of $B^0_{(s)} \to K^0_S h^+ h'^-$ performed here includes the run 2 data on top of the run 1 data that was previously studied. In total, the analysis is performed with a 9 fb^{-1} data set. In addition to signal events, the data samples contain various sources of background events that pollute the $K^0_S h^+ h'^-$ spectra. These include combinatorial, crossfeed, charmed, and partially-reconstructed background events. We implement dedicated strategies to reduce the contribution of the combinatorial, crossfeed and charmed backgrounds.

Combinatorial background arises from the random association of a pair of charged hadrons with a K^0_S. A pre-selection is applied to the data events so that the contribution of combinatorial events is reduced. Crossfeeds appear when one of the daughter particles is misidentified. For example, a kaon produced in $B^0_{(s)} \to K^0_S K^+ K^-$ that is reconstructed as a pion will contribute to the $B^0_{(s)} \to K^0_S K^+ \pi^-$ decay spectrum as a background.

The methods employed to reduce the contribution of combinatorial and crossfeed background events are similar. Two multivariate analyses, as discussed in Sec. VI.3, are implemented. Each multivariate selector combines a set of discriminating variables into a single output variable. The two selectors that we trained are referred to as "topological" and "particle identification" selectors,

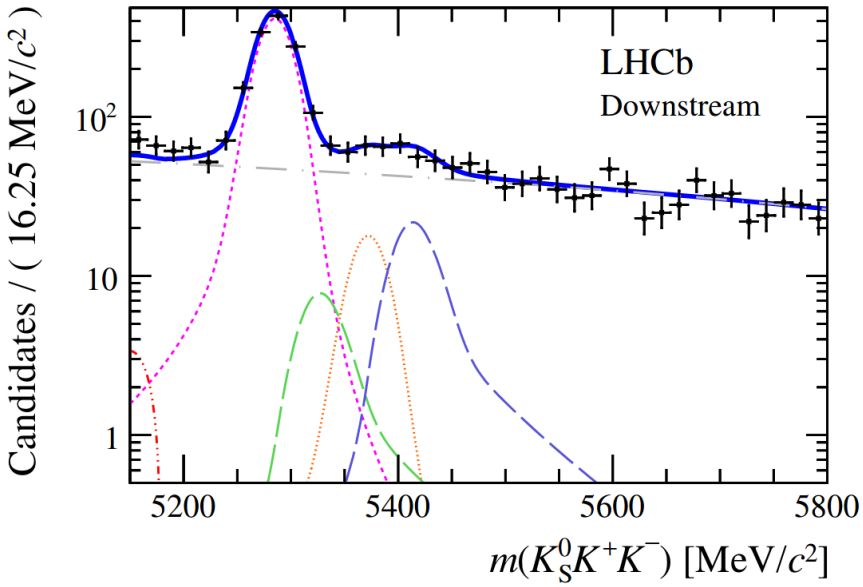

Figure VI.1: Fit of the invariant-mass distribution of $B^0_{(s)} \to K^0_S K^+ K^-$ candidates with Downstream (DD) K^0_S (see definition below), in events from the year 2011. This result is taken from the run 1 $K^0_S h^+ h'^-$ study [10], in which the $B^0_s \to K^0_S K^+ K^-$ signal was found to have a 2.5σ significance. The B^0 signal is represented by the magenta line and the yellow line is the B^0_s signal distribution. The red dashed line is the partially reconstructed background contributions. The crossfeed distributions are represented by the blue and green dashed lines. The combinatorial background is the grey straight line.

according to the type of discriminating variables that were used to train them. The selection is performed thanks to topological variables when the aim is to reduce contributions from combinatorial events. We then use particle identification quantities to remove crossfeed events. We apply a cut on the selectors output variables to minimise the contribution of combinatorial and crossfeed events. The cut is chosen such that the significance of the signal over the background is maximised, by a 2-dimensional optimisation of both multivariate selectors simultaneously. The optimisation relies on finding the maximum of a figure of merit (FoM). For an already observed decay mode, we maximise

$$FoM = \frac{S}{\sqrt{S+B}}, \tag{VI.1}$$

where S and B are, respectively, the number of signal and background events

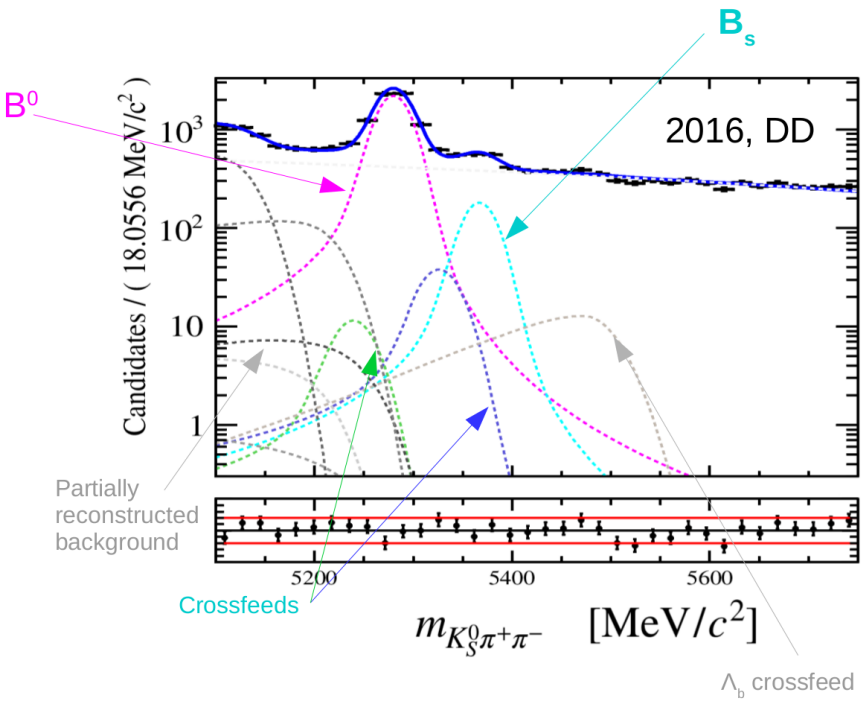

Figure VI.2: Fit of the invariant-mass distribution of $B^0_{(s)} \to K^0_S\pi^+\pi^-$ candidates with Downstream (DD) K^0_S (see definition below), in events from the year 2016. This plot, where all components are identified, illustrates the fit model.

once we apply the selection, in a given region around the signal peak. The number of signal events

$$S = S_0 \times \epsilon_{\text{selection}},$$

is computed at each point considered for the 2-dimensional optimisation. In this equation the $\epsilon_{\text{selection}}$ term is the efficiency of the BDT cuts estimated from simulated data. The expected number of signal events is computed as

$$S_0(B^0_{(s)} \to K^0_S h^+ h'^-) = 2 \times \sigma(b\bar{b}) \times \mathcal{L} \times$$
$$\times \mathcal{B}(B^0_{(s)} \to K^0_S h^+ h'^-) \times \mathcal{B}(K^0_S \to \pi^+\pi^-) \times f_{d,s} \times \epsilon^{\text{MC}}$$

where $\sigma(b\bar{b})$ is the $b\bar{b}$ production cross section, $\mathcal{L}$ is the integrated luminosity of the data-taking period for which we are optimising the selection, $f_{d,s}$ is the hadronisation fraction of the $B^0_{(s)}$ meson, and ϵ^{MC} is the efficiency of the selection that we apply before the BDT cuts, that we evaluate on simulated events. The number of combinatorial background events B is measured from

the data sample. We fit first the region above 5550 MeV/c^2. We extrapolate the number of combinatorial background events in the signal peak region from a fit to the right-hand side region of the data samples. The number of events arising from crossfeed background events is computed analogously to what is done for the signal events.

In the case of a yet-unobserved decay, we maximise the so called "Punzi figure of merit":

$$\text{FoM} = \frac{\epsilon}{\frac{\alpha}{2} + \sqrt{B}}, \tag{VI.2}$$

where $\alpha = 5$, corresponding to the hoped signal significance, in terms of number of standard deviations, and ϵ is the selection efficiency of the signal as estimated from the simulated data.

Another source of background consists of the Λ_b crossfeeds arising from $\Lambda_b \to phK^0_S$ decays where the proton is misidentified as a kaon or a pion. These events are modelled using MC samples and included in the mass fit.

Partially-reconstructed background are decays for which we missed a daughter particle (e.g. the photon in $B^0 \to K^0_S \pi^+ \pi^- \gamma$). They are modelled using MC samples and included in the mass fit.

Three-body B-meson decays with an intermediate charmed or charmonium particle (e.g $B^0 \to (D^+ \to \pi^+ K^0_S)\pi^-$ or $B^0 \to (J/\psi \to \pi^+\pi^-)K^0_S$) are vetoed as they are well separated from signal events.

Figure VI.2 gives an overview of the fit model. All the components that are included in the fit to the B-meson invariant mass of the $K^0_S h^+ h'^-$ modes are identified in this plot.

The study is focused on data taken during run 1 and run 2 of the LHC. The data is divided into several samples to account for differences in trigger efficiencies and data taking conditions, namely: 2011, 2012a and 2012b, 2015, 2016, 2017 and 2018 samples. The division to two samples in 2012 is due to the fact that during this year's data taking, a significant improvement of the trigger efficiency for long-lived particles was obtained following an update of the software trigger algorithms. We consider separately the candidates in which the daughter pions of the K^0_S left a track in the VELO as well as in the tracking stations (refered to as Long-Long, or LL) and candidates in which these tracks are present in the TT and the T-stations only (Downstream-Downstream, or DD). These candidates are studied in two separate categories as we expect the shapes of the various contributions to differ. We perform a single simultaneous fit to the resulting spectra, in order to measure the yields of the $K^0_S h^+ h'^-$ signal contributions. This fit also allows us to derive sWeights for signal and

background, which are useful for the description of the distributions of signal events over the phase space.

An efficiency study is also performed. It gives the average efficiency of the selection and of various detector effects over the square Dalitz-plane. Correction factors are part of this study: they are needed to take into account discrepancies between the simulated events and data, and are estimated from calibration samples. The total efficiency is then

$$\epsilon^{tot} = \epsilon^{gen}\epsilon^{sel|gen}\epsilon^{PID|(sel|gen)}, \tag{VI.3}$$

where ϵ^{gen} is the generator-level cut efficiency in the Monte Carlo. Generator-level cuts are geometry and physics cuts applied to simulated events after the 4-vector generation and before the detector response is simulated in detail. The $\epsilon^{sel|gen}$ term is the selection efficiency on events that passed the generator level cuts. It includes the trigger, the stripping and the selection efficiency. The stripping is a set of loose cuts that are used to filter the data samples. The term $\epsilon^{PID|(sel|gen)}$ is the PID selection efficiency on the events that passed the rest of the selection.

The efficiency can vary as a function of the position in the Dalitz plane, and the distribution of the $B^0_{(s)} \to K^0_S h^+ h'^-$ signal in the Dalitz plane is not well known a priori. To take this into account, we use the sWeighted distribution of the events over the square Dalitz plane to derive the branching fractions of the $K^0_S h^+ h'^-$ decays. This distribution is derived from

$$\epsilon = \frac{\sum_{e\in\text{data}} sW(e)}{\sum_{e\in\text{data}} \frac{sW(e)}{\epsilon(e)}} \tag{VI.4}$$

where sW(e) is the sWeight of event e and $\epsilon(e)$ is the efficiency associated to it. The overall efficiency of signal events is then computed from the integration over the square-Dalitz plane variables m' and θ':

$$\epsilon^{tot} = \int\int_{\text{sqDP}} f_{B^0_{d,s}\to K^0_S h^+ h'^-}(m',\theta')\,\epsilon_{B^0_{d,s}\to K^0_S h^+ h'^-}(m',\theta')\,dm'd\theta', \tag{VI.5}$$

where m' and θ' are the coordinates of the square Dalitz plane, and $f_{B^0_{d,s}\to K^0_S h^+ h'^-}(m',\theta')$ and $\epsilon_{B^0_{d,s}\to K^0_S h^+ h'^-}(m',\theta')$ are, respectively, the distribution of the signal events and their efficiencies over the square Dalitz plane. The coordinates of the square Dalitz plane are expressed in terms of the Dalitz-plane coordinates as $m' \equiv \arccos\left(2\frac{m_{13}-m_{13}^{min}}{m_{13}^{max}-m_{13}^{min}} - 1\right)$ and $\theta' \equiv \frac{1}{\pi}\theta_{13}$. In these definitions, θ_{13} is the helicity angle of the pair of particles 13, and m_{13}^{max} and m_{13}^{min}

are the kinematics limits of m_{13} such as $m_{13}^{max} = M - m_2$ and $m_{13}^{min} = m_1 + m_3$. From the overall efficiency, we can correct the signal yields that we extract from the fit to data:

$$N^{\rm corr}_{B^0_{d,s}\to K^0_S h^+ h'^-} = \frac{N_{B^0_{d,s}\to K^0_S h^+ h'^-}}{\epsilon^{\rm tot}}. \tag{VI.6}$$

Then

$$B(B^0_{d,s} \to K^0_S h^+ h'^-) = \frac{N^{\rm corr}_{B^0_{d,s}\to K^0_S h^+ h'^-}}{\mathcal{L}\sigma_{p\bar{p}\to b\bar{b}} f_{d,s}} \tag{VI.7}$$

is the branching fraction of the $B^0_{d,s} \to K^0_S h^+ h'^-$ decay. The term $\mathcal{L}$ is the integrated luminosity, $f_{d,s}$ is the fragmentation fraction of the $B^0_{(s)}$ meson and $\sigma_{p\bar{p}\to b\bar{b}}$ is the cross section of $b\bar{b}$ production at LHCb.

We study ratios of branching fractions with respect to the branching fraction of the $B^0 \to K^0_S \pi^+\pi^-$ decay. In that situation, the luminosity and cross-section terms are cancelled out. The uncertainties on f_d/f_s are much smaller than the uncertainties on the individual fragmentation fractions. We want to measure at the end

$$\frac{\mathcal{B}(B^0_{d,s} \to K^0_S h^+ h'^-)}{\mathcal{B}(B^0 \to K^0_S \pi^+\pi^-)} = \frac{N^{\rm corr}_{B^0_{d,s}\to K^0_S h^+ h'^-}}{N^{\rm corr}_{B^0\to K^0_S \pi^+\pi^-}} \frac{f_d}{f_{d,s}}. \tag{VI.8}$$

Finally, we study the systematic uncertainties on these ratios. These include uncertainties from choice of fit model or fixed quantities in the fit to the data, for example, as described in Sec. VI.7.

In the next section, we describe the first step of the analysis, which consists in a loose selection (trigger, stripping) applied to the data events collected by the LHCb detector.

VI.2 Trigger and stripping selections - Online selection

We discuss in this section loose selections applied early in the data-taking process. The aim is to filter out events that are not relevant to LHCb analyses, and save disk space and processing time. Let's detail the trigger and the stripping selections.

VI.2.1 Trigger selection

The trigger selection is processed by three different trigger structures: the L0, the HLT1 and the HLT2. The L0 is a purely hardware trigger. This trigger can fire on detector activity (e.g. calorimeter energy deposits) due to a $K^0_S h^+ h'^-$ signal-like candidate. This kind of trigger activation is classified as TOS for Trigger On Signal. The L0 can also trigger on any other tracks or particles in the event. This is classified as Trigger Independent of Signal or TIS. In that case, the trigger not only fires on hadron lines (HCAL activity), it can also fire on muon, electron or photon lines. This low-level trigger is complemented by two high-level triggers. They consist of the HLT1 and the HLT2. The HLTs are software triggers that perform a basic reconstruction of the event. HLT1 filters events that passed the L0 by selecting events with an high transverse momentum, with a good fit quality and that are well separated from the primary vertex. Next comes the HLT2. It conducts a full event reconstruction in order to perform a more detailed selection. This additional filtering is done through inclusive topological trigger lines [83]. These lines are meant to trigger on partially or fully reconstructed decays that contain at least two charged daughters originating at a secondary vertex. At first a list of 2-body proto-candidates is produced. These are made from 2 particles for which the primary vertex with the smallest impact parameter is the same. These particles should also have a distance of closest approach smaller than 2mm. It is required that their vertex should be downstream the primary vertex we mentioned above. Then, n-body topological lines are build by further filtering the two-body proto-candidates. The candidates are selected thanks to a bonsai boosted decision tree [84]. The 2-, 3- and 4-body HLT2 lines are relevant for the $K^0_S h^+ h'^-$ analysis. On top of these topological lines, a selection based on simple cuts on variables was used in 2011. Events passing the trigger selection are further filtered during the stripping step.

VI.2.2 Stripping selection

The stripping is a set of lines that are designed to apply loose cuts centrally on data events. They are written for a specific analysis; in our case events are selected according to criteria determining if they are likely to be a $K^0_S h^+ h'^-$ decay. At this stage, the candidates are reconstructed by associating a K^0_S candidate with two oppositely charged tracks. An initial cut requires events to have less than 250 long tracks and at least one primary vertex. This first step ensures that we save CPU time and disk space by discarding events that are not useful. Each selected candidate is then further processed: each track

is at first treated as a pion, they are then fitted again with different mass hypotheses. The K^0_S candidates are formed thanks to the combination of 2 oppositely charged tracks. Candidates compatible with downstream pions are taken from StdNoPIDsDownPions. This contains a list of candidates compatible with downstream pions. For K^0_S belonging to the LL category, the daughters particles are taken from StdLoosePions which contains long tracks compatible with pions. The stripping then proceeds to the reconstruction of the $B^0_{(s)}$ decay.

When reconstructing hadron decays, stripping cuts are applied to the daughter candidate tracks first. The mother candidates are then initially reconstructed by four-momentum addition, which requires limited CPU time. For candidates that pass initial, looser cuts, a vertex fit is performed and a final set of cuts is applied to the mother candidates. Candidates that pass all cuts are refitted using the Decay Tree Fitter package [85]. Constraints can be added at this stage. We use them to improve the B resolution by constraining the B-meson to originate from the best primary vertex. We also constrain the K^0_S to its nominal mass. Crossfeed backgrounds are studied thanks to the change in mass hypothesis performed by the Decay Tree Fitter on simulated signal events.

We discussed here the online selection, performed centrally early in the production chain. In the next section we detail the offline selection.

VI.3 Offline Selection

In sections VI.3.4 and VI.3.5 I describe work done principally by another LHCb student at Clermont-Ferrand, Hossein Afsharnia. While other members of the analysis group and I also contributed through discussions, suggestions, cross-checks, and providing inputs, he was primarily responsible for those parts.

VI.3.1 Preselection

The preselection is performed as a preparation to the actual Multi Variate Analysis and the selection criteria that are based upon it. It consists of topological cuts aimed at reducing the proportion of background, such as cuts on the B-meson pseudo rapidity or cuts on the B-meson transverse momentum. Cuts that would tend to shape the B-meson mass peak and would bring a non-flat efficiency distribution in the Dalitz plane are avoided where possible.

VI.3.2 Multi-Variate analysis

We mitigate the contribution of the combinatorial background and the crossfeed background thanks to multivariate selectors. These are algorithms that take several discriminating variables as inputs and combine them into a single output variable. Applying a suitable cut on the output variable reduces the proportion of background events in the sample considered. We implemented two selectors of this kind: the first is based on topological variables (and in general variables that are not correlated with the B-meson kinematics) and is meant to reduce the combinatorial background contribution, and the second is based on particle identification quantities. This is used to reduce the contribution of crossfeed backgrounds.

The multivariate analysis we used is based on boosted decision trees.

Boosted Decision Tree

Boosted Decision Trees are a machine learning tool. They are used to discriminate between signal- and background-like events in data samples. These algorithms are supervised (see explanation below) and we use them to classify events as background or signal. We feed the tool with a set of variables for which discriminating power has been found. Based on this set of variables, the decision tree provides a weight for each event to be signal- or background-like. "Supervised algorithm" means that we train the tree on a well-known data set (proxy) before applying it to unknown data. We already know which events in the proxy are (simulated) signal events and which ones are background events. We use this information to supervise the learning of the algorithm. The pros of these classifiers is that it is quite easy to understand what they are doing as well as visualising the steps that the algorithm takes to separate events. The discriminating variables should preferably have strong separation power, but using extra variables with a low power should not reduce the performance. On the cons side, decision trees are prone to over-fitting and one should be careful when setting the parameters of the algorithm. The algorithm of boosted decision trees, used in the current analysis, consists of many weak learners that are trained sequentially on different subsets of the training set. At each iteration, a weight is attributed to each subset. Sets that were wrongly classified get an increasing weight at each step. Thus, the weak learners are forced to focus on samples that are harder to predict. Not only are we using boosted decision trees, we are in fact using gradient-boosted decision trees. Gradient boosting implies that rather than weighting samples that are harder to predict, we boost the decision trees according to the gradient of the loss function. In

the case of a classifier algorithm, the loss function is describing how good we are at identifying signal events.

When implementing this kind of selection, the first step is to train the BDT (Boosted Decision Tree). We separate our signal and background events into training and testing samples. With the training sample, the tool is able to build the tree through which a weight will be applied to events to associate them to background or signal categories. In order to make sure that the BDT we trained is performing well, we also apply it to test samples. This allows us to estimate its performance and also make sure we did not over-fit the data. We evaluate the performance using the ROC curve, which shows the background rejection against the signal efficiency. An ideal machine learning tool will have an area under the ROC curve close to one; a poorly performing one will tend to have a ROC curve area around 0.5 (the limiting case where we assign randomly one of the 2 classes to the events). To ensure that we did not over-train the tree, we should plot the distributions of the weights attributed by the BDT for background and signal events, doing so for the training and testing samples. If the distributions are close when comparing the 2 samples, as measured with a Kolmogorov-Smirnov test for example, then we can assume that the BTD is able to perform well on unseen sets of events.

VI.3.3 Discriminating combinatorial background events

Let's detail the discriminating variables that we use to classify combinatorial background events and signal events. At this stage, we are using, as much as possible, variables that are not correlated with the B-meson mass nor with the kinematics of the Dalitz plane. The signal events on which we trained the BDT come from simulated samples. The background events are taken from the right hand side of the data samples.

The set of discriminating variables is based on what was used in the previous analysis (see Ref. [10]) and was further studied during Emilie Bertholet's thesis [86]. Variables that present a clear discriminating power include, for example, the χ^2 or quality of the fit that reconstructs the impact parameter of the B-meson with respect to the primary vertex. Variables such as the B-meson vertex isolation or fit quality of the B-meson vertex are useful here. The impact parameters of the daughters of the B meson are correlated with the B-meson kinematics. Their sum does not have this property so it is used as a discriminating variable. The list of variables used differs between LL and DD categories, e.g. the flight distance of the K^0_S is not used in the selector

VI.3 Offline Selection

Topological MVA input variables		
Variable	Descritpion	Sample
$p_T(B)$	B transverse momentum	DD and LL
$\eta(B)$	B pseudo-rapidity	DD and LL
$\chi^2_{IP}(B)$	χ^2 significance of the impact parameter of the B	DD and LL
$\chi^2_{FD}(B)$	χ^2 significance of the flight distance of the B	DD and LL
DIRA(B)	cosine of the angle between the B displacement vector and the B momentum vector	DD and LL
$\chi^2_{vtx}(B)$	Vertex fit quality of the B	DD and LL
$\chi^2_{ISOvtx}(B)$	B-meson vertex isolation	DD and LL
$p_T^{asym}(B)$	B p_T asymmetry for a cone of radius 1.5 rad around the B-candidate in the $\eta-\phi$ plane	DD and LL
$\chi^2_{IP}(h^+)+\chi^2_{IP}(h^-)$	sum of the χ^2_{IP} of the B charged hadron daughters	DD
$\chi^2_{FD}(K^0_S)$	χ^2 of the flight distance of the K^0_S	LL
$\chi^2_{IP}(h^+)+\chi^2_{IP}(h^-)+\chi^2_{IP}(K^0_S)$	sum of the χ^2_{IP} of the B daughters	LL
$p_T^{asym}(K^0_S)$	K^0_S p_T asymmetry for a cone of radius 1.5 rad around the K^0_S-candidate in the $\eta-\phi$ plane	DD and LL
$p^{asym}(B)$	B p asymmetry for a cone of radius 1.5 rad around the B-candidate in the $\eta-\phi$ plane	DD and LL
$p^{asym}(K^0_S)$	K^0_S p asymmetry for a cone of radius 1.5 rad around the K^0_S-candidate in the $\eta-\phi$ plane	DD and LL
$\Delta\eta^{asym}(B)$	cone $\Delta\eta$ asymmetry for the B candidate	DD and LL
$\Delta\eta^{asym}(K^0_S)$	cone $\Delta\eta$ asymmetry for the K^0_S candidate	DD and LL
$\Delta\phi^{asym}(B)$	cone $\Delta\phi$ asymmetry for the B candidate	DD and LL
$\Delta\phi^{asym}(K^0_S)$	cone $\Delta\phi$ asymmetry for the K^0_S candidate	DD and LL

Table I: This tables contains the discriminating variables that we used to train the topological BDT. We list in this table the name of the variables, a brief definition and we mention also to which sample these variables are used as discriminating variables.

of the DD category. The impact parameter of the K^0_S is not included when computing the sum of impact parameters of B-meson daughters for DD events. The discriminating variables included in the multivariate selector are listed in Tab. I. The cone variables are defined as the asymmetry between the variable associated to the desired track and the value of the sum over all the tracks that are contained in a cone around the particle in question.

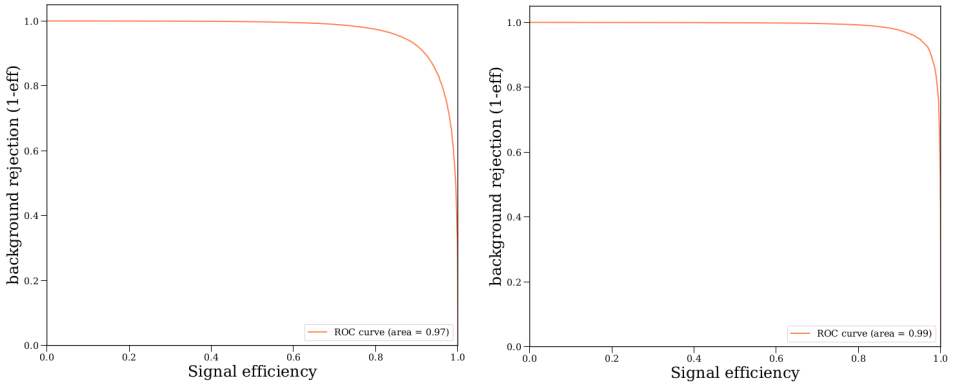

Figure VI.3: ROC curves for the topological multivariate analysis - 2018 DD (LL) on the left (right). We use the area under the ROC curve to estimate how well the algorithm is performing. With an area under the ROC curve equal to or above 0.97 in both cases, we can assume that the classifying tool is performing very well.

We present the performance of the selection developed to reduce combinatorial background events. Two quantities are of interest here: the 'classifying power' and the degree of over-fitting. The ROC curve, associated with the first quantity, tells us how good is the algorithm at separating background and signal events. We show in Fig. VI.3 the ROC curves for the $B^0 \to K^0_S \pi^+ \pi^-$ decays in the case of the 2018 data taking period. The left plot is the plot where the K^0_S is DD, the right plot is given for the LL category.

In general, candidates with a Long-Long K^0_S tend to lead to a better performing selection tool. The performance seems to be equivalent for all data taking period. Table II gives the area under the ROC curve for all data-taking periods and K^0_S reconstruction category. It is not enough to check the ability of the classifier to separate background and signal events. We have to make sure that the good performance we observed is not associated with strong over-fitting. As we already stated, we verify this by separating our samples into a training sample (on which we train the selector) and a testing sample that hasn't been seen by the selector during the training. We can assume that the boosted decision trees are working well on unseen data - that they are not over-fitting - if we observe similar performance on the training and on the testing samples. We study also the background and signal MVA weight distributions for both sets. If they are similar enough, over-fitting should not be an issue. We ran this study for both K^0_S categories and also for all data taking periods. The parameters of the multivariate analysis were chosen to reduce the risk of over-fitting. These parameters are used to control the learning process.

Topological MVA area under the ROC curve		
Data-taking period	DD sample result	LL sample result
2011	0.97	0.98
2012a	0.95	0.98
2012b	0.98	0.97
2015	0.97	0.98
2016	0.97	0.99
2017	0.97	0.99
2018	0.97	0.99

Table II: This tables contains the area under the ROC curve of the topological BDT for each data-taking period. It holds this information for both DD and LL category.

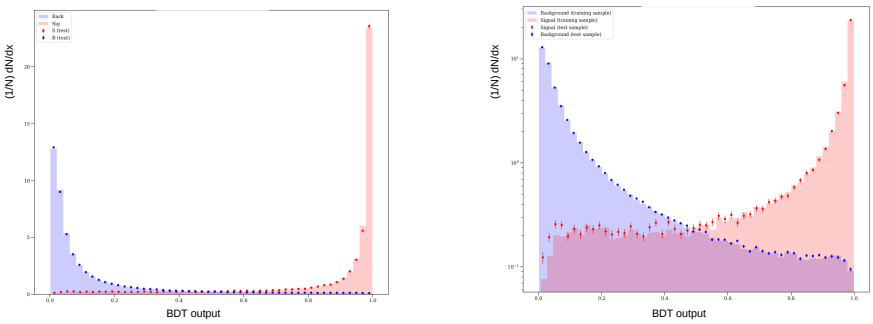

Figure VI.4: Distribution in linear/logarithmic sale (left/right) of the MVA output variable for the signal and background events of the 2018 DD samples. We plot the distribution of train and test samples in order to look for over-fitting. A Kolmogorov-Smirnov test and the comparison of the accuracy on the test and train samples confirms that we should not be worried about over-fitting.

They are for example the number of estimators or the maximum depth of the trees of the classifier. Figure VI.4 shows the over-training test on signal and background events of the 2018 DD samples. The Kolmogorov-Smirnov test gives a p-value of around 90% in the case of the background components, the p-value for the signal is at a level of a few percents. We see on Fig. VI.4 that the training and test samples have similar distribution in the region above 0.5, they tend to diverge for lower value. We deduce that a mild over-training is happening but the region where we apply our selection cuts is not concerned by this issue.

We discussed how to reduce the contribution of one of the dominant, combinatorial background. We now turn to how we deal with the crossfeed backgrounds. Since these backgrounds tend to live under the signal peaks, we need use a second selector to reduce their contamination.

VI.3.4 Discriminating crossfeed background

In the previous analysis [10], the crossfeed background contributions were reduced using cuts on particle identification variables known as ProbNNs. ProbNNs are the output of a Neural Network. Observables measured in the LHCb detector that contribute to particle identification (such as the ring size in the RICH detectors) are combined through the use of the neural network. As an output, this machine learning tool gives a variable that tell us how likely a particle is to be a pion for example. They are transformed so that they are contained in [0,1]. Hence, a ProbNN_K close to one tells us that the considered particle is most likely a kaon.

In the current analysis, we developed a new selection for the crossfeeds. Instead of simply cutting on the ProbNN quantities, we feed them to a second boosted decision tree. This latter is trained on simulated signal and crossfeed events. We use the ProbNN associated with the kaon, pion and proton hypothesis as discriminating variables. The classifier was trained to separate crossfeeds and signal events, and shows good performance as illustrated in Fig. VI.5. We also checked that over-fitting was at a reasonably low level. This is shown in Fig. VI.6

We have now in our hands boosted decision trees that perform well at discriminating background events, of various sources, from signal events. We next wish to optimise their performance. The outputs of both decision trees are correlated, so we perform a 2-dimensional optimisation.

VI.3.5 BDT optimisation

Having trained the two BDT selectors, then we want to maximise a function related to the significance of our signal. We do this in two different ways depending on whether the decay has already been observed, as discussed in Sec. VI.1 (we use Eq. VI.1 for previously observed decays, and Eq. VI.2 with $\alpha = 5$ for $B^0_s \to K^0_S K^+ K^-$). As we are running two separated but correlated multivariate analyses, the optimal cut points on the MVA's output variable are taken from a 2-dimensional optimisation, outlined below.

For each decay mode in a subsample, we define a 2-dimensionnal grid of cut values, evaluating the expected signal and background yields in a region

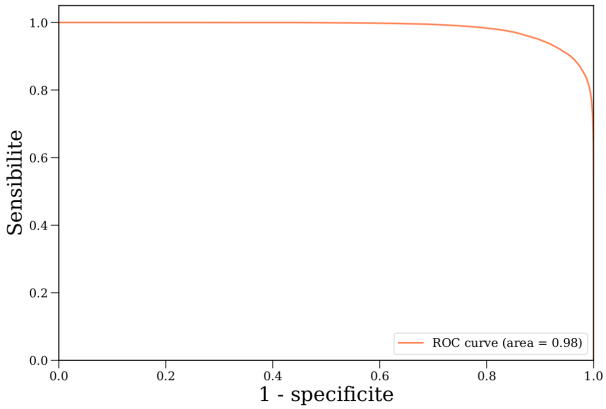

Figure VI.5: ROC curves for the multivariate analysis on the PID - 2018. We use the area under the ROC curve to estimate how well the algorithm is performing. With an area under the ROC curve equal to 0.98, we can assume that the classifying tool is performing very well.

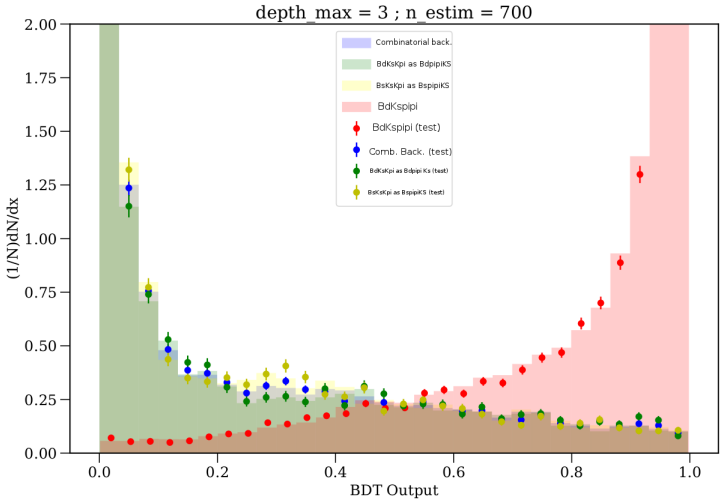

Figure VI.6: Distribution in linear scale of the MVA output variable for the signal and background events of the 2018 DD samples. We plot the distribution of training and test samples in order to look for over-fitting. The red component is the $B^0 \rightarrow K^0_S \pi^+ \pi^-$ signal, the blue component is the combinatorial background, the yellow component is the ($B^0 \rightarrow K^0_S K^+ \pi^-$ as $B^0 \rightarrow K^0_S \pi^+ \pi^-$) crossfeed background and the green component is the ($B^0_s \rightarrow K^0_S K^+ \pi^-$ as $B^0_s \rightarrow K^0_S \pi^+ \pi^-$) crossfeed.

around the signal peak at each grid point. We estimate the signal yield and the combinatorial background events from a fit to the data. Crossfeed yields are estimated from the expected yield of the origin mode and the efficiency with which simulated events of that decay pass the selection of the destination mode (e.g. the efficiency with which $B^0_s \to K^0_S K^+ K^-$ passes the $B^0 \to K^0_S \pi^+ \pi^-$ selectors). We optimise selections for both the B_d and the B_s signals separately. When we optimise on the B_d signal component for example, the B_s signal events are counted as background events, and vice-versa. We loop over the possible BDT output values of the topological and the PID selections together, until the signal significance is estimated over the whole 2-dimensional space. The topological and PID BDT output for which we obtained the highest signal significance for that mode are retained.

The optimised selection ensures that the $K^0_S h^+ h'^-$ signal components are studied with the highest possible significance, and that the fits to the B-meson mass are performed in the best available conditions. We will discuss the fit strategy in the following section.

VI.4 Fit procedure

We designed a selection that gives to the signal events the highest possible significance over the background events. With this in hand, we are able to perform a B-meson mass fit. This is a key step when measuring branching fractions. First, we set out the fit strategy. We would like to fit simultaneously all $K^0_S h^+ h'^-$ spectra. Here, spectrum means mass distribution of all candidates reconstructed as the decay of a B_d or a B_s to one particular $K^0_S h^+ h'^-$ final state. Each spectrum contains two signal species (decay products of B_d and B_s) and three types of background, namely combinatorial, partially reconstructed and crossfeed backround. A background is said to be combinatorial when it arises from the random association of pairs of charged hadron with a K^0_S (real or fake). A crossfeed is a background that appears when daughter particles are misidentified. We limited the crossfeed contribution to the case of a single mis-identification as this scenario is largely dominant over double mis-identification. Two type of crossfeeds are considered. We take into account crossfeeds pollution from other $K^0_S h^+ h'^-$ decays, for example a $B^0 \to K^0_S K^+ K^-$ reconstruced as a $B^0 \to K^0_S K^+ \pi^-$. We also include crossfeeds from $\Lambda_b \to p h K^0_S$ where the proton is mis-identified as a meson. The third class of background, from partially reconstructed decays, populates the left-hand side of each spectrum. For example, $B^0 \to K^0_S \pi^+ \pi^- \gamma$ events for which we missed the photon will appear to the left of the main B^0 peack. Simulated samples are used in most cases to

determine the shapes of the structures populating the mass spectra. The shape of the combinatorial background is the only shape determined purely from the data, we model it by a polynomial. In the case of the other contributions, the shape is taken from a fit to the MC samples but some of their parameters may be modified when fitting the data.

The fit procedure will rely on a software package named V0hhFitter. It is a tool developed by the analysis group designed around the Roofit fitter developed to perform complex simultaneous fits.

VI.4.1 Maximum Likelihood Estimator

We want to extract from the data collected by LHCb quantities relevant to the $K^0_S h^+ h'^-$ analysis such as the yields of $K^0_S h^+ h'^-$ decays. To do so, we first decide on a model that should describe the data. The parameters of this model are to be fitted to describe the (simulated) data distribution, using a maximum likelihood estimator to fit the parameters of the model to the event distribution. Maximum likelihood estimators are unbiased and efficient with large sets of data. For a given model, the likelihood is

$$L(\theta) = \prod_{i=1}^{N} f(x_i, \theta), \tag{VI.9}$$

where x_i are independent measurements of an observable x and f is the chosen model, expressed as a probability density function and depending on one or more parameters θ. As discussed above, the data sample should be described by several background and signal contributions. Thus, their yield is also a parameter that should be determined by the estimator. In most cases, the number of events N_i of a given contribution follows a Poisson distribution,

$$f(N_i) = \frac{N_{i,0}^{N_i}}{N_i!} e^{-N_i,0}, \tag{VI.10}$$

around a mean yield $N_{i,0}$. Equation VI.9 is then transformed to

$$L(\theta) = \frac{e^{-N}}{N_0!} \prod_{i=1}^{N_0} f(x_i, \theta; N_i), \tag{VI.11}$$

which is usually called the extended maximum likelihood. We define $N_0 = \sum_i N_{i,0}$ and $N = \sum_i N_i$.

Some parameters of the model we use to describe the data distribution might be over-sensitive to small statistical fluctuations and thereby harm the

fit stability. Fortunately, some of these parameters can be constrained if we happen to have information about their behaviour. We can then constrain parameters based on this prior knowledge ; gaussian constraints are useful tools here. They enable us to constrain a parameter at its expected value and allow it to vary within the uncertainties on this value. Independently of the shape that the constraints we apply may take, they are implemented as penalties to the likelihood function.

Now that we have described the tools we are using, we next discuss in more detail the fit procedure for each species in the final data fit.

VI.4.2 Model for signal components

The signal components consist of B_d and B_s meson decays to $K^0_S h^+ h'^-$. We take their shape from simulated samples, since the available data is too limited to extract all of the features (particularly the tails of the distribution). The signal species are described by double crystal ball function [87]. These are simply a sum of two crystal ball functions that share the same width and mean. Crystal ball functions are Gaussian distributions with a power-law tail [87]:

$$f(t; n, \alpha, \sigma) = N \begin{cases} e^{\frac{-t^2}{2\sigma^2}} & \text{if } t/\sigma > -\alpha \\ (\frac{n}{|\alpha|})^n (\frac{n-\alpha^2}{|\alpha|} - \frac{t}{\sigma})^{-n} e^{\frac{-\alpha^2}{2}} & \text{if } t/\sigma \leq -\alpha, \end{cases} \tag{VI.12}$$

where N is a normalisation factor and σ is the width of the Gaussian distribution. We define $t = m - \mu$ as the difference between the reconstructed mass and the mean μ of the Gaussian distribution. The parameters α describes the position of the tail with respect to the Gaussian distribution. The parameter n controls the power-law tail. The double crystal ball allows us to describe radiative effects resulting in photon emission by the final state particles: the left tail takes this into account. Detector resolution effects dominate the right-hand tail. We perform a simultaneous fit to simulated samples of all categories we consider. An example of a fit to Monte Carlo signal events is shown in Fig.VI.7, for $B^0 \to K^0_S \pi^+ \pi^-$ using long tracks for the K^0_S. The plot shows events simulated under 2018 conditions. A few assumptions are necessary to ensure the stability of the fit. The left tail parameters are constrained to be the same for all data-taking periods and K^0_S reconstruction category (DD and LL) but can vary between final states whereas the right tail has a common shape between all the categories. In the fit to the data, the tail parameters are fixed to the values found in the fit to simulation. The peak position μ is free to vary between data-taking periods but is common between K^0_S reconstruction categories and decay types. The width σ of the $B^0 \to K^0_S \pi^+ \pi^-$ decays is free

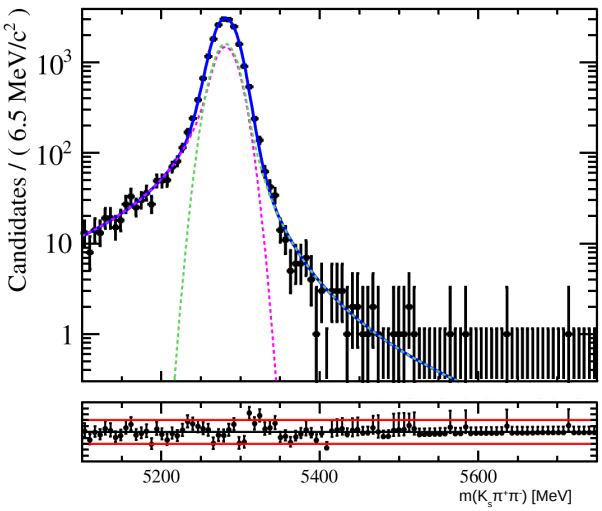

Figure VI.7: Example of fit to the simulated data signal. Signal distribution are modelled by a double crystal ball. We show here the 2018 sample, $B^0 \to K^0_S\pi^+\pi^-$ where the K^0_S is Long-Long. The x axis is the reconstructed B-meson mass, expressed in MeV. The green and magenta distributions are respectively the right- and left-hand side tail crystal ball.

to vary between data-taking periods. Multiplicative scale factors for the width of the other categories are taken from the simulated sample fit results and then fixed in the data fit. We extracted scale factors from the simulated data for each data-taking period for each of the following width: the $K^0_S K^+K^-$ width, $K^0_S K^+\pi^-$ width, the LL/DD ratio and the B^0/B^0_s ratio.

VI.4.3 Model for crossfeeds components

A crucial component of the analysis are the crossfeed (CF) contributions. These appears when one of the hadron of the decay is misidentified. Since they tend to lie under the signal contributions, having a good control of the crossfeed background is a requirement. We consider only dominant crossfeeds. For example, misidentified $K^0_S\pi^+\pi^-$ decaying from a B^0_s are suppressed against the B^0 decays. Doubly misidentified crossfeeds have been studied and found to be negligible compared to single misidentified decays. For example, in fitting the $K^0_S\pi^+\pi^-$ and the $K^0_S K^+K^-$ spectra we take only into account crossfeed contributions from B^0_s and B^0 decays to $K^0_S K^+\pi^-$. Likewise, the $K^0_S K^+\pi^-$ spectrum is polluted by B^0 meson decays to $K^0_S\pi^+\pi^-$ and $K^0_S K^+K^-$. The complete list of crossfeed backgrounds we considered is the following:

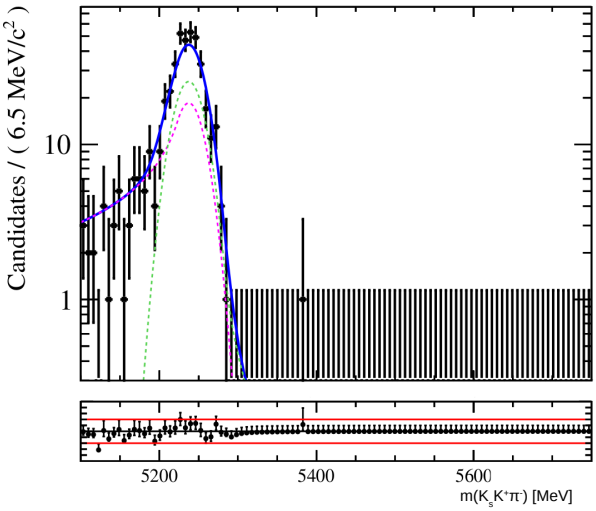

Figure VI.8: Example of a fit to a crossfeed component in simulated data. The crossfeed distribution is modelled by a double crystal ball. We show here $B^0 \to K^0_S K^+ K^-$ reconstructed as $K^0_S K^+ \pi^-$ where the K^0_S are downstream, for data simulated in 2018 conditions. The x axis is the reconstructed B-meson mass, expressed in MeV

- $B^0 \to K^0_S \pi^+ \pi^-$ reconstructed as $B^0 \to K^0_S K^+ \pi^-$
- $B^0 \to K^0_S K^+ K^-$ reconstructed as $B^0 \to K^0_S K^+ \pi^-$
- $B^0 \to K^0_S K^+ \pi^-$ reconstructed as $B^0 \to K^0_S \pi^+ \pi^-$
- $B^0_s \to K^0_S K^+ \pi^-$ reconstructed as $B^0_s \to K^0_S \pi^+ \pi^-$
- $B^0 \to K^0_S K^+ \pi^-$ reconstructed as $B^0 \to K^0_S K^+ K^-$
- $B^0_s \to K^0_S K^+ \pi^-$ reconstructed as $B^0_s \to K^0_S K^+ K^-$

The shape of crossfeed backgrounds are described by double crystal ball functions. To obtain a converging fit to the Monte-Carlo samples, we fit each decay type individually. In each of these fits, all the shape parameters are common between data-taking periods and K^0_S reconstruction categories. An example of a fit to Monte Carlo signal events is shown in Fig.VI.8, for $B^0 \to K^0_S K^+ K^-$ reconstructed as $K^0_S K^+ \pi^-$ using downstream K^0_S. The plot shows events simulated under 2018 conditions. In the fit to the data, the shapes are taken from the fit to the simulated samples and all the shape parameters are then fixed. The yields of the crossfeeds are not free to vary, instead we constrain their yield based on the yield of the signal from which they are originating.

Since the selections of different final states are quite similar (differing mainly in the BDT cuts), we can estimate the yield of a misidentified crossfeed N_{CF} as the correctly identified (source) yield N_s multiplied by the ratio of selection efficiencies:

$$\frac{N_{CF}}{N_S} = \frac{\epsilon_{CF}}{\epsilon_S} \tag{VI.13}$$

These efficiencies are estimated on the simulated samples. We apply Gaussian constraints to these yields, with the central value determined from the ratio above. The width is taken from propagation of the uncertainties on the efficiency ratio and statistical uncertainties on the yields.

VI.4.4 Model for partially reconstructed background components

Partially reconstructed backgrounds are contributions resulting from the fact that we miss a daughter particle in a 4- (or more) body decay, e.g. $B^0 \to K^0_S\pi^+\pi^-\gamma$. The partially reconstructed event will be interpreted as a B-meson charmless 3-body decay. It will appear in the left-hand side of the spectrum. Numerous decays can contribute to this background type. From the previous analysis [10], we know that 4 categories are enough to describe these partially reconstructed events well. Two of these categories appear in all the spectrum, independently of the decay type:

- Partially reconstructed charmed decays such as $B^+ \to D^0\ (K^0_S\pi^+\pi^-)K^+$
- Partially reconstructed charmless decays such as $B^0 \to K^*\ (K^0_S\pi^0)\rho^0$ $(\pi^+\pi^-)$

The charmed and charmless partially reconstructed background originate from both B_d and B_s decay process. In the case of the $K^0_S\pi^+\pi^-$ spectrum, we have 2 extra categories of partially reconstructed backgroud:

- Partially reconstructed decays where we missed a final state photon such as $B^0 \to K^0_S\pi^+\pi^-\gamma$
- Partially reconstructed decays where we missed a photon emitted by a resonance such as $B^0 \to \eta'(\rho^0\gamma)K^0_S$

We model these contributions as a Gaussian distribution convoluted with an ARGUS function. The shapes are determined with simulation. Their parameters are common between LL and DD K^0_S reconstruction categories.

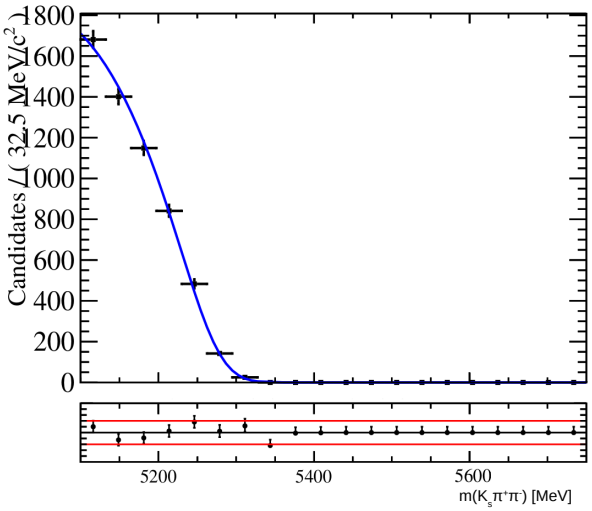

Figure VI.9: Example of a fit to partially reconstructed background in simulated data. Partially reconstructed background distributions are modelled by an ARGUS convoluted with a Gaussian. We show here $B^0 \to K^0_S \pi^+ \pi^- \gamma$ where the photon is not included in the reconstruction and where the K^0_S are downstream, for data simulated in 2018 conditions. The x axis is the reconstructed B-meson mass, expressed in MeV

The shape are then fully fixed in the fit to the data to the parameters found in the fit to the MC. As for the crossfeeds, Gaussian constraints are used to control the partially reconstructed background yields. We constrain the yields ratio to the ratio of branching fractions and efficiencies

$$\frac{N_B}{N_S} = \frac{\epsilon_B}{\epsilon_S} \frac{BR_B}{BR_S}. \tag{VI.14}$$

Figure VI.9 shows the fit to the 2018 DD simulated samples.

VI.4.5 Model for Λ_b crossfeed backgrounds components

Decays of a $\Lambda_b \to phK^0_S$ may contribute to the $K^0_S h^+ h'^-$ spectra. When the proton is misidentified as a kaon or a pion, these events can contribute as crossfeeds. We observed that the shape of these contributions were strongly sculpted by the BDT based on particle identification quantities. Thus, the Λ_b crossfeed backgrounds are modelled with KEYS pdf [88].

Once again, the yields are Gaussian-constrained to the ratio of branching fraction and efficiencies:

$$\frac{N_{LbCF}}{N_S} = \frac{\epsilon_B}{\epsilon_S} \frac{BR_B}{BR_S} \tag{VI.15}$$

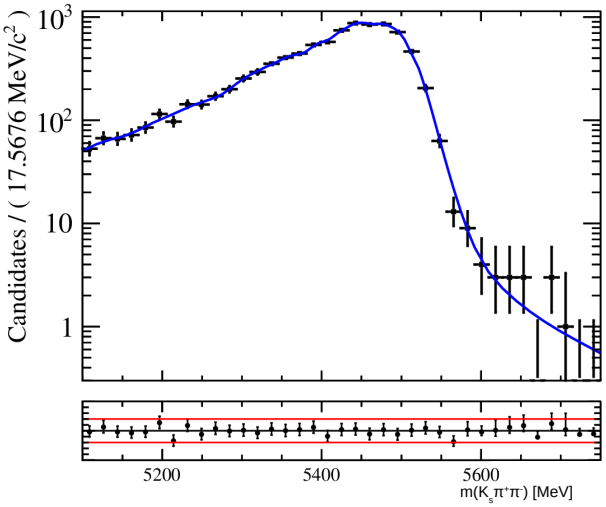

Figure VI.10: Example of fit to the simulated data Λ_b crossfeed. Λ_b crossfeed are modelled by KEYS pdf. We show here $\Lambda_b \to phK^0_S$ reconstructed as $K^0_S\pi^+\pi^-$ where the K^0_S are downstream, for data simulated in 2018 conditions. The x axis is the reconstructed B-meson mass, expressed in MeV

Figure VI.10 shows a fit to $\Lambda_b \to phK^0_S$ as $K^0_S\pi^+\pi^-$ crossfeed in 2018 MC with downstream K^0_S.

VI.4.6 Fit to the data strategy and results

The shapes, obtained from the fits to the Monte Carlo described above, are propagated to the fit to the data. The shape of the combinatorial background is taken to by a polynomial and its slope is measured in the fit to the data. This fit is a complex procedure. Due to the large number of floating parameters and subsamples (spectra) to fit, the fit to the data is performed in several steps. First, the signal shape free parameters are fitted. In the fit to the data, the central value μ of the signal double crystal balls is common between LL and DD, and between the final states but is free to vary between the data-taking periods. The width σ of the $B^0 \to K^0_S\pi^+\pi^-$ decays is free to vary in the fit to the data between data-taking periods in the case of the DD category. We measured in the fit to simulated data ratios of the width of the signal crystal balls relative to the width of the $B^0 \to K^0_S\pi^+\pi^-$ DD decays. The other widths are fixed in the fit to the data with these ratios. In this step, we also fit the signal yield and the yields of the crossfeeds. Once we have determined these parameters, we fit the Gaussian constraint on the partially reconstructed

background, one decay type at a time. First, we fit the branching fraction ratios. This term is common to all the spectra for a given decay type, i.e. the ratio of branching fractions is the same independently of the data-taking period or the K^0_S category. For many partially reconstructed backgrounds, not only is the branching fraction poorly known, but even the efficiency is uncertain (since it depends on an unkown phase space distribution), and can vary between subsamples with different selections. We therefore refit each subsamples individually with floating efficiency ratios. Finally, the yields of the partially reconstructed background are fixed thanks to the value of the ratios measured in the previous steps and we fit the data one last time. The fit to the data results in the case of the 2018 DD (LL) data are shown on Fig. VI.11 (Fig. B.14). The fit to the other data-taking periods can be find in appendix B.1.

From this fit result, we are able to extract not only signal yields but also the full set of shapes and normalisations, and hence we can compute per-event weights (sWeights [89]).

VI.5 The ${}_s\mathcal{P}lot$ method

The events populating each and every $K^0_S h^+ h'^-$ spectrum are mixtures of signal and background. The phase-space distribution of signal events is not known a priori. We need to access this information in order to average the selection efficiency over the phase space. An ${}_s\mathcal{P}lot$ [89] procedure has been implemented in the case of the $K^0_S h^+ h'^-$ analysis. The ${}_s\mathcal{P}lot$ is a tool that allows to reconstruct the distribution of signal and background events for a control variable x. It does not require any prior knowledge of the said control variables. The ${}_s\mathcal{P}lot$ method relies on a discriminating variable y. If the distributions of the discriminating variable (here, the invariant mass of a B meson) is known for all the contributions in a sample, we can deduce the distribution of each of these species in the control variable on a statistical level. This is only possible in the case where the control variable and the discriminating variable are not correlated. This method allows to attribute an sWeight to each event e of a species n. This weight is defined as:

$$sP_n(y_e) = \frac{\sum_{j=1}^{N_s} V_{nj} f_j(y_e)}{\sum_{k=1}^{N_s} N_k f_k(y_e)}. \tag{VI.16}$$

In this equation, N_s is the number of species. In our analysis, N_k would be the yield of a given contribution and f_k would be its normalised PDF. The term V_{nj} is then the covariance of the yields of the contributions n and j.

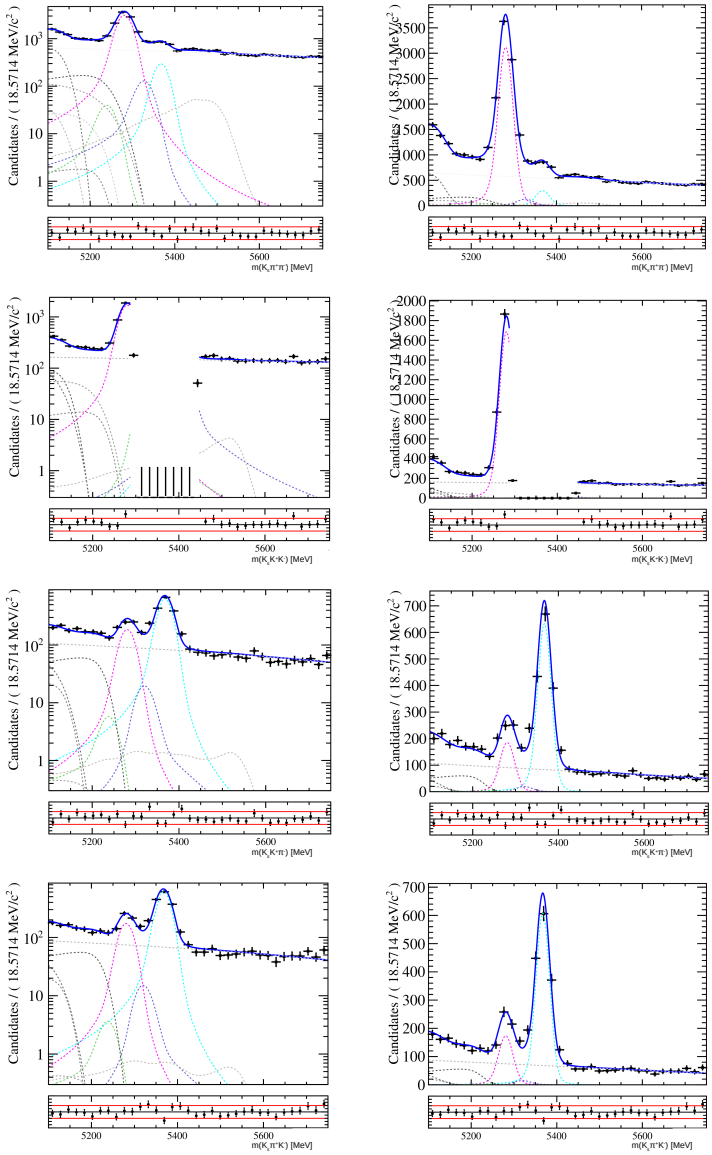

Figure VI.11: Result of the simultaneous fit to the data. We show here the results on 2018, DD. The selection has been optimised on the B^0 signal. From top to bottom, $K^0_S\pi^+\pi^-$, $K^0_S K^+K^-$, $K^0_S K^+\pi^-$ and $K^0_S\pi^+K^-$ are shown. The left-hand-side plots have a logarithmic scale, and the plots on the right show the same data on a linear scale. The magenta dashed line is the B^0 signal contribution. The B^0_s signal peak is in cyan. The crossfeed backgrounds are the blue and green dashe lines. The grey dashed line peaking above 5400 MeV is the Λ_b crossfeed background. To the left of the plot, the grey dashed lines illustrate the partially reconstructed background contributions and the combinatorial background is the grey straight line. In the $K^0_S K^+K^-$ spectra, the region around the B^0_s signal (5320-5450 MeV) is blinded.

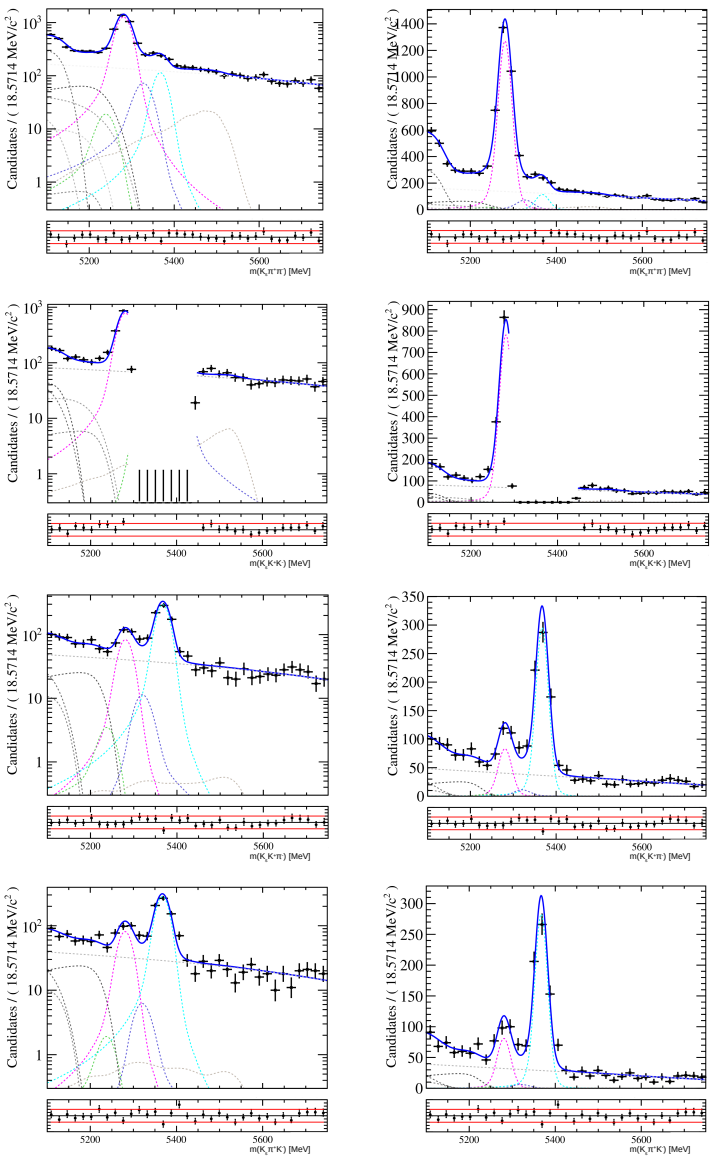

Figure VI.12: Result of the simultaneous fit to the data. We show here the results on 2018, LL. The selection has been optimised on the B^0 signal. From top to bottom, $K^0_S\pi^+\pi^-$, $K^0_S K^+K^-$, $K^0_S K^+\pi^-$ and $K^0_S\pi^+K^-$ are shown. The left-hand-side plots have a logarithmic scale, and the plots on the right show the same data on a linear scale. The magenta dashed line is the B^0 signal contribution. The B^0_s signal peak is in cyan. The crossfeed backgrounds are the blue and green dashe lines. The grey dashed line peaking above 5400 MeV is the Λ_b crossfeed background. To the left of the plot, the grey dashed lines illustrate the partially reconstructed background contributions and the combinatorial background is the grey straight line. In the $K^0_S K^+K^-$ spectra, the region around the B^0_s signal (5320-5450 MeV) is blinded.

The distribution $\tilde{M}_n(\bar{x})$ of the control variable x is then given by:

$$N_n \tilde{M}_n(\bar{x})\delta x = \sum_{e \in \delta x} sP_n(y_e), \tag{VI.17}$$

where the bins of the binned distribution of the control variable have a width of δ_x and each bin is centred on $\bar{x}$.

We now have per-events weights, determined based on their distribution in the B-meson mass spectrum. From them, we consider the background-subtracted signal distributions in the Dalitz planes. Next, we will combine this information with the efficiency variation within the Dalitz plot to improve our description of the average efficiency across the phase space.

VI.6 Efficiencies

Performing the branching fraction measurement requires to correct the signal yield we measure from the fit to the data to account for the efficiency of our selection. The first process we considered is the acceptance of the detector. The efficiencies of the various selection process discussed in Sec. VI.3 should also be studied. The simulated data does not describe the data perfectly. In particular, the Monte Carlo samples does not reproduce perfectly the number of track, differences in the impulsion distributions or miscalibration of the calorimeter for example. These discrepancies have an impact on the description of the efficiencies of the various selection process. We should then correct the Monte Carlo distributions of the relevant quantities to match the data distributions of these quantities and propagate these corrections to the efficiency determinations. In the end, all the efficiencies will be combined to determine a total efficiency over the phase space of the $B^0_{(s)} \to K^0_S h^+ h'^-$ decays.

VI.6.1 Efficiency of the LHCb detector acceptance

The LHCb detector (see Chap. IV) does not cover all the directions in which the B mesons can fly. In order to estimate proper branching fractions (BR), we need to evaluate the proportion of decays that happen within LHCb acceptance. To do so, we made sure to generate simulated events without any generator level cuts. We ran private generation of such events as the MC samples that we have are generated with acceptance cuts. With the help of those cuts-free samples we were able to evaluate the efficiency of the acceptance cuts. Some cuts also exists to ensure that the kinematics of the particle are suitable for

the RICH detectors ; we were able to study their efficiency at this stage as well. A few example of the cuts that we evaluate at this stage are listed here:

- $B^0_{(s)}$-meson and K^0_S daughter particles are required to be within the detector acceptance ($1.8 < \eta < 5$ and $0.01 < \theta < 0.4$).
- The charged hadrons are required to be suitable for the RICH detectors, i.e. they should have a momentum in the 3 to 150 GeV.
- The B-meson momentum is required to be larger than 1500 MeV.

VI.6.2 Selection efficiency

To perform a proper study of the various $K^0_S h^+ h'^-$ decays, an optimised selection was applied which ensured the highest significance for our signal over the background. To correctly measure the BF of these decays, we also need to know the efficiency of the selection. The selection consists of the stripping cuts, the pre selection cuts, the MVA cuts and the various vetoes, all of them being detailed in the previous sections. The naive approach to estimate these efficiencies is to compare the distribution of the events before we apply any cuts in the square Dalitz plane to their distribution once all the cuts are applied. This naive approach does not take into account that sadly, the simulated events are not representing well what is observed in the data. A few correction will then be applied on the way to calculate our total efficiency.

Tracking efficiency correction

The simulation having imperfections, it is required to take this into account when we estimate the efficiencies. Among what we want to correct, there is the tracking efficiency. The first step is to correct the MC distribution in term of momentum, η and number of long tracks so that they match the data distribution. In order to perform the re-weighting of the simulated samples, we use the re-weighting algorithms from the hep_ml Python package [90]. A Gradient Boosting Re-weighter allows to train a machine learning tool to re-weight the simulated data in order to match real data distributions. This tool takes as an input the variables we would like to correct for. We feed the algorithm with the sWeighted data and the simulated event distributions in η, P_t and P. In both case, the whole selection is applied. The output is a single per event weight. Correlations are handled by the tool it-self and we should not be worried about binning here as the re-weighting is performed event by event. Figure VI.13 shows the P_t distribution of the B meson for

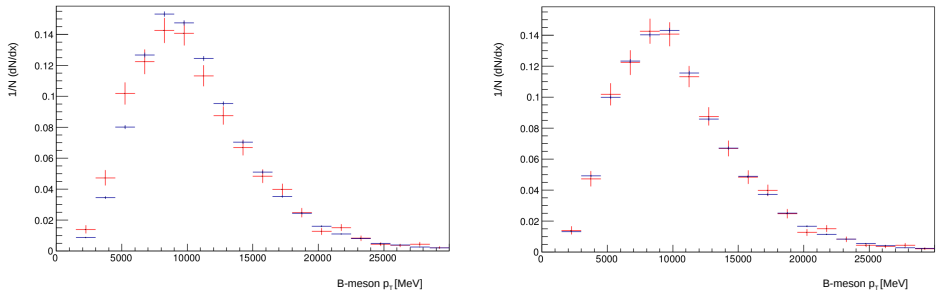

Figure VI.13: We correct the simulated event distributions in term of η, P_t and P as discrepancies are observed between Monte Carlo and real data samples. The left-hand-side plot shows the unweighted MC samples (blue) and sWeighted data (red) for the transverse momentum of the B meson, shown in GeV. On the right hand side, we show the same distributions but the MC is re-weighted to correct for discrepancies in the kinematics distribution of the B meson.

both the MC and data samples, before and after the simulated events have been re-weighted. In both case, the data event have been sWeighted. When we apply a weight to the simulated events to correct for the discrepancies with the real data in the B-meson kinematics, we don't expect any modification in the distribution of the quantities that are not correlated with the B-meson kinematics. Figure VI.14 shows that it is indeed the case: we can without any concern the GB Reweighter. We can then correct for any discrepancies in tracking efficiency between simulated events and the real data events.

The correction for each track is taken from calibration table. These table were produced with $B^+ \to J/\psi K^+$ decays. For each track in the MC samples, a correction factor is attributed. This is done using the value found in the tables, depending on the P and η of each track. We then compute in each square-Dalitz plane bin an average correction factor.

Trigger efficiency correction

The selection efficiency should be corrected to take into account the differences between the L0HadronTOS trigger efficiency observed in the data and in the MC. This correction should be applied to events that passed this requirement but also to those that did not make it. They will be treated separately in the following correction study.

The data efficiency is computed from calibration tables. For each track

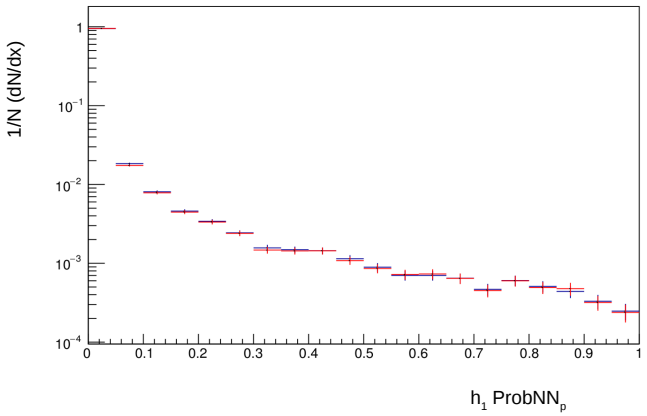

Figure VI.14: We correct the simulated event distributions in term of η, P_t and P as discrepancies are observed between Monte Carlo and real data samples. The plot shows the weighted MC samples (blue) and sWeighted data (red) for the $h1ProbNN_P$, in logarithmic scale. This is performed as a test: we don't expect quantities uncorrelated with the B-meson kinematics to be altered by the correction we apply. ProbNNs are the output of a Neural Network. They are produced by the use of a neural network that combines the observables measured in the LHCb detector that contribute to particle identification.

found in the MC samples, an efficiency is computed. The trigger efficiency for one event is then the probability that we trigger on at least one track.For each track, a set of correction must be applied before we look up in the table the trigger efficiency. The trigger efficiency depends on the transverse energy deposit in the calorimeter. The transverse energy is defined as:

$$E_T = E \sin(\theta) \tag{VI.18}$$

The simulated transverse energy does not take a few effects into consideration: it should be corrected to take into account overlaps between signal track clusters, average occupancy, HCAL mis-calibrations and the fraction of tracks not reaching the HCAL. Once all these corrections are applied, we can compute the data trigger efficiency associated with the corrected transverse energy of each tracks. We can then obtain the distribution of the averaged trigger efficiency for the data in the square Dalitz plane. The efficiency on the MC is computed as the ratio of events passing both TIS and TOS requirement to that of TIS events alone (see Sec. VI.2). By dividing the data and MC

efficiency, one can then obtain the correction that should be applied to the selection efficiency. A similar approach is then applied to events that passed TIS requirements but did not fired TOS.

Total selection efficiency

The trigger efficiency correction that we just discussed above should then be applied to the total selection efficiency. The selection efficiency over the phase space is computed separately for events classified as Trigger On Signal (TOS) and for events classified as Trigger Independent of Signal but not classified as Trigger On Signal (TIS&&!TOS). We apply to these efficiencies the corresponding correction, taking into account the relative amount of events that are respectively TOS or TIS&&!TOS. Eventually, a correction factor is applied to each category to take into account the difference in the proportion of triggered events in the data and in the MC. The total selection efficiency is then:

$$\epsilon^{\text{tot}} = \epsilon^{\text{gen}} \times \epsilon^{\text{sel|gen}} \times \epsilon^{\text{trig|sel}}. \tag{VI.19}$$

With this in hand, we can now compute an averaged total efficiency in the square Dalitz plane for each of our species. This will include all the effects mention in this section. The total efficiency is the product of all the sub efficiencies that we discussed above. It is smoothed with the help of a 2D-cubic spline.

VI.7 Systematic uncertainties study

We now want to evaluate the systematic uncertainties related to the fit process. We consider several sources of systematic uncertainty. The first source arises from fixed parameters in the fit to the data. The first approach we applied was to perform around 100 alternative fits to the data. In these fits, the fixed parameters for which we want to extract a systematic uncertainty are varied according to the correlation matrix of the fit to the simulated data. The distribution of the change in yield between the baseline model and the alternative fit is then fitted with the help of a Gaussian distribution. The systematic uncertainty related to a yield X is then given by:

$$\Delta_X = \sqrt{\left(\frac{\mu}{2}\right)^2 + \sigma^2} \tag{VI.20}$$

where μ is the mean and σ is the width of the Gaussian distribution. We perform such a study for the following parameters:

- The partially reconstructed background shape parameters
- The signal shape tail parameters α_0, n_0, α_1/α_0, n_1/n_0 and the fraction of the two crystal balls

The second source of systematic uncertainties is the choice of models used in the fits to the data. In the previous analysis [10], toy studies were performed to study this source of systematic uncertainties. Unfortunately, the large number of spectra to fit simultaneously and the large number of contributions make such study non-feasible in a reasonable amount of time. Instead, to assess this uncertainty, we perform alternative fits where we change the linehsape model. The systematic uncertainty is then derived from the yield difference between the baseline fit and the alternative fit. For example, we performed such a study for the case of the signal shape. We changed all the signal lineshape (double crystal ball) in favour of single crystal balls and compared the resulting yields. This type of study was also performed for the following fit components:

- The combinatorial background polynomial distribution was instead fitted with an exponential distribution.
- The crossfeed backrounds double crystal balls were replaced by KEYS pdfs.
- The Λ_b crossfeed backgrounds KEYS pdfs were modified and fixed in the fit to the data, using coarser KEYS kernels.

A similar study is conducted in the case of the fixed partially reconstructed background yields. In order to give a brief reminder, we want to mention the fact that the yields of the partially reconstructed backgrounds are fixed to the yield of the dominant signal in each spectrum. We fix the background yields to the signal yields with a ratio of branching fractions and a ratio of efficiencies. In the first steps, we float these ratios within Gaussian constraints. In the last step, we fix the background yield with the fitted ratios' central values.

In the case of the ratio of efficiencies, the uncertainties on these ratios are determined from Monte Carlo. Thus, to derive systematic uncertainties related to the fixed efficiency ratios, we perform, for each ratio, two alternative fits. In a first fit, we fit the data while adding to the value of the ratio one sigma of its uncertainty. In a second fit, we subtract to this ratio one sigma of its uncertainty. The systematic uncertainties in this scenario is then the mean yield difference between the baseline fit yield and each of the alternative fit.

In the case of the ratio of branching fractions, we have a poor knowledge of the branching fraction of the partially reconstructed background and the

uncertainties on them. For each of the ratio of branching fractions, we perform first a negative likelihood scan around the value we obtain from the fit to the data. We reproduce the process described in the case of the ratio of efficiencies once we found alternative value of the ratio of branching fractions for which the delta in two times the negative likelihood is greater than one. The results from the systematic uncertainty studies are given in Table I for the $B^0 \to K^0_S K^+\pi^-$ decay mode. Similar tables for the other decay modes can be found in App. B.2 In each of these tables, we give first the yield measured in the fit to the data. It is followed by the statistical uncertainty. We quote then, in this order, the systematic uncertainties related to the following source:

- Fixed signal shape parameters (Sig. p.)
- Fixed partially reconstructed background shape parameters (P.R. p.)
- Fixed partially reconstructed background efficiency ratios (P.R. eff.)
- Fixed partially reconstructed background branching fraction ratios (P.R. BR)
- Choice in the signal model (Sig. m.)
- Choice in the combinatorial background model (Comb. m.)
- Choice in the Λ_b crossfeed model (Λ_b m.)

We see from these tables that in general, the statistical uncertainty and the systematic uncertainties related to the choice in the signal and combinatorial background models are the dominant uncertainties. Before we move to the results reveal and discussion, we should note that these systematic uncertainties study suffer from one major issue. We were not able to perform toy studies when evaluating the effect of the choice in the model of the fit contributions. The results we present in this section are then prone to statistical fluctuations. This is obvious if we look at Tab. III: the systematic uncertainty related to the choice in the model of the signal contributions is three times larger in the $B^0 \to K^0_S\pi^+\pi^-$ DD category for the 2016 data-taking period compared to the 2017 data-taking period. We note that (where the uncertainty is not tiny) the systematic uncertainties on the final results, i.e. the ratios of branching fractions, are determined from the change to the final result between the baseline and alternative fit. Thus, where effects produce a coherent change across decay modes, we can expect partial cancellation in the ratios.

Systematic uncertainties for each category in the case of the selection optimised on the B^0 signal									
Category	Yield	Stat.	Sig.p.	P.R. p.	P.R. eff.	P.R. BR	Sig.m.	Comb.m.	Λ_b m.
N($B^0 \to K^0_S K^+\pi^-$)(DD)(2011)	52	12	0	1	2	3	5	3	1
N($B^0 \to K^0_S K^+\pi^-$)(DD)(2012a)	36	8	0	0	2	2	3	3	0
N($B^0 \to K^0_S K^+\pi^-$)(DD)(2012b)	90	13	0	1	3	4	11	6	3
N($B^0 \to K^0_S K^+\pi^-$)(DD)(2015)	68	11	0	1	1	3	8	5	4
N($B^0 \to K^0_S K^+\pi^-$)(DD)(2016)	372	30	1	1	4	8	40	30	1
N($B^0 \to K^0_S K^+\pi^-$)(DD)(2017)	421	33	1	1	4	9	48	38	4
N($B^0 \to K^0_S K^+\pi^-$)(DD)(2018)	458	32	1	1	4	9	59	43	15
N($B^0 \to K^0_S K^+\pi^-$)(LL)(2011)	32	8	0	0	2	2	4	5	2
N($B^0 \to K^0_S K^+\pi^-$)(LL)(2012a)	13	4	0	0	1	1	0	1	0
N($B^0 \to K^0_S K^+\pi^-$)(LL)(2012b)	36	9	0	0	2	2	3	2	0
N($B^0 \to K^0_S K^+\pi^-$)(LL)(2015)	33	8	0	0	2	2	5	4	0
N($B^0 \to K^0_S K^+\pi^-$)(LL)(2016)	107	16	0	1	3	5	12	13	0
N($B^0 \to K^0_S K^+\pi^-$)(LL)(2017)	138	18	0	1	3	5	20	13	1
N($B^0 \to K^0_S K^+\pi^-$)(LL)(2018)	193	21	0	1	4	6	25	14	0

Table III: This tables contains the yield, the statistical uncertainties and the systematic uncertainties related to the fit process for the $B^0 \to K^0_S K^+\pi^-$ decays. In general, the statistical uncertainty and the systematic uncertainties related to the choice in the signal and combinatorial background models are the dominant uncertainties.

VI.8 Results

We derive from Eq. VI.6 and Eq. VI.8 the branching fractions of the $K^0_S h^+ h'^-$ decays relative to that of $B^0 \to K^0_S \pi^+\pi^-$. The statistical uncertainties are derived from the uncertainties on the yields, taking into account possible correlations. The systematic uncertainties related to the choice of model of the fit component are taken to be the difference between the branching fraction ratios measured with the nominal fit and these ratios measured with the alternative fits.

Combining all datasets, the ratios of branching fraction relative to that of $B^0 \to K^0_S \pi^+\pi^-$ are measured to be

$$\frac{\mathcal{B}(B^0 \to K^0_S K^+\pi^-)}{\mathcal{B}(B^0 \to K^0_S \pi^+\pi^-)} = 0.150 \pm 0.004(\text{Stat}) \pm 0.018(\text{Syst}),$$
$$\frac{\mathcal{B}(B^0_s \to K^0_S \pi^+\pi^-)}{\mathcal{B}(B^0 \to K^0_S \pi^+\pi^-)} = 0.284 \pm 0.006(\text{Stat}) \pm 0.022(\text{Syst}) \pm 0.009\,(\text{f}_\text{s}/\text{f}_\text{d}),$$
$$\frac{\mathcal{B}(B^0 \to K^0_S K^+K^-)}{\mathcal{B}(B^0 \to K^0_S \pi^+\pi^-)} = 0.647 \pm 0.009(\text{Stat}) \pm 0.010(\text{Syst}),$$
$$\frac{\mathcal{B}(B^0_s \to K^0_S K^+\pi^-)}{\mathcal{B}(B^0 \to K^0_S \pi^+\pi^-)} = 1.924 \pm 0.003(\text{Stat}) \pm 0.010(\text{Syst}) \pm 0.060\,(\text{f}_\text{s}/\text{f}_\text{d}).$$

When relevant, we quote the external uncertainty related to the f_s/f_d ratio.

The results on the $K^0_S K^+ K^-$ samples are not shown here as these are still blinded.

The result on the ratio of branching fraction of $B^0 \to K^0_S K^+ K^-$ relative to that of $B^0 \to K^0_S \pi^+ \pi^-$ are in good agreement with the results from the B-factories. In this case, the averaged ratio was measured to be [91–93]:

$$\frac{\mathcal{B}(B^0 \to K^0_S K^+ \pi^-)}{\mathcal{B}(B^0 \to K^0_S \pi^+ \pi^-)} = 0.134 \pm 0.011,$$

where we quote only the statistical uncertainty. As for $\frac{\mathcal{B}(B^0 \to K^0_S K^+ K^-)}{\mathcal{B}(B^0 \to K^0_S \pi^+ \pi^-)}$, we observe a poor agreement with the results from the B-factories. The averaged measurement from the B-factories is [91, 94, 95]:

$$\frac{\mathcal{B}(B^0 \to K^0_S K^+ K^-)}{\mathcal{B}(B^0 \to K^0_S \pi^+ \pi^-)} = 0.539 \pm 0.025.$$

The result from our analysis is more than 3 σ away from this result.

Comparing the values from the current analysis to the run 1 analysis [10], we observe that most of the results are away from each other by more than 3 σ. Still, reduced statistical uncertainties are obtained compared to the run 1 study, as expected, and the results are limited by systematic uncertainties.

We should note that our results suffer from some limitations. In particular, the efficiencies we have used to measure the ratios of branching fraction do not benefit from the corrections mentioned in Sec. VI.6, nor from the sWeights derived from the fit to the B-meson invariant mass.

VI.9 Conclusion

We measured the branching fractions of the B^0 and B^0_s decays to the final state $K^0_S h^+ h'^-$ relative to that of the decay $B^0 \to K^0_S \pi^+ \pi^-$. The study we performed uses the run 1 and the run 2 data sets. This corresponds to an integrated luminosity of about 9 fb^{-1}. We combine the results from a simultaneous fit to the invariant mass distribution of the $B^0_{(s)} \to K^0_S h^+ h'^-$ decays.

Compared to the run 1 LHCb study, the preliminary results we quote in Sec. VI.8 have, as expected, smaller statistical uncertainties. In most cases, the current results on the $K^0_S h^+ h'^-$ ratios of branching fractions are limited by systematic uncertainties. Most of the results are not in a good agreement with the with the results from the run 1 study [10], nor with B-factories results when relevant. The study of the systematic effects is still ongoing. In particular, the uncertainties related to the efficiency are not quoted as these are not available

yet. For the time being, we mentioned only the dominant systematic effects, mostly related to the choice of the model of some of the fit contributions. These numbers have a limitation though: this first iteration based on differences in the central value with the baseline and modified models is vulnerable to statistical fluctuations in the data sample. As such, further studies of the systematic effects might reduce them. A more evolved systematic uncertainty study involving toy studies would here account for these possible fluctuations. Further discussions and perspectives on this study are discussed in Chap. VII.

Chapter VII

Conclusion

The work described in this thesis was focused on studying charmless three-body decays of B mesons. It also included developments on LHCb's scintillating fibre tracker monitoring.

We began with insights into the CKM angle γ. The study discussed in Chapter III enables constraints on γ deduced from charmless 3-body decays of B mesons. My aim was to measure γ using results from BaBar amplitude analyses. The analysis that I performed extended and tested a method suggested by London et al. [15]. Under a few assumptions, such as that the flavour SU(3) symmetry holds, the amplitude of the decay should obey certain symmetry relations, and information on γ can be deduced from each of the six symmetrisations. The feasibility of this method was tested by Bertholet et al. [16] on the fully symmetric state, and encouraging results were found, though interpretation was limited by the presence of multiple, ambiguous solutions. The work discussed in this thesis tested the same method in the context of the fully antisymmetric state. Unfortunately, in this situation, the Dalitz planes that we study do not contain enough information to extract γ. However, combining multiple symmetry states could allow stronger constraints on γ to be extracted in a future study.

The second aspect of the work discussed here is a measurement of the branching fractions of $B^0_{(s)} \to K^0_S h^+ h'^-$. This analysis is the update of an LHCb run 1 analysis. It now includes the full dataset collected during run 1 and run 2, for a total integrated luminosity of around 9 fb^{-1}. The ratios of branching fractions of decays of the form $K^0_S h^+ h'^-$ were updated. Excluding the $K^0_S K^+ K^-$ final state (which is included in the fit but blinded), the results

are the following:

$$\frac{\mathcal{B}(B^0 \to K^0_S K^+\pi^-)}{\mathcal{B}(B^0 \to K^0_S \pi^+\pi^-)} = 0.150 \pm 0.004(\text{Stat}) \pm 0.018(\text{Syst}),$$
$$\frac{\mathcal{B}(B^0_s \to K^0_S \pi^+\pi^-)}{\mathcal{B}(B^0 \to K^0_S \pi^+\pi^-)} = 0.284 \pm 0.006(\text{Stat}) \pm 0.022(\text{Syst}) \pm 0.009\,(\text{f}_\text{s}/\text{f}_\text{d}),$$
$$\frac{\mathcal{B}(B^0 \to K^0_S K^+K^-)}{\mathcal{B}(B^0 \to K^0_S \pi^+\pi^-)} = 0.647 \pm 0.009(\text{Stat}) \pm 0.010(\text{Syst}),$$
$$\frac{\mathcal{B}(B^0_s \to K^0_S K^+\pi^-)}{\mathcal{B}(B^0 \to K^0_S \pi^+\pi^-)} = 1.924 \pm 0.003(\text{Stat}) \pm 0.010(\text{Syst}) \pm 0.060\,(\text{f}_\text{s}/\text{f}_\text{d}).$$

where the uncertainties are, in order, statistical, systematic uncertainties, and, when relevant, due to external input on f_s/f_d. These are dominated by systematic uncertainties. The first and the third ratio use only B^0 decays, and so can be compared to results from the B-factories ; the first ratio is in good agreement, it is not the case of the third ratio. In general, these results are in poor agreement with the run 1 analysis study but the values we present here suffer from known limitations. Further studies of the $K^0_S h^+ h'^-$ efficiency model are necessary. This study also lays the ground for future Dalitz plane amplitude analyses, which will benefit from the clean selection, improved crossfeed rejection, and efficiency model as well as the improved statistics. In particular, the decay amplitude of $B^0_d \to K^0_S K^+K^-$ was studied with the run 1 data but the dataset available at that time was not enough to disentangle the multiple solutions found in amplitude fits. With these new data, toy studies by another member of the group indicate that ambiguities should be reduced.

The last subject tackled in this dissertation is the upgrade of LHCb's downstream tracker. The LHCb collaboration is about to finish the installation of its upgrade detector. The detector is being upgraded in order to allow the collaboration to collect 50 fb^{-1} by the end of the run 4. I worked on the development of monitoring tools, and more specifically, the developments of a monitoring panel and the update of the tracker calibration procedure.

The phase I of the LHCb upgrade should bring new exciting insights on charmless 3-body B-meson decays. The increased statistics will allow searches for new physics processes and tests of Standard Model predictions to be performed at a great level of precision. In particular, studies of charmless 3-body B-meson decays could yield precise descriptions of the amplitude pattern. These studies could also in the future help constrain CKM quantities such as $\sin(2\beta_{\text{eff}})$. With Belle II being collecting data and LHCb being about to start a new data-taking run, we should expect more precise descriptions of the amplitude content of charmless 3-body B-meson decays to be available in the

future. With larger statistics and the addition of more symmetry states, we can also expect that the extraction of the CKM angle γ using charmless 3-body decays of B mesons will yield exciting new results. The most dramatic scenario would, of course, be a value of γ different from that seen in tree-level decays, which would indicate the influence of physics beyond the Standard Model.

Appendices

Appendix A

Supplementary material for the extraction of γ from three-body charmless decays of the B meson

A.1 Expression of the observables in term of the theoretical parameters in the case of the antisymmetric states

$$X_{K^+\pi^+\pi^-} = \frac{2}{9}(9C_1^2 + C_1^2\kappa^2 + 4C_2^2\kappa^2 + 9P^2 + 9T_1^2\kappa^2 + 9T_2^2 + 18C_1T_2cos(\phi_{C_1}) + 4C_1C_2\kappa^2cos(\phi_{C_1} - \phi_{C_2})$$
$$- 6C_1\kappa Pcos(\phi_{C_1} - \phi_P) - 12C_2\kappa Pcos(\phi_{C_2} - \phi_P) + 6C_1\kappa^2T_1cos(\phi_{C_1} - \phi_{T_1}) + 12C_2\kappa^2T_1cos(\phi_{C_2} - \phi_{T_1})$$
$$- 18P\kappa T_1cos(\phi_P - \phi_{T_1}) + 6cos(\gamma)(C_1^2\kappa + C_1\kappa T_2cos(\phi_{C_1}) + 2C_1C_2\kappa cos(\phi_{C_1}$$
$$- \phi_{C_2}) + 2C_2T_2\kappa cos(\phi_{C_2}) - 3C_1Pcos(\phi_{C_1} - \phi_P) - 3PT_2cos(\phi_P) + 3C_1\kappa T_1cos(\phi_{C_1} - \phi_{T_1})$$
$$+ 3\kappa T_1T_2cos(\phi_{T_1})))$$

$$Y_{K^+\pi^+\pi^-} = \frac{4}{3}sin(\gamma)(C_1\kappa T_2sin(\phi_{C_1}) - 2C_1C_2\kappa sin(\phi_{C_1} - \phi_{C_2}) + 2C_2\kappa T_2sin(\phi_{C_2}) + 3C_1Psin(\phi_{C_1} - \phi_P)$$
$$- 3PT_2sin(\phi_P) - 3C_1\kappa T_1sin(\phi_{C_1} - \phi_{T_1}) + 3\kappa T_1T_2sin(\phi_{T_1}))$$

$$X_{K_s\pi^+\pi^0} = \frac{1}{9}(9C_2^2 + C_1^2\kappa^2 + 4C_2^2\kappa^2 + 36P^2 + 9T_1^2 + 9T_2^2\kappa^2 + 6C_1\kappa^2T_2cos(\phi_{C_1}) + 4C_1C_2\kappa^2cos(\phi_{C_1} - \phi_{C_2})$$
$$+ 12C_2\kappa^2T_2cos(\phi_{C_2}) + 12C_1\kappa Pcos(\phi_{C_1} - \phi_P) + 24C_2\kappa Pcos(\phi_{C_2} - \phi_P) + 36\kappa PT_2cos(\phi_P) + 18C_2T_1cos(\phi_{C_2} - \phi_{T_1})$$
$$+ 6cos(\gamma)(2C_2^2\kappa + C_2C_1\kappa cos(\phi_{C_1} - \phi_{C_2}) + 3C_2\kappa T_2cos(\phi_{C_2}) + 6C_2Pcos(\phi_{C_2} - \phi_P) + C_1\kappa T_1cos(\phi_{C_1} - \phi_{T_1})$$
$$+ 2C_2\kappa T_1cos(\phi_{C_2} - \phi_{T_1}) + 6PT_1cos(\phi_P - \phi_{T_1}) + 3\kappa T_1T_2cos(\phi_{T_1})))$$

$$Y_{K_s\pi^+\pi^0} = \frac{2}{3}sin(\gamma)(C_2C_1\kappa sin(\phi_{C_1} - \phi_{C_2}) - 3C_2\kappa T_2sin(\phi_{C_2}) - 6C_2Psin(\phi_{C_2} - \phi_P) + C_1\kappa T_1sin(\phi_{C_1} - \phi_{T_1})$$
$$+ 2C_2\kappa T_1sin(\phi_{C_2} - \phi_{T_1}) + 6PT_1sin(\phi_P - \phi_{T_1}) - 3\kappa T_1T_2sin(\phi_{T_1}))$$

A.1 Expression of the observables in term of the theoretical parameters in the case of the antisymmetric states

$$
\begin{aligned}
X_{K_s\pi^+\pi^-} = \frac{2}{9}(&9C_1^2 + 4C_1^2\kappa^2 + C_2^2\kappa^2 + 9P^2 + 9T_1^2 + 9T_1^2\kappa^2 + 6\kappa(2C_1^2 + 3T_1^2)cos(\gamma) + 4C_1C_2\kappa^2 cos(\phi_{C_1} - \phi_{C_2}) \\
&+ 3C_2C_1\kappa cos(\gamma + \phi_{C_1} - \phi_{C_2}) + 3C_2C_1\kappa cos(\gamma - \phi_{C_1} + \phi_{C_2}) \\
&+ 12C_1\kappa Pcos(\phi_{C_1} - \phi_P) + 9C_1Pcos(\gamma + \phi_{C_1} - \phi_P) + 6C_2\kappa Pcos(\phi_{C_2} - \phi_P) \\
&+ 9C_1Pcos(\gamma - \phi_{C_1} + \phi_P) + 18C_1T_1cos(\phi_{C_1} - \phi_{T_1}) + 12C_1\kappa^2T_1cos(\phi_{C_1} - \phi_{T_1}) + 15C_1\kappa T_1cos(\gamma + \phi_{C_1} - \phi_{T_1}) \\
&+ 6C_2\kappa^2T_1cos(\phi_{C_2} - \phi_{T_1}) + 3C_2\kappa T_1cos(\gamma + \phi_{C_2} - \phi_{T_1}) + 18P\kappa T_1cos(\phi_P - \phi_{T_1}) + 9PT_1cos(\gamma + \phi_P - \phi_{T_1}) \\
&+ 15C_1\kappa T_1cos(\gamma - \phi_{C_1} + \phi_{T_1}) + 3C_2\kappa T_1cos(\gamma - \phi_{C_2} + \phi_{T_1}) + 9PT_1cos(\gamma - \phi_P + \phi_{T_1}))
\end{aligned}
$$

$$
\begin{aligned}
Y_{K_s\pi^+\pi^-} = -(\frac{4}{3})&sin(\gamma)(C_2C_1\kappa sin(\phi_{C_1} - \phi_{C_2}) + 3C_1Psin(\phi_{C_1} - \phi_P) + T_1(C_1\kappa sin(\phi_{C_1} - \phi_{T_1}) - C_2\kappa sin(\phi_{C_2} - \phi_{T_1}) \\
&- 3Psin(\phi_P - \phi_{T_1})))
\end{aligned}
$$

$$
\begin{aligned}
Z_{K_s\pi^+\pi^-} = -(\frac{2}{3})&(2C_1^2\kappa + 3\kappa T_1^2 + 3(C_1^2 + T_1^2)cos(\gamma) + C_2C_1\kappa cos(\phi_{C_1} - \phi_{C_2}) + 3C_1Pcos(\phi_{C_1} - \phi_P) \\
&+ 5C_1\kappa T_1cos(\phi_{C_1} - \phi_{T_1}) + 3C_1T_1cos(\gamma + \phi_{C_1} - \phi_{T_1}) + C_2\kappa T_1cos(\phi_{C_2} - \phi_{T_1}) + 3PT_1cos(\phi_P - \phi_{T_1}) \\
&+ 3C_1T_1cos(\gamma - \phi_{C_1} + \phi_{T_1}))sin(\gamma)
\end{aligned}
$$

Supplementary material for the extraction of γ from three-body charmless decays of the B meson

A.1 Expression of the observables in term of the theoretical parameters in the case of the antisymmetric states

$$
\begin{aligned}
X_{K^+\pi^0\pi^-} = \frac{1}{9}(&9C_2^2 + C_1^2\kappa^2 + 16C_2^2\kappa^2 + 36P^2 + 9T_1^2 + 36T_2^2 + 9T_2^2\kappa^2 + 12\kappa(2C_2^2 + 3T_2^2)cos(\gamma) \\
&- 12C_1\kappa T_2 cos(\gamma - \phi_{C_1}) - 6C_1\kappa^2 T_2 cos(\phi_{C_1}) \\
&+ 57C_2\kappa T_2 cos(\gamma - \phi_{C_2}) + 18C_2T_2 cos(2\gamma - \phi_{C_2}) - 8C_1C_2\kappa^2 cos(\phi_{C_1} - \phi_{C_2}) \\
&-3C_2C_1\kappa cos(\gamma+\phi_{C_1}-\phi_{C_2})+18C_2T_2cos(\phi_{C_2})+24C_2\kappa^2T_2cos(\phi_{C_2})+9C_2\kappa T_2cos(\gamma+\phi_{C_2})-3C_2C_1\kappa cos(\gamma-\phi_{C_1}+\phi_{C_2}) \\
&- 72PT_2cos(\gamma - \phi_P) + 12C_1\kappa Pcos(\phi_{C_1} - \phi_P) - 48C_2\kappa Pcos(\phi_{C_2} \\
&- \phi_P) - 18C_2Pcos(\gamma + \phi_{C_2} - \phi_P) - 36\kappa PT_2cos(\phi_P) \\
&- 18C_2Pcos(\gamma - \phi_{C_2} + \phi_P) - 9\kappa T_1T_2cos(\gamma - \phi_{T_1}) \\
&- 18T_1T_2cos(2\gamma - \phi_{T_1}) + 3C_1\kappa T_1cos(\gamma + \phi_{C_1} - \phi_{T_1}) \\
&- 18C_2T_1cos(\phi_{C_2} - \phi_{T_1}) \\
&- 12C_2\kappa T_1cos(\gamma + \phi_{C_2} - \phi_{T_1}) + 18PT_1cos(\gamma + \phi_P - \phi_{T_1}) \\
&- 18T_1T_2cos(\phi_{T_1}) - 9\kappa T_1T_2cos(\gamma + \phi_{T_1}) + 3C_1\kappa T_1cos(\gamma - \phi_{C_1} + \phi_{T_1}) \\
&- 12C_2\kappa T_1cos(\gamma - \phi_{C_2} + \phi_{T_1}) + 18PT_1cos(\gamma - \phi_P + \phi_{T_1}))
\end{aligned}
$$

$$
\begin{aligned}
Y_{K^+\pi^0\pi^-} = \frac{2}{3}&sin(\gamma)(6C_2T_2sin(\gamma - \phi_{C_2}) - C_2C_1\kappa sin(\phi_{C_1} - \phi_{C_2}) - 3C_2\kappa T_2sin(\phi_{C_2}) + 6C_2Psin(\phi_{C_2} - \phi_P) \\
&- 6T_1T_2sin(\gamma - \phi_{T_1}) + C_1\kappa T_1sin(\phi_{C_1} - \phi_{T_1}) - 4C_2\kappa T_1sin(\phi_{C_2} - \phi_{T_1}) + 6PT_1sin(\phi_P - \phi_{T_1}) + 3\kappa T_1T_2sin(\phi_{T_1}))
\end{aligned}
$$

$$
\begin{aligned}
X_{K_sK^+K^-} = \frac{2}{9}&(9C_1^2 + C_1^2\kappa^2 + 4C_2^2\kappa^2 + 9P^2 + 9T_2^2 - 18C_1T_2cos(\phi_{C_1}) + 4C_1C_2\kappa^2cos(\phi_{C_1} - \phi_{C_2}) \\
&- 6C_1\kappa Pcos(\phi_{C_1} - \phi_P) - 12C_2\kappa Pcos(\phi_{C_2} - \phi_P) - 6cos(\gamma)(C_1^2\kappa - C_1\kappa T_2cos(\phi_{C_1}) + 2C_1C_2\kappa cos(\phi_{C_1} - \phi_{C_2}) \\
&- 2C_2T_2\kappa cos(\phi_{C_2}) - 3C_1Pcos(\phi_{C_1} - \phi_P) + 3PT_2cos(\phi_P)))
\end{aligned}
$$

$$
\begin{aligned}
Y_{K_sK^+K^-} = \frac{4}{3}&sin(\gamma)(C_1\kappa T_2sin(\phi_{C_1}) + 2C_1C_2\kappa sin(\phi_{C_1} - \phi_{C_2}) + 2C_2\kappa T_2sin(\phi_{C_2}) - 3C_1Psin(\phi_{C_1} - \phi_P) - 3PT_2sin(\phi_P)) \\
Z_{K_sK^+K^-} = \frac{2}{3}&(C_1^2\kappa - 3(C_1^2 + T_2^2)cos(\gamma) + 3C_1T_2cos(\gamma - \phi_{C_1}) - C_1\kappa T_2cos(\phi_{C_1}) + 3C_1T_2cos(\gamma + \phi_{C_1}) \\
&+ 2C_1C_2\kappa cos(\phi_{C_1} - \phi_{C_2}) - 2C_2T_2\kappa cos(\phi_{C_2}) - 3C_1Pcos(\phi_{C_1} - \phi_P) + 3PT_2cos(\phi_P))sin(\gamma)
\end{aligned}
$$

Supplementary material for the extraction of γ from three-body charmless decays of the B meson

Appendix B

Supplementary material for the branching fraction measurements of $B^0_{(s)} \to K^0_S h^\pm h'^\mp$ modes

B.1 Simultaneous fit to the data results

B.2 Systematic uncertainty study results

The results from the systematic uncertainty studies from Sec.VI.7 are given in the followingtables for each of the decay modes:

- Table I gives the results for the $B^0 \to K^0_S K^+\pi^-$ decay mode
- Table II gives the results for the $B^0 \to K^0_S \pi^+ K^-$ decay mode
- Table III gives the results for the $B^0 \to K^0_S \pi^+\pi^-$ decay mode
- Table IV gives the results for the $B^0_s \to K^0_S K^+\pi^-$ decay mode
- Table V gives the results for the $B^0_s \to K^0_S \pi^+ K^-$ decay mode
- Table VI gives the results for the $B^0_s \to K^0_S \pi^+\pi^-$ decay mode

In each of these tables, we give first the yield measured in the fit to the data. It is followed by the statistical uncertainty. We quote then, in this order, the systematic uncertainties related to the following source:

- Fixed signal shape parameters (Sig. p.)

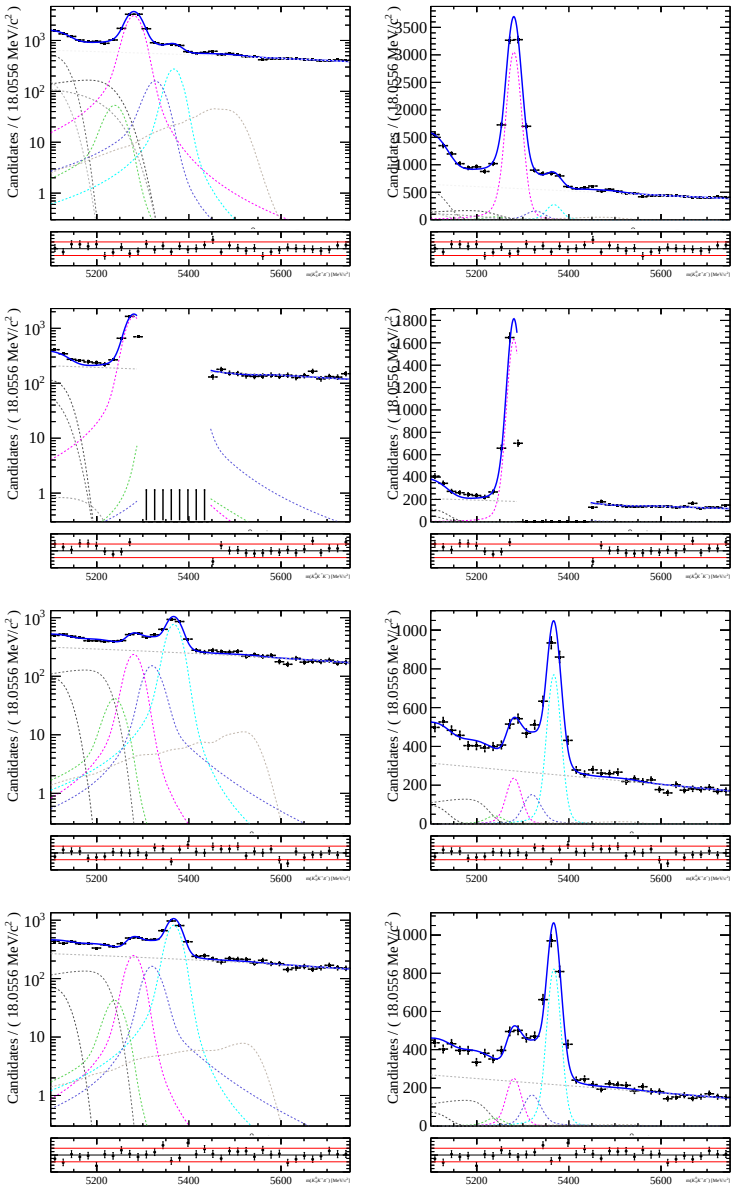

Figure B.1: Result of the simultaneous fit to the data. We show here the results on 2018, DD. The selection has been optimised on the principal signal peak. From top to bottom, $K^0_S\pi^+\pi^-$, $K^0_S K^+K^-$, $K^0_S K^+\pi^-$ and $K^0_S\pi^+K^-$ are shown. The left-hand-side plots have a logarithmic scale, and the plots on the right show the same data on a linear scale. The magenta dashed line is the B^0 signal contribution. The B^0_s signal peak is in cyan. The crossfeed backgrounds are the blue and green dashe lines. The grey dashed line peaking above 5400 MeV is the Λ_b crossfeed background. To the left of the plot, the grey dashed lines illustrate the partially reconstructed background contributions and the combinatorial background is the grey straight line. In the $K^0_S K^+K^-$ spectra, the region around the B^0_s signal (5320-5450 MeV) is blinded.

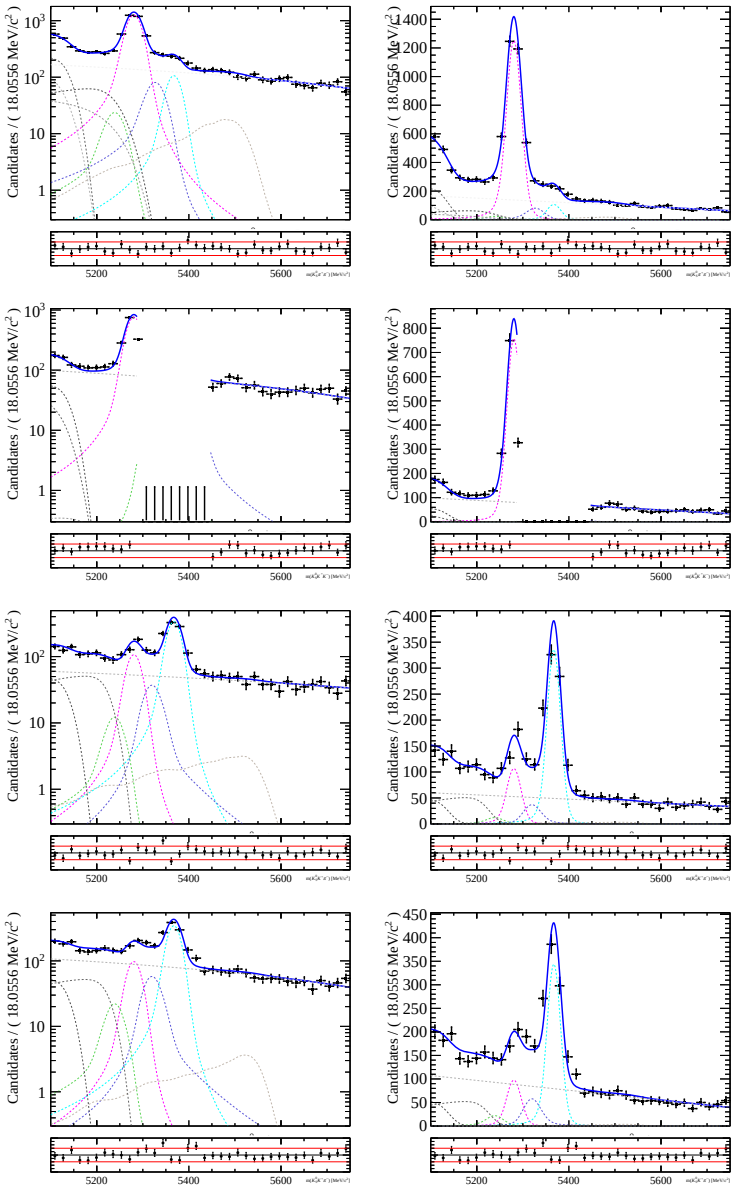

Figure B.2: Result of the simultaneous fit to the data. We show here the results on 2018, LL. The selection has been optimised on the principal signal peak. From top to bottom, $K^0_S\pi^+\pi^-$, $K^0_S K^+K^-$, $K^0_S K^+\pi^-$ and $K^0_S\pi^+K^-$ are shown. The left-hand-side plots have a logarithmic scale, and the plots on the right show the same data on a linear scale. The magenta dashed line is the B^0 signal contribution. The B^0_s signal peak is in cyan. The crossfeed backgrounds are the blue and green dashe lines. The grey dashed line peaking above 5400 MeV is the Λ_b crossfeed background. To the left of the plot, the grey dashed lines illustrate the partially reconstructed background contributions and the combinatorial background is the grey straight line. In the $K^0_S K^+K^-$ spectra, the region around the B^0_s signal (5320-5450 MeV) is blinded.

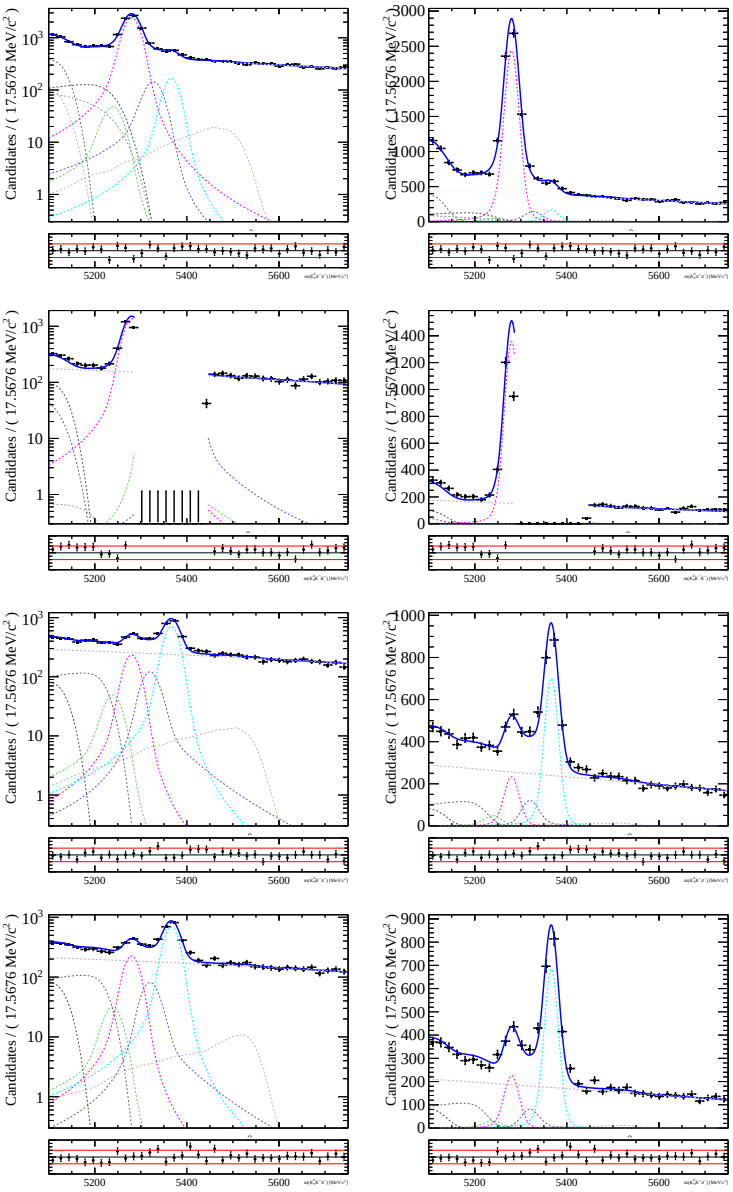

Figure B.3: Result of the simultaneous fit to the data. We show here the results on 2017, DD. The selection has been optimised on the principal signal peak. From top to bottom, $K^0_S\pi^+\pi^-$, $K^0_S K^+K^-$, $K^0_S K^+\pi^-$ and $K^0_S\pi^+K^-$ are shown. The left-hand-side plots have a logarithmic scale, and the plots on the right show the same data on a linear scale. The magenta dashed line is the B^0 signal contribution. The B^0_s signal peak is in cyan. The crossfeed backgrounds are the blue and green dashe lines. The grey dashed line peaking above 5400 MeV is the Λ_b crossfeed background. To the left of the plot, the grey dashed lines illustrate the partially reconstructed background contributions and the combinatorial background is the grey straight line. In the $K^0_S K^+K^-$ spectra, the region around the B^0_s signal (5320-5450 MeV) is blinded.

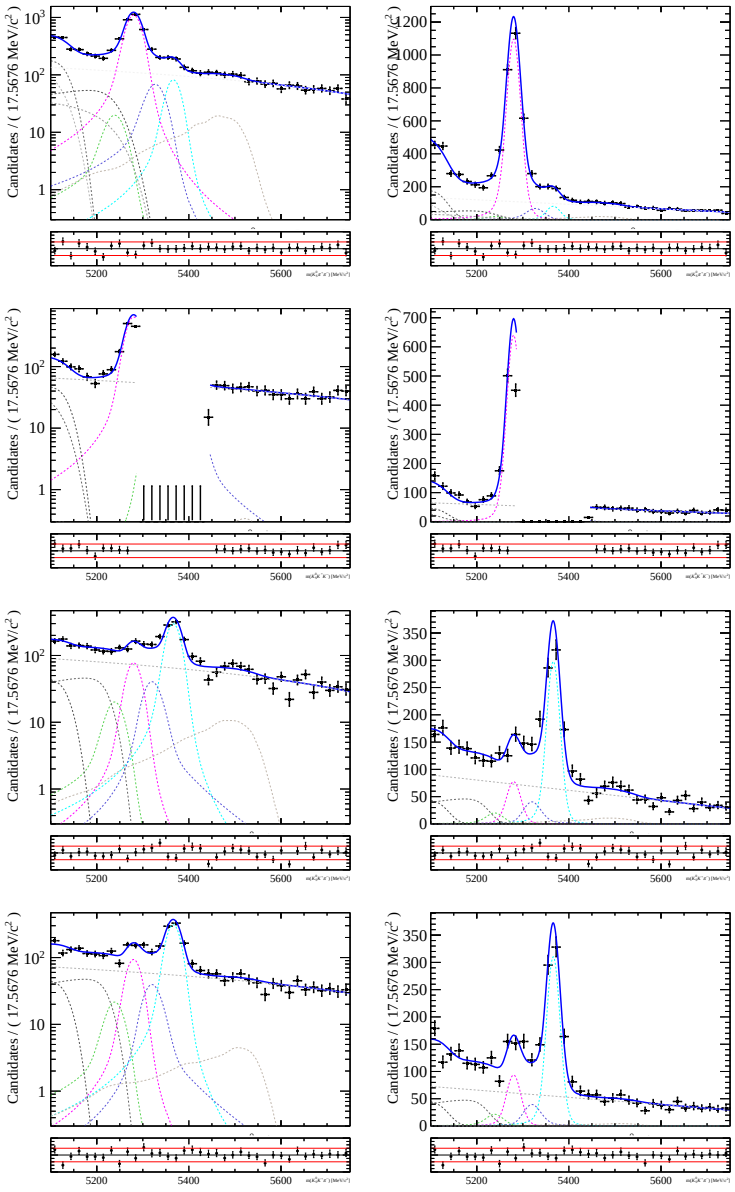

Figure B.4: Result of the simultaneous fit to the data. We show here the results on 2017, LL. The selection has been optimised on the principal signal peak. From top to bottom, $K^0_S\pi^+\pi^-$, $K^0_S K^+K^-$, $K^0_S K^+\pi^-$ and $K^0_S\pi^+K^-$ are shown. The left-hand-side plots have a logarithmic scale, and the plots on the right show the same data on a linear scale. The magenta dashed line is the B^0 signal contribution. The B^0_s signal peak is in cyan. The crossfeed backgrounds are the blue and green dashe lines. The grey dashed line peaking above 5400 MeV is the Λ_b crossfeed background. To the left of the plot, the grey dashed lines illustrate the partially reconstructed background contributions and the combinatorial background is the grey straight line. In the $K^0_S K^+K^-$ spectra, the region around the B^0_s signal (5320-5450 MeV) is blinded.

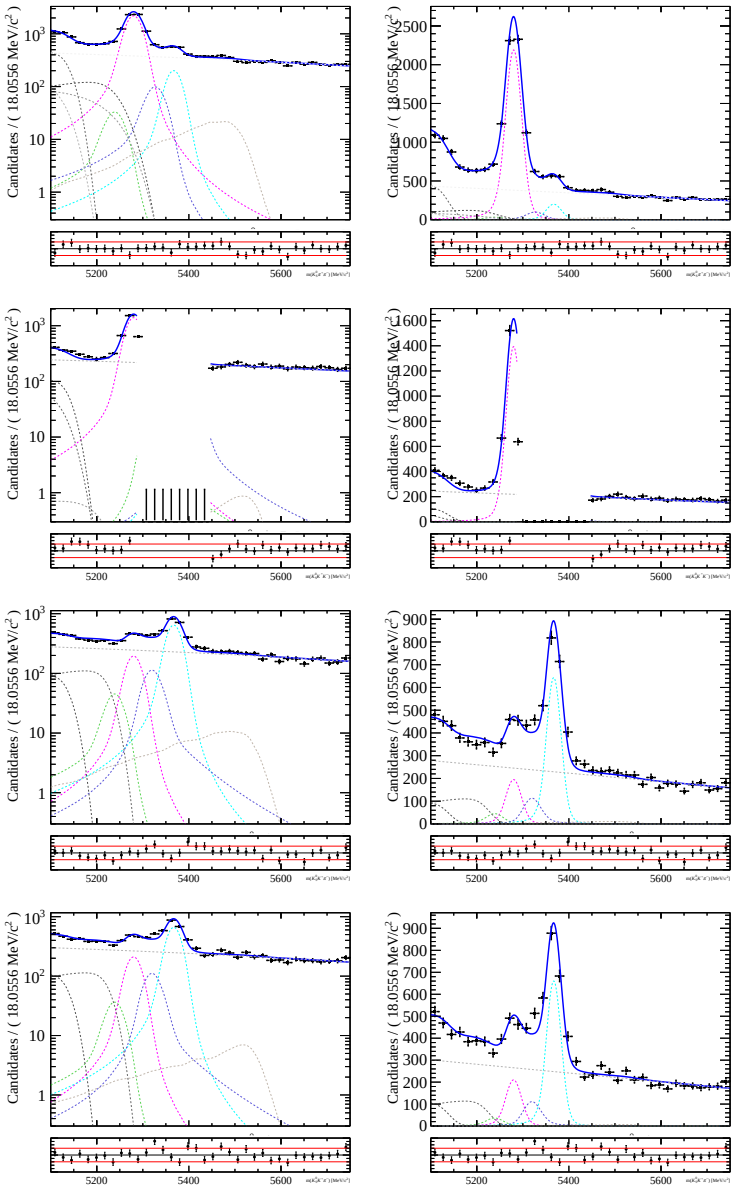

Figure B.5: Result of the simultaneous fit to the data. We show here the results on 2016, DD. The selection has been optimised on the principal signal peak. From top to bottom, $K^0_S\pi^+\pi^-$, $K^0_S K^+K^-$, $K^0_S K^+\pi^-$ and $K^0_S\pi^+K^-$ are shown. The left-hand-side plots have a logarithmic scale, and the plots on the right show the same data on a linear scale. The magenta dashed line is the B^0 signal contribution. The B^0_s signal peak is in cyan. The crossfeed backgrounds are the blue and green dashe lines. The grey dashed line peaking above 5400 MeV is the Λ_b crossfeed background. To the left of the plot, the grey dashed lines illustrate the partially reconstructed background contributions and the combinatorial background is the grey straight line. In the $K^0_S K^+K^-$ spectra, the region around the B^0_s signal (5320-5450 MeV) is blinded.

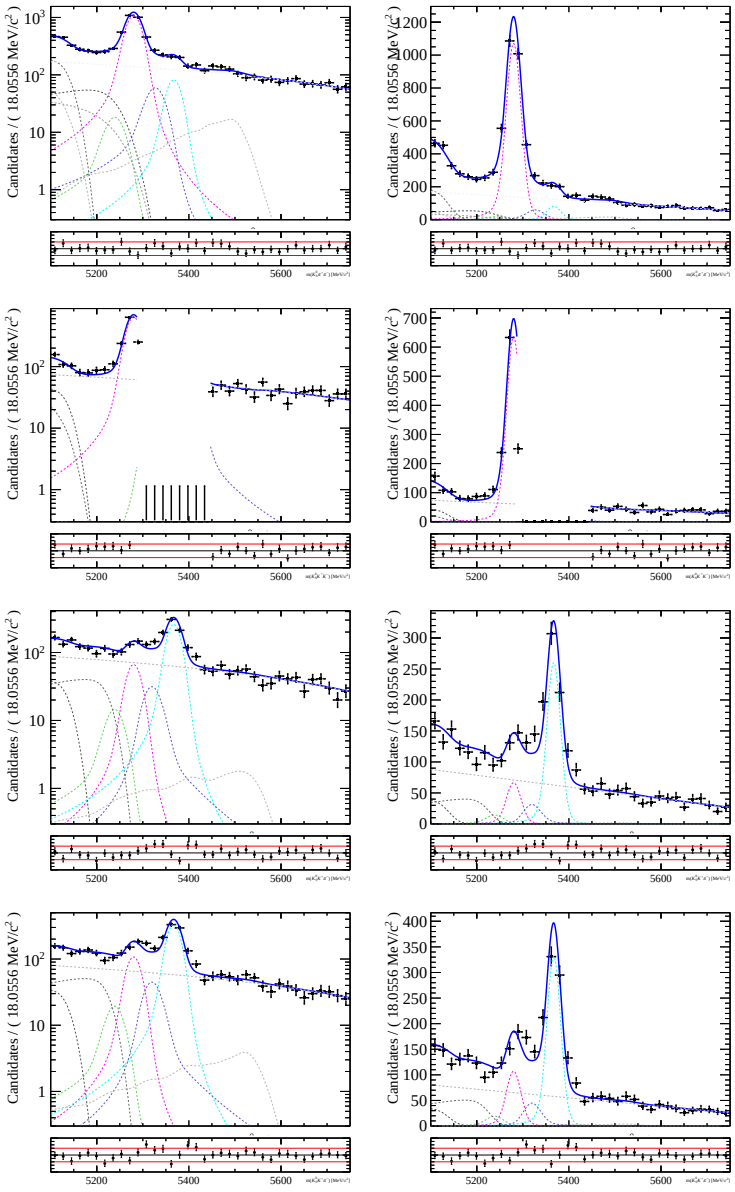

Figure B.6: Result of the simultaneous fit to the data. We show here the results on 2016, LL. The selection has been optimised on the principal signal peak. From top to bottom, $K^0_S\pi^+\pi^-$, $K^0_S K^+K^-$, $K^0_S K^+\pi^-$ and $K^0_S\pi^+K^-$ are shown. The left-hand-side plots have a logarithmic scale, and the plots on the right show the same data on a linear scale. The magenta dashed line is the B^0 signal contribution. The B^0_s signal peak is in cyan. The crossfeed backgrounds are the blue and green dashe lines. The grey dashed line peaking above 5400 MeV is the Λ_b crossfeed background. To the left of the plot, the grey dashed lines illustrate the partially reconstructed background contributions and the combinatorial background is the grey straight line. In the $K^0_S K^+K^-$ spectra, the region around the B^0_s signal (5320-5450 MeV) is blinded.

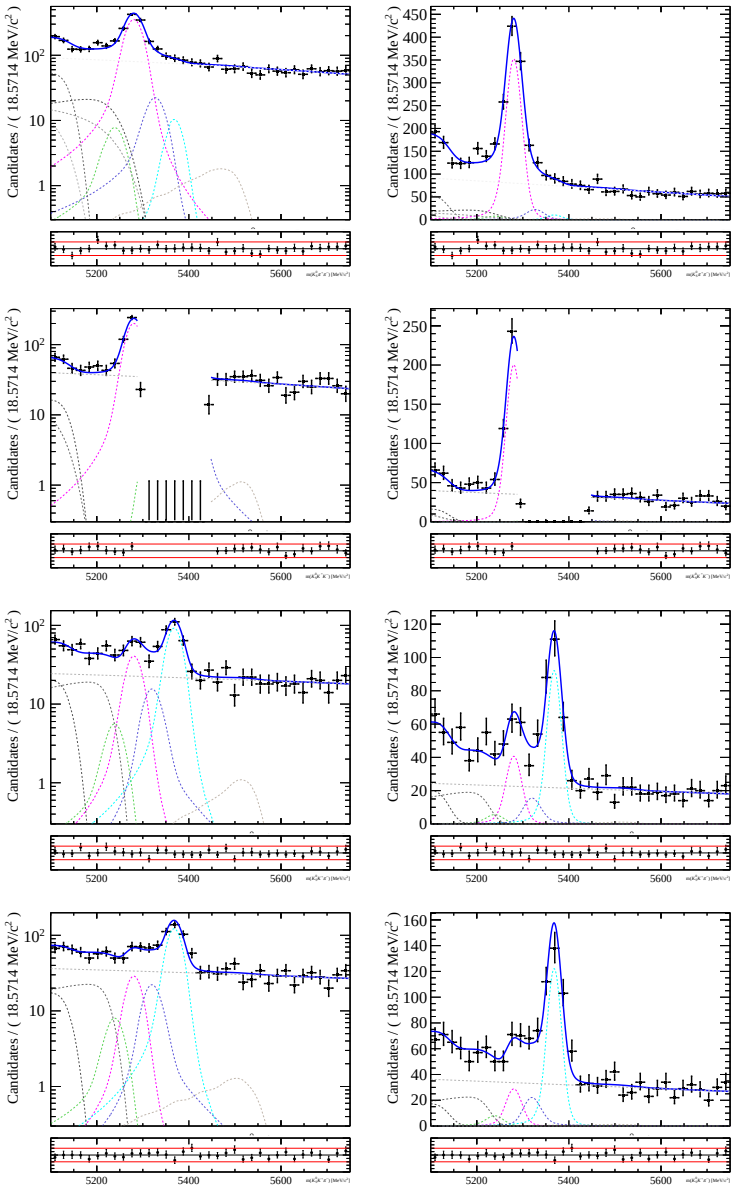

Figure B.7: Result of the simultaneous fit to the data. We show here the results on 2015, DD. The selection has been optimised on the principal signal peak. From top to bottom, $K^0_S\pi^+\pi^-$, $K^0_S K^+K^-$, $K^0_S K^+\pi^-$ and $K^0_S\pi^+K^-$ are shown. The left-hand-side plots have a logarithmic scale, and the plots on the right show the same data on a linear scale. The magenta dashed line is the B^0 signal contribution. The B^0_s signal peak is in cyan. The crossfeed backgrounds are the blue and green dashe lines. The grey dashed line peaking above 5400 MeV is the Λ_b crossfeed background. To the left of the plot, the grey dashed lines illustrate the partially reconstructed background contributions and the combinatorial background is the grey straight line. In the $K^0_S K^+K^-$ spectra, the region around the B^0_s signal (5320-5450 MeV) is blinded.

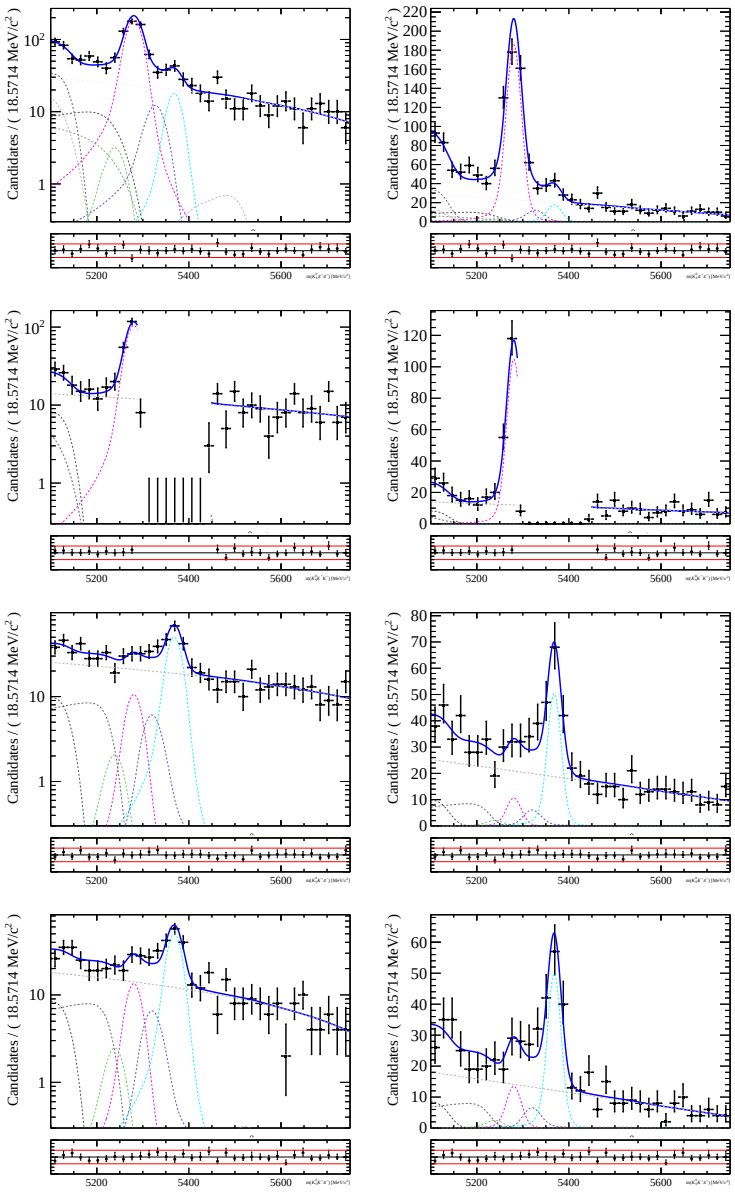

Figure B.8: Result of the simultaneous fit to the data. We show here the results on 2015, LL. The selection has been optimised on the principal signal peak. From top to bottom, $K^0_S\pi^+\pi^-$, $K^0_S K^+K^-$, $K^0_S K^+\pi^-$ and $K^0_S\pi^+K^-$ are shown. The left-hand-side plots have a logarithmic scale, and the plots on the right show the same data on a linear scale. The magenta dashed line is the B^0 signal contribution. The B^0_s signal peak is in cyan. The crossfeed backgrounds are the blue and green dashe lines. The grey dashed line peaking above 5400 MeV is the Λ_b crossfeed background. To the left of the plot, the grey dashed lines illustrate the partially reconstructed background contributions and the combinatorial background is the grey straight line. In the $K^0_S K^+K^-$ spectra, the region around the B^0_s signal (5320-5450 MeV) is blinded.

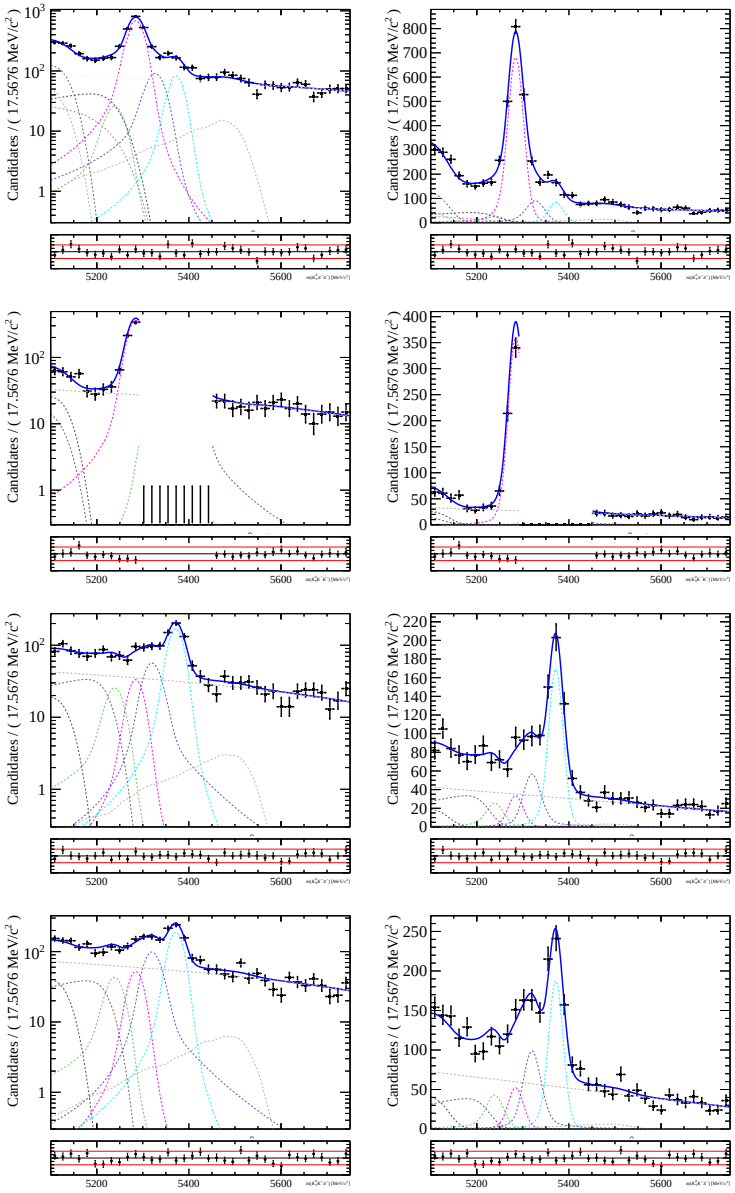

Figure B.9: Result of the simultaneous fit to the data. We show here the results on 2012b, DD. The selection has been optimised on the principal signal peak. From top to bottom, $K^0_S\pi^+\pi^-$, $K^0_S K^+K^-$, $K^0_S K^+\pi^-$ and $K^0_S\pi^+K^-$ are shown. The left-hand-side plots have a logarithmic scale, and the plots on the right show the same data on a linear scale. The magenta dashed line is the B^0 signal contribution. The B^0_s signal peak is in cyan. The crossfeed backgrounds are the blue and green dashe lines. The grey dashed line peaking above 5400 MeV is the Λ_b crossfeed background. To the left of the plot, the grey dashed lines illustrate the partially reconstructed background contributions and the combinatorial background is the grey straight line. In the $K^0_S K^+K^-$ spectra, the region around the B^0_s signal (5320-5450 MeV) is blinded.

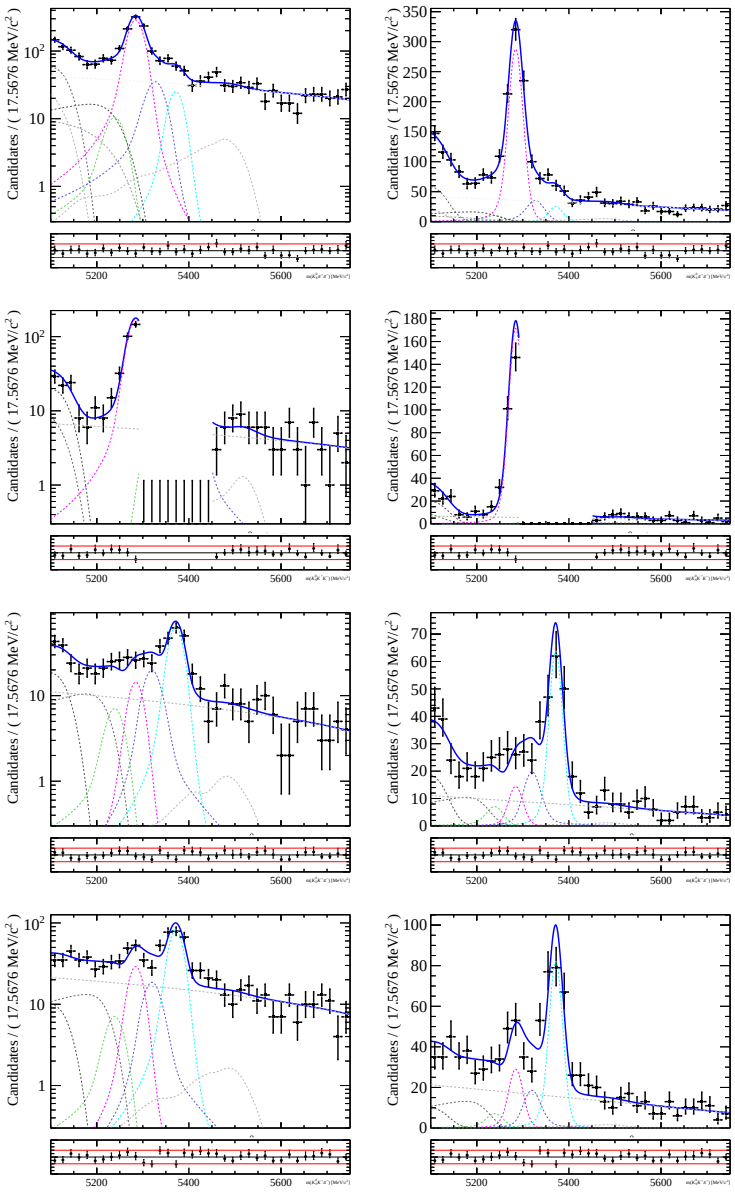

Figure B.10: Result of the simultaneous fit to the data. We show here the results on 2012b, LL. The selection has been optimised on the principal signal peak. From top to bottom, $K^0_S\pi^+\pi^-$, $K^0_S K^+K^-$, $K^0_S K^+\pi^-$ and $K^0_S\pi^+K^-$ are shown. The left-hand-side plots have a logarithmic scale, and the plots on the right show the same data on a linear scale. The magenta dashed line is the B^0 signal contribution. The B^0_s signal peak is in cyan. The crossfeed backgrounds are the blue and green dashe lines. The grey dashed line peaking above 5400 MeV is the Λ_b crossfeed background. To the left of the plot, the grey dashed lines illustrate the partially reconstructed background contributions and the combinatorial background is the grey straight line. In the $K^0_S K^+K^-$ spectra, the region around the B^0_s signal (5320-5450 MeV) is blinded.

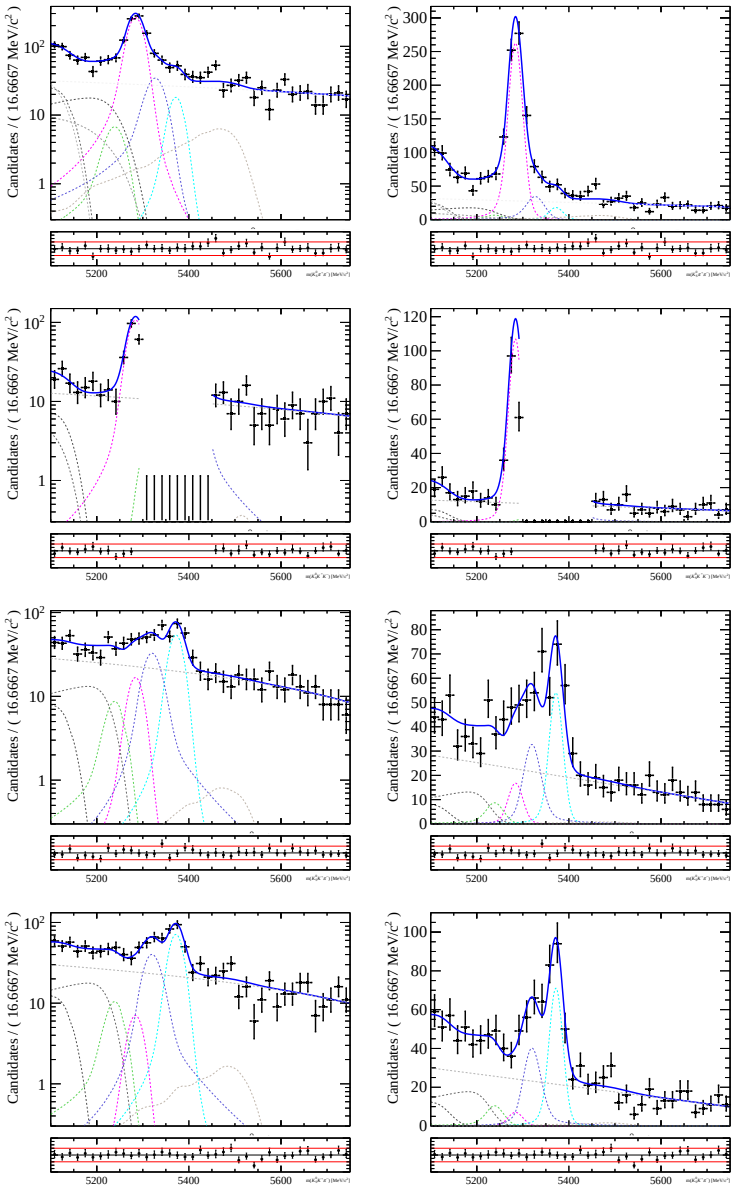

Figure B.11: Result of the simultaneous fit to the data. We show here the results on 2012a, DD. The selection has been optimised on the principal signal peak. From top to bottom, $K^0_S\pi^+\pi^-$, $K^0_S K^+K^-$, $K^0_S K^+\pi^-$ and $K^0_S\pi^+K^-$ are shown. The left-hand-side plots have a logarithmic scale, and the plots on the right show the same data on a linear scale. The magenta dashed line is the B^0 signal contribution. The B^0_s signal peak is in cyan. The crossfeed backgrounds are the blue and green dashe lines. The grey dashed line peaking above 5400 MeV is the Λ_b crossfeed background. To the left of the plot, the grey dashed lines illustrate the partially reconstructed background contributions and the combinatorial background is the grey straight line. In the $K^0_S K^+K^-$ spectra, the region around the B^0_s signal (5320-5450 MeV) is blinded.

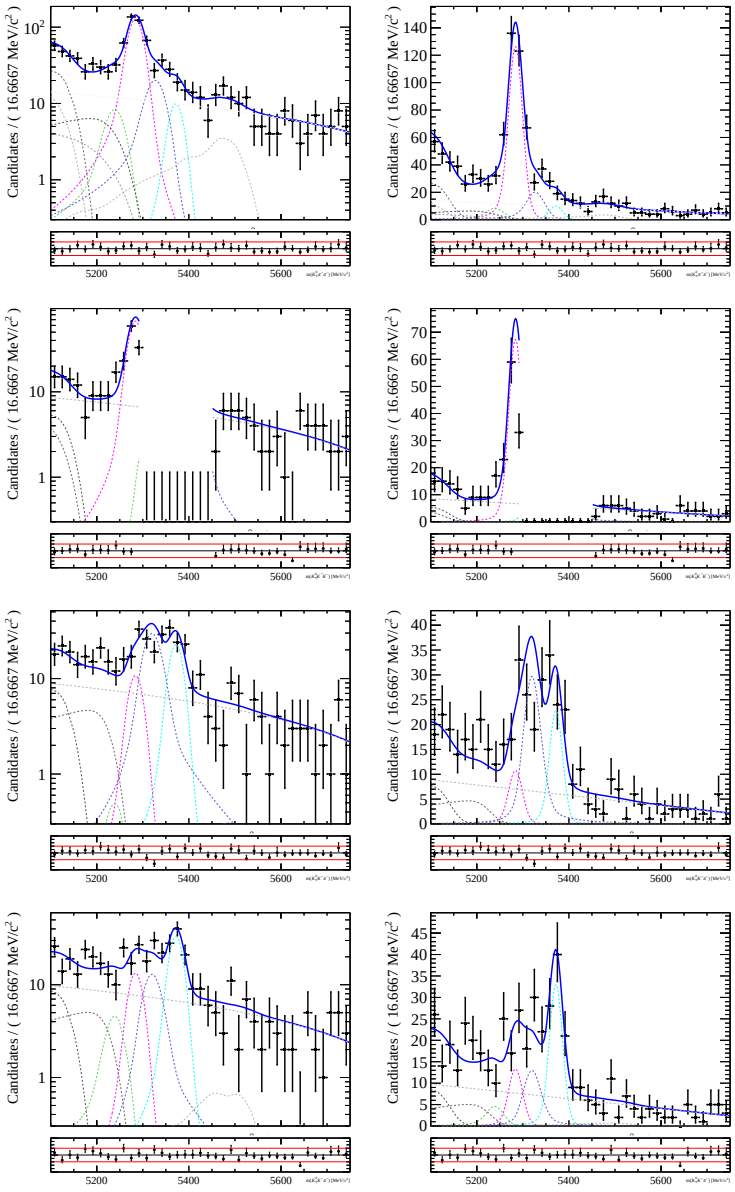

Figure B.12: Result of the simultaneous fit to the data. We show here the results on 2011, LL. The selection has been optimised on the principal signal peak. From top to bottom, $K^0_S\pi^+\pi^-$, $K^0_S K^+K^-$, $K^0_S K^+\pi^-$ and $K^0_S\pi^+K^-$ are shown. The left-hand-side plots have a logarithmic scale, and the plots on the right show the same data on a linear scale. The magenta dashed line is the B^0 signal contribution. The B^0_s signal peak is in cyan. The crossfeed backgrounds are the blue and green dashe lines. The grey dashed line peaking above 5400 MeV is the Λ_b crossfeed background. To the left of the plot, the grey dashed lines illustrate the partially reconstructed background contributions and the combinatorial background is the grey straight line. In the $K^0_S K^+K^-$ spectra, the region around the B^0_s signal (5320-5450 MeV) is blinded.

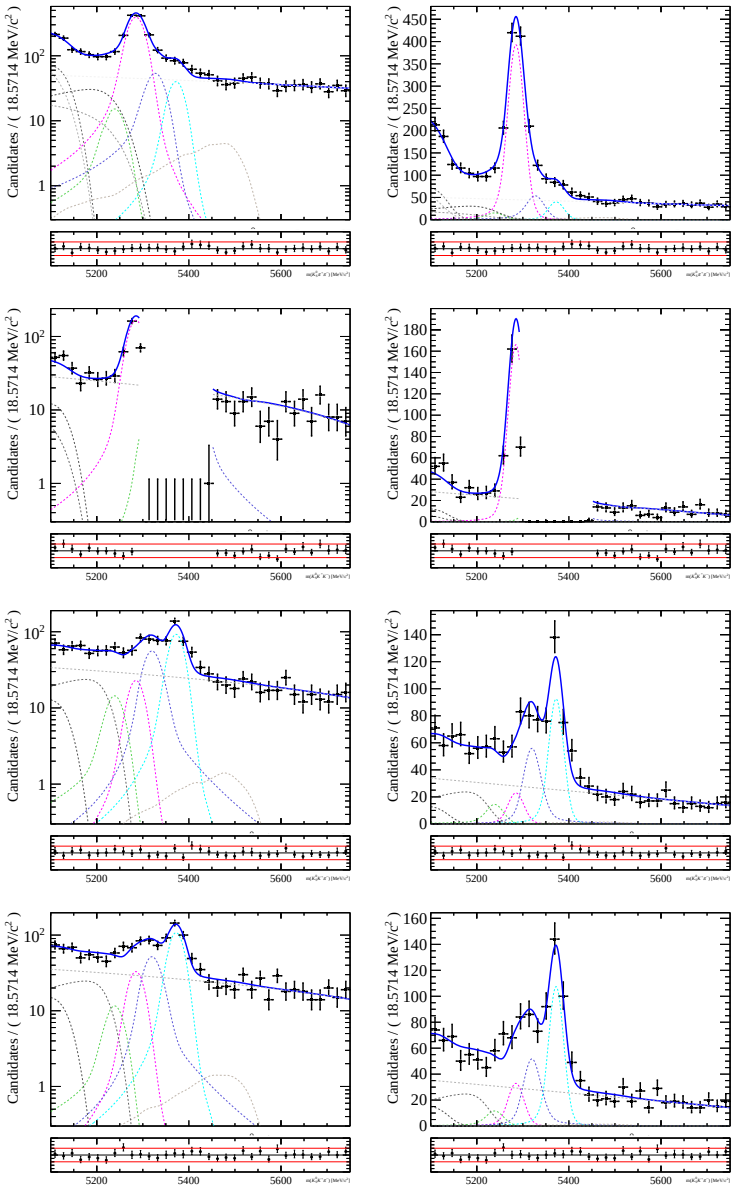

Figure B.13: Result of the simultaneous fit to the data. We show here the results on 2011, DD. The selection has been optimised on the principal signal peak. From top to bottom, $K^0_S\pi^+\pi^-$, $K^0_S K^+K^-$, $K^0_S K^+\pi^-$ and $K^0_S\pi^+K^-$ are shown. The left-hand-side plots have a logarithmic scale, and the plots on the right show the same data on a linear scale. The magenta dashed line is the B^0 signal contribution. The B^0_s signal peak is in cyan. The crossfeed backgrounds are the blue and green dashe lines. The grey dashed line peaking above 5400 MeV is the Λ_b crossfeed background. To the left of the plot, the grey dashed lines illustrate the partially reconstructed background contributions and the combinatorial background is the grey straight line. In the $K^0_S K^+K^-$ spectra, the region around the B^0_s signal (5320-5450 MeV) is blinded.

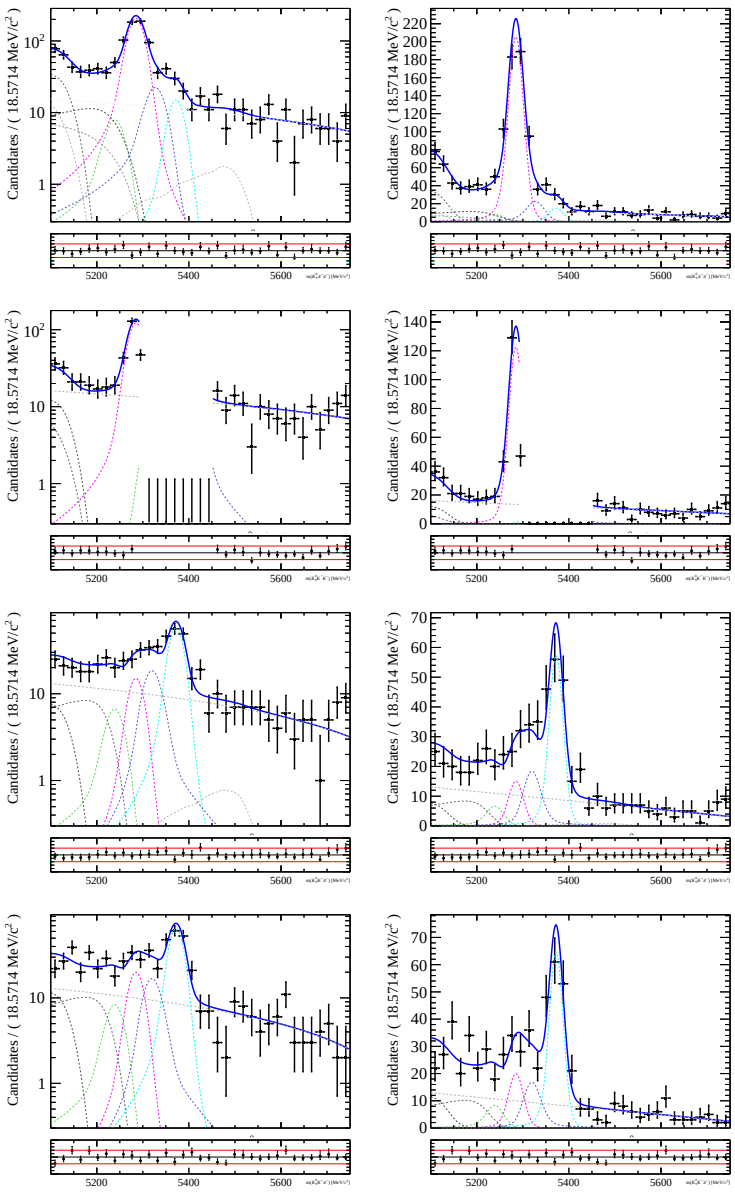

Figure B.14: Result of the simultaneous fit to the data. We show here the results on 2011, LL. The selection has been optimised on the principal signal peak. From top to bottom, $K^0_S\pi^+\pi^-$, $K^0_S K^+K^-$, $K^0_S K^+\pi^-$ and $K^0_S\pi^+K^-$ are shown. The left-hand-side plots have a logarithmic scale, and the plots on the right show the same data on a linear scale. The magenta dashed line is the B^0 signal contribution. The B^0_s signal peak is in cyan. The crossfeed backgrounds are the blue and green dashe lines. The grey dashed line peaking above 5400 MeV is the Λ_b crossfeed background. To the left of the plot, the grey dashed lines illustrate the partially reconstructed background contributions and the combinatorial background is the grey straight line. In the $K^0_S K^+K^-$ spectra, the region around the B^0_s signal (5320-5450 MeV) is blinded.

Systematic uncertainties for each category in the case of the selection optimised on the B^0 signal									
Category	Yield	Stat.	Sig.p.	P.R. p.	P.R. eff.	P.R. BR	Sig.m.	Comb.m.	Λ_b m.
N($B^0 \to K^0_S K^+\pi^-$)(DD)(2011)	52	12	0	1	2	3	5	3	1
N($B^0 \to K^0_S K^+\pi^-$)(DD)(2012a)	36	8	0	0	2	2	3	3	0
N($B^0 \to K^0_S K^+\pi^-$)(DD)(2012b)	90	13	0	1	3	4	11	6	3
N($B^0 \to K^0_S K^+\pi^-$)(DD)(2015)	68	11	0	1	1	3	8	5	4
N($B^0 \to K^0_S K^+\pi^-$)(DD)(2016)	372	30	1	1	4	8	40	30	1
N($B^0 \to K^0_S K^+\pi^-$)(DD)(2017)	421	33	1	1	4	9	48	38	4
N($B^0 \to K^0_S K^+\pi^-$)(DD)(2018)	458	32	1	1	4	9	59	43	15
N($B^0 \to K^0_S K^+\pi^-$)(LL)(2011)	32	8	0	0	2	2	4	5	2
N($B^0 \to K^0_S K^+\pi^-$)(LL)(2012a)	13	4	0	0	1	1	0	1	0
N($B^0 \to K^0_S K^+\pi^-$)(LL)(2012b)	36	9	0	0	2	2	3	2	0
N($B^0 \to K^0_S K^+\pi^-$)(LL)(2015)	33	8	0	0	2	2	5	4	0
N($B^0 \to K^0_S K^+\pi^-$)(LL)(2016)	107	16	0	1	3	5	12	13	0
N($B^0 \to K^0_S K^+\pi^-$)(LL)(2017)	138	18	0	1	3	5	20	13	1
N($B^0 \to K^0_S K^+\pi^-$)(LL)(2018)	193	21	0	1	4	6	25	14	0

Table I: This tables contains the yield, the statistical uncertainties and the systematic uncertainties related to the fit process for the $B^0 \to K^0_S K^+\pi^-$ decays. In general, the statistical uncertainty and the systematic uncertainties related to the choice in the signal and combinatorial background models are the dominant uncertainties.

- Fixed partially reconstructed background shape parameters (P.R. p.)
- Fixed partially reconstructed background efficiency ratios (P.R. eff.)
- Fixed partially reconstructed background branching fraction ratios (P.R. BR)
- Choice in the signal model (Sig. m.)
- Choice in the combinatorial background model (Comb. m.)
- Choice in the Λ_b crossfeed model (Λ_b m.)

In general, the statistical uncertainty and the systematic uncertainties related to the choice in the signal and combinatorial background models are the dominant uncertainties.

Systematic uncertainties for each category in the case of the selection optimised on the B^0 signal									
Category	Yield	Stat.	Sig.p.	P.R. p.	P.R. eff.	P.R. BR	Sig.m.	Comb.m.	Λ_b m.
N($B^0 \to K^0_S\pi^+K^-$)(DD)(2011)	79	12	0	1	2	3	10	2	1
N($B^0 \to K^0_S\pi^+K^-$)(DD)(2012a)	21	8	0	0	1	2	3	3	0
N($B^0 \to K^0_S\pi^+K^-$)(DD)(2012b)	113	16	1	1	2	4	7	9	2
N($B^0 \to K^0_S\pi^+K^-$)(DD)(2015)	60	14	0	1	1	4	6	11	3
N($B^0 \to K^0_S\pi^+K^-$)(DD)(2016)	348	30	1	1	3	8	34	29	0
N($B^0 \to K^0_S\pi^+K^-$)(DD)(2017)	382	28	1	1	3	7	29	23	9
N($B^0 \to K^0_S\pi^+K^-$)(DD)(2018)	430	30	1	1	3	8	27	40	17
N($B^0 \to K^0_S\pi^+K^-$)(LL)(2011)	37	9	0	0	1	2	2	5	0
N($B^0 \to K^0_S\pi^+K^-$)(LL)(2012a)	15	5	0	0	1	1	0	2	1
N($B^0 \to K^0_S\pi^+K^-$)(LL)(2012b)	42	8	0	0	1	2	3	5	0
N($B^0 \to K^0_S\pi^+K^-$)(LL)(2015)	29	8	0	0	1	2	5	1	0
N($B^0 \to K^0_S\pi^+K^-$)(LL)(2016)	179	20	0	1	1	5	17	15	0
N($B^0 \to K^0_S\pi^+K^-$)(LL)(2017)	171	20	0	1	1	5	22	13	2
N($B^0 \to K^0_S\pi^+K^-$)(LL)(2018)	188	20	0	1	1	6	26	19	0

Table II: This tables contains the yield, the statistical uncertainties and the systematic uncertainties related to the fit process for the $B^0 \to K^0_S\pi^+K^-$ decays. In general, the statistical uncertainty and the systematic uncertainties related to the choice in the signal and combinatorial background models are the dominant uncertainties.

Systematic uncertainties for each category in the case of the selection optimised on the B^0 signal									
Category	Yield	Stat.	Sig.p.	P.R. p.	P.R. eff.	P.R. BR	Sig.m.	Comb.m.	Λ_b m.
N($B^0 \to K^0_S\pi^+\pi^-$)(DD)(2011)	1085	42	1	2	5	10	64	20	3
N($B^0 \to K^0_S\pi^+\pi^-$)(DD)(2012a)	721	34	1	1	5	8	2	29	2
N($B^0 \to K^0_S\pi^+\pi^-$)(DD)(2012b)	1865	56	11	2	7	13	49	28	6
N($B^0 \to K^0_S\pi^+\pi^-$)(DD)(2015)	969	42	1	2	5	9	23	15	4
N($B^0 \to K^0_S\pi^+\pi^-$)(DD)(2016)	5911	101	32	3	10	23	173	94	24
N($B^0 \to K^0_S\pi^+\pi^-$)(DD)(2017)	6627	107	5	3	9	24	66	106	24
N($B^0 \to K^0_S\pi^+\pi^-$)(DD)(2018)	8252	121	7	4	10	28	125	94	33
N($B^0 \to K^0_S\pi^+\pi^-$)(LL)(2011)	526	28	1	1	4	6	1	12	1
N($B^0 \to K^0_S\pi^+\pi^-$)(LL)(2012a)	345	23	0	1	3	5	6	4	1
N($B^0 \to K^0_S\pi^+\pi^-$)(LL)(2012b)	768	35	5	1	5	8	7	23	2
N($B^0 \to K^0_S\pi^+\pi^-$)(LL)(2015)	467	27	0	1	4	6	8	4	1
N($B^0 \to K^0_S\pi^+\pi^-$)(LL)(2016)	2696	65	15	2	7	15	55	69	10
N($B^0 \to K^0_S\pi^+\pi^-$)(LL)(2017)	2816	66	2	2	7	16	52	67	8
N($B^0 \to K^0_S\pi^+\pi^-$)(LL)(2018)	3155	70	3	2	7	16	54	72	9

Table III: This tables contains the yield, the statistical uncertainties and the systematic uncertainties related to the fit process for the $B^0 \to K^0_S\pi^+\pi^-$ decays. In general, the statistical uncertainty and the systematic uncertainties related to the choice in the signal and combinatorial background models are the dominant uncertainties.

Systematic uncertainties for each category in the case of the selection optimised on the B^0 signal									
Category	Yield	Stat.	Sig.p.	P.R. p.	P.R. eff.	P.R. BR	Sig.m.	Comb.m.	Λ_b m.
N($B^0_s \to K^0_S K^+\pi^-$)(DD)(2011)	184	16	0	1	2	4	2	2	1
N($B^0_s \to K^0_S K^+\pi^-$)(DD)(2012a)	103	11	0	0	2	3	5	3	0
N($B^0_s \to K^0_S K^+\pi^-$)(DD)(2012b)	331	20	0	1	3	4	14	5	3
N($B^0_s \to K^0_S K^+\pi^-$)(DD)(2015)	146	14	0	0	1	3	11	4	3
N($B^0_s \to K^0_S K^+\pi^-$)(DD)(2016)	1194	42	1	1	4	9	76	24	2
N($B^0_s \to K^0_S K^+\pi^-$)(DD)(2017)	1319	44	1	1	4	9	99	26	4
N($B^0_s \to K^0_S K^+\pi^-$)(DD)(2018)	1471	46	1	1	5	10	115	31	12
N($B^0_s \to K^0_S K^+\pi^-$)(LL)(2011)	117	12	0	0	2	3	1	4	2
N($B^0_s \to K^0_S K^+\pi^-$)(LL)(2012a)	43	7	0	0	1	2	1	1	0
N($B^0_s \to K^0_S K^+\pi^-$)(LL)(2012b)	124	13	0	0	2	3	3	2	0
N($B^0_s \to K^0_S K^+\pi^-$)(LL)(2015)	90	11	0	0	2	2	8	3	0
N($B^0_s \to K^0_S K^+\pi^-$)(LL)(2016)	468	25	0	1	3	6	26	7	0
N($B^0_s \to K^0_S K^+\pi^-$)(LL)(2017)	534	27	1	1	3	6	46	8	1
N($B^0_s \to K^0_S K^+\pi^-$)(LL)(2018)	643	30	1	1	4	6	59	12	0

Table IV: This tables contains the yield, the statistical uncertainties and the systematic uncertainties related to the fit process for the $B^0_s \to K^0_S K^+\pi^-$ decays. In general, the statistical uncertainty and the systematic uncertainties related to the choice in the signal and combinatorial background models are the dominant uncertainties.

Systematic uncertainties for each category in the case of the selection optimised on the B^0 signal									
Category	Yield	Stat.	Sig.p.	P.R. p.	P.R. eff.	P.R. BR	Sig.m.	Comb.m.	Λ_b m.
N($B^0_s \to K^0_S \pi^+ K^-$)(DD)(2011)	170	15	0	0	1	3	3	1	1
N($B^0_s \to K^0_S \pi^+ K^-$)(DD)(2012a)	127	13	0	0	1	3	5	4	0
N($B^0_s \to K^0_S \pi^+ K^-$)(DD)(2012b)	345	22	1	1	2	5	11	6	1
N($B^0_s \to K^0_S \pi^+ K^-$)(DD)(2015)	230	19	0	1	2	4	21	10	2
N($B^0_s \to K^0_S \pi^+ K^-$)(DD)(2016)	1173	42	1	1	3	9	67	22	1
N($B^0_s \to K^0_S \pi^+ K^-$)(DD)(2017)	1268	41	1	1	3	8	79	19	7
N($B^0_s \to K^0_S \pi^+ K^-$)(DD)(2018)	1423	44	1	1	3	9	88	32	13
N($B^0_s \to K^0_S \pi^+ K^-$)(LL)(2011)	106	12	0	0	1	2	1	2	0
N($B^0_s \to K^0_S \pi^+ K^-$)(LL)(2012a)	44	7	0	0	1	1	0	1	1
N($B^0_s \to K^0_S \pi^+ K^-$)(LL)(2012b)	122	12	0	0	1	3	3	3	0
N($B^0_s \to K^0_S \pi^+ K^-$)(LL)(2015)	100	12	0	0	1	3	12	1	0
N($B^0_s \to K^0_S \pi^+ K^-$)(LL)(2016)	581	28	0	1	2	6	31	7	1
N($B^0_s \to K^0_S \pi^+ K^-$)(LL)(2017)	594	28	1	1	2	6	49	8	2
N($B^0_s \to K^0_S \pi^+ K^-$)(LL)(2018)	618	29	0	1	2	6	57	14	0

Table V: This tables contains the yield, the statistical uncertainties and the systematic uncertainties related to the fit process for the $B^0_s \to K^0_S \pi^+ K^-$ decays. In general, the statistical uncertainty and the systematic uncertainties related to the choice in the signal and combinatorial background models are the dominant uncertainties.

Systematic uncertainties for each category in the case of the selection optimised on the B^0 signal									
Category	Yield	Stat.	Sig.p.	P.R. p.	P.R. eff.	P.R. BR	Sig.m.	Comb.m.	Λ_b m.
N($B_s^0 \to K_S^0\pi^+\pi^-$)(DD)(2011)	106	20	0	1	4	7	2	12	2
N($B_s^0 \to K_S^0\pi^+\pi^-$)(DD)(2012a)	49	16	0	1	3	5	6	17	1
N($B_s^0 \to K_S^0\pi^+\pi^-$)(DD)(2012b)	230	28	2	1	5	9	11	14	2
N($B_s^0 \to K_S^0\pi^+\pi^-$)(DD)(2015)	32	21	0	1	4	7	17	2	2
N($B_s^0 \to K_S^0\pi^+\pi^-$)(DD)(2016)	533	52	3	1	6	16	15	40	10
N($B_s^0 \to K_S^0\pi^+\pi^-$)(DD)(2017)	466	52	2	1	6	15	86	45	9
N($B_s^0 \to K_S^0\pi^+\pi^-$)(DD)(2018)	735	62	2	2	7	18	111	28	13
N($B_s^0 \to K_S^0\pi^+\pi^-$)(LL)(2011)	39	11	0	0	2	4	9	5	1
N($B_s^0 \to K_S^0\pi^+\pi^-$)(LL)(2012a)	26	10	0	0	2	3	2	0	0
N($B_s^0 \to K_S^0\pi^+\pi^-$)(LL)(2012b)	69	17	1	1	4	5	9	12	1
N($B_s^0 \to K_S^0\pi^+\pi^-$)(LL)(2015)	44	13	0	1	3	4	2	3	1
N($B_s^0 \to K_S^0\pi^+\pi^-$)(LL)(2016)	204	31	1	1	4	10	17	30	3
N($B_s^0 \to K_S^0\pi^+\pi^-$)(LL)(2017)	212	29	1	1	4	10	11	32	3
N($B_s^0 \to K_S^0\pi^+\pi^-$)(LL)(2018)	268	32	1	1	5	11	9	34	4

Table VI: This tables contains the yield, the statistical uncertainties and the systematic uncertainties related to the fit process for the $B_s^0 \to K_S^0\pi^+\pi^-$ decays. In general, the statistical uncertainty and the systematic uncertainties related to the choice in the signal and combinatorial background models are the dominant uncertainties.

Bibliography

[1] **ATLAS** Collaboration, G. Aad *et al.*, "Observation of a new particle in the search for the Standard Model Higgs boson with the ATLAS detector at the LHC," *Phys. Lett. B* **716** (2012) 1–29, arXiv:1207.7214 [hep-ex].

[2] **CMS** Collaboration, S. Chatrchyan *et al.*, "Observation of a New Boson at a Mass of 125 GeV with the CMS Experiment at the LHC," *Phys. Lett. B* **716** (2012) 30–61, arXiv:1207.7235 [hep-ex].

[3] **BaBar** Collaboration, J. P. Lees *et al.*, "Measurement of Branching Fractions and Rate Asymmetries in the Rare Decays $B \to K^{(*)}\ell^+\ell^-$," *Phys. Rev. D* **86** (2012) 032012, arXiv:1204.3933 [hep-ex].

[4] **Belle** Collaboration, J. T. Wei *et al.*, "Measurement of the Differential Branching Fraction and Forward-Backward Asymmetry for $B \to K^{(*)}\ell^+\ell^-$," *Phys. Rev. Lett.* **103** (2009) 171801, arXiv:0904.0770 [hep-ex].

[5] **LHCb** Collaboration, R. Aaij *et al.*, "Test of lepton universality using $B^+ \to K^+\ell^+\ell^-$ decays," *Phys. Rev. Lett.* **113** (2014) 151601, arXiv:1406.6482 [hep-ex].

[6] **HFLAV** Collaboration, Y. S. Amhis *et al.*, "Averages of b-hadron, c-hadron, and τ-lepton properties as of 2018," *Eur. Phys. J.* **C81** (2021) 226, arXiv:1909.12524 [hep-ex]. updated results and plots available at https://hflav.web.cern.ch/.

[7] **LHCb** Collaboration, R. Aaij *et al.*, "Tests of lepton universality using $B^0 \to K^0_S\ell^+\ell^-$ and $B^+ \to K^{*+}\ell^+\ell^-$ decays," arXiv:2110.09501 [hep-ex].

[8] **LHCb** Collaboration, R. Aaij *et al.*, "Test of lepton universality in beauty-quark decays," arXiv:2103.11769 [hep-ex].

[9] **LHCb** Collaboration, R. Aaij *et al.*, "Amplitude analysis of $B^0_s \to K^0_S K^\pm \pi^\mp$ decays," *JHEP* **06** (2019) 114, arXiv:1902.07955 [hep-ex].

[10] **LHCb** Collaboration, R. Aaij *et al.*, "Updated branching fraction measurements of $B^0_{(s)} \to K^0_S h^+ h'^-$ decays," *JHEP* **11** (2017) 027, arXiv:1707.01665 [hep-ex].

[11] **LHCb** Collaboration, R. Aaij *et al.*, "Amplitude analysis of the $B^+ \to \pi^+\pi^+\pi^-$ decay," *Phys. Rev. D* **101** no. 1, (2020) 012006, arXiv:1909.05212 [hep-ex].

[12] **LHCb** Collaboration, R. Aaij *et al.*, "Observation of Several Sources of CP Violation in $B^+ \to \pi^+\pi^+\pi^-$ Decays," *Phys. Rev. Lett.* **124** no. 3, (2020) 031801, arXiv:1909.05211 [hep-ex].

[13] M. Gronau and D. London, "How to determine all the angles of the unitarity triangle from $B^0_{(d)} \to DK_{(s)}$ and $B^0_{(s)} \to D^0$," *Phys. Lett. B* **253** (1991) 483–488.

[14] D. Atwood, I. Dunietz, and A. Soni, "Enhanced CP violation with $B \to KD^0$ (anti-D^0) modes and extraction of the CKM angle γ," *Phys. Rev. Lett.* **78** (1997) 3257–3260, arXiv:hep-ph/9612433.

[15] B. Bhattacharya, M. Imbeault, and D. London, "Extraction of the CP-violating phase γ using $B \to K\pi\pi$ and $B \to KK\bar{K}$ decays," *Phys. Lett. B* **728** (2014) 206–209, arXiv:1303.0846 [hep-ph].

[16] E. Bertholet, E. Ben-Haim, B. Bhattacharya, M. Charles, and D. London, "Extraction of the CKM phase γ using charmless 3-body decays of B mesons," *Phys. Rev. D* **99** no. 11, (2019) 114011, arXiv:1812.06194 [hep-ph].

[17] R. H. Dalitz and S. F. Tuan, "The phenomenological description of -K -nucleon reaction processes," *Annals Phys.* **10** (1960) 307–351.

[18] I. J. R. Aitchison, "K-matrix formalism for overlapping resonances," *Nucl. Phys. A* **189** (1972) 417–423.

[19] S. U. Chung, J. Brose, R. Hackmann, E. Klempt, S. Spanier, and C. Strassburger, "Partial wave analysis in K matrix formalism," *Annalen Phys.* **4** (1995) 404–430.

[20] **FOCUS** Collaboration, J. M. Link *et al.*, "The $K^-\pi^+$ S-wave from the $D^+ \to K^-\pi^+\pi^+$ decay," *Phys. Lett. B* **681** (2009) 14–21, arXiv:0905.4846 [hep-ex].

[21] **E791** Collaboration, E. M. Aitala *et al.*, "Model independent measurement of S-wave $K^-\pi^+$ systems using $D^+ \to K\pi\pi$ decays from Fermilab E791," *Phys. Rev. D* **73** (2006) 032004, arXiv:hep-ex/0507099. [Erratum: Phys.Rev.D 74, 059901 (2006)].

[22] **CLEO** Collaboration, G. Bonvicini *et al.*, "Dalitz plot analysis of the $D^+ \to K^-\pi^+\pi^+$ decay," *Phys. Rev. D* **78** (2008) 052001, arXiv:0802.4214 [hep-ex].

[23] **BaBar** Collaboration, B. Aubert *et al.*, "Dalitz Plot Analysis of $D_s+ \to \pi^+\pi^-\pi^+$," *Phys. Rev. D* **79** (2009) 032003, arXiv:0808.0971 [hep-ex].

[24] **BaBar** Collaboration, P. del Amo Sanchez *et al.*, "Analysis of the $D^+ \to K^-\pi^+e^+\nu_e$ decay channel," *Phys. Rev. D* **83** (2011) 072001, arXiv:1012.1810 [hep-ex].

[25] E. Schrödinger, "An undulatory theory of the mechanics of atoms and molecules," *Phys. Rev.* **28** (Dec, 1926) 1049–1070.

[26] N. Cabibbo, "Unitary Symmetry and Leptonic Decays," *Phys. Rev. Lett.* **10** (1963) 531–533.

[27] M. Kobayashi and T. Maskawa, "CP Violation in the Renormalizable Theory of Weak Interaction," *Prog. Theor. Phys.* **49** (1973) 652–657.

[28] **CKMfitter Group** Collaboration, J. Charles, A. Hocker, H. Lacker, S. Laplace, F. R. Le Diberder, J. Malcles, J. Ocariz, M. Pivk, and L. Roos, "CP violation and the CKM matrix: Assessing the impact of the asymmetric B factories," *Eur. Phys. J. C* **41** no. 1, (2005) 1–131, arXiv:hep-ph/0406184.

[29] C. S. Wu, E. Ambler, R. W. Hayward, D. D. Hoppes, and R. P. Hudson, "Experimental Test of Parity Conservation in β Decay," *Phys. Rev.* **105** (1957) 1413–1414.

[30] T. D. Lee and C.-N. Yang, "Question of Parity Conservation in Weak Interactions," *Phys. Rev.* **104** (1956) 254–258.

[31] J. H. Christenson, J. W. Cronin, V. L. Fitch, and R. Turlay, "Evidence for the 2π Decay of the K_2^0 Meson," *Phys. Rev. Lett.* **13** (1964) 138–140.

[32] R. H. Dalitz, "The decay of the tau-meson," *Proc. Phys. Soc. A* **66** (1953) 710–713.

[33] E. Fabri, "A study of tau-meson decay," *Nuovo Cim.* **11** (1954) 479–491.

[34] R. M. Sternheimer and S. J. Lindenbaum, "Extension of the Isobaric Nucleon Model for Pion Production in Pion-Nucleon, Nucleon-Nucleon, and Antinucleon-Nucleon Interactions," *Phys. Rev.* **123** (1961) 333–376.

[35] D. Herndon, P. Soding, and R. J. Cashmore, "A generalized isobar model formalism," *Phys. Rev. D* **11** (1975) 3165.

[36] C. Zemach, "Determination of the Spins and Parities of Resonances," *Phys. Rev.* **140** (1965) B109–B124.

[37] G. Breit and E. Wigner, "Capture of Slow Neutrons," *Phys. Rev.* **49** (1936) 519–531.

[38] G. J. Gounaris and J. J. Sakurai, "Finite width corrections to the vector meson dominance prediction for $\rho \to e^+e^-$," *Phys. Rev. Lett.* **21** (1968) 244–247.

[39] S. M. Flatte, "Coupled - Channel Analysis of the pi eta and K anti-K Systems Near K anti-K Threshold," *Phys. Lett. B* **63** (1976) 224–227.

[40] J. M. Blatt and V. F. Weisskopf, *Theoretical nuclear physics*. Springer, New York, 1952.

[41] A. Giri, Y. Grossman, A. Soffer, and J. Zupan, "Determining gamma using $B^\pm \to DK^\pm$ with multibody D decays," *Phys. Rev. D* **68** (2003) 054018, `arXiv:hep-ph/0303187`.

[42] M. Gronau, O. F. Hernandez, D. London, and J. L. Rosner, "Electroweak penguins and two-body B decays," *Phys. Rev. D* **52** (1995) 6374–6382, `arXiv:hep-ph/9504327`.

[43] N. R.-L. Lorier, M. Imbeault, and D. London, "Diagrammatic Analysis of Charmless Three-Body B Decays," *Phys. Rev. D* **84** (2011) 034040, `arXiv:1011.4972 [hep-ph]`.

[44] K. G. Wilson, "The Renormalization Group and Strong Interactions," *Phys. Rev. D* **3** (1971) 1818.

[45] N. R.-L. Lorier, M. Imbeault, and D. London, "Diagrammatic Analysis of Charmless Three-Body B Decays," *Phys. Rev. D* **84** (2011) 034040, arXiv:1011.4972 [hep-ph].

[46] **BaBar** Collaboration, J. P. Lees *et al.*, "Study of CP violation in Dalitz-plot analyses of $B^0 \to K^+K^-K^0_{(S)}$, $B^+ \to K^+K^-K^+$, and $B^+ \to K^0_{(S)}K^0_{(S)}K^+$," *Phys. Rev. D* **85** (2012) 112010, arXiv:1201.5897 [hep-ex].

[47] **BaBar** Collaboration, J. P. Lees *et al.*, "Amplitude Analysis of $B^0 \to K^+\pi^-\pi^0$ and Evidence of Direct CP Violation in $B \to K^*\pi$ decays," *Phys. Rev. D* **83** (2011) 112010, arXiv:1105.0125 [hep-ex].

[48] **BaBar** Collaboration, B. Aubert *et al.*, "Time-dependent amplitude analysis of $B^0 \to K^0_{(S)}\pi^+\pi^-$," *Phys. Rev. D* **80** (2009) 112001, arXiv:0905.3615 [hep-ex].

[49] **BaBar** Collaboration, B. Aubert *et al.*, "Evidence for Direct CP Violation from Dalitz-plot analysis of $B^\pm \to K^\pm\pi^\mp\pi^\pm$," *Phys. Rev. D* **78** (2008) 012004, arXiv:0803.4451 [hep-ex].

[50] **BaBar** Collaboration, J. P. Lees *et al.*, "Evidence for CP violation in $B^+ \to K^*(892)^+\pi^0$ from a Dalitz plot analysis of $B^+ \to K^0_S\pi^+\pi^0$ decays," *Phys. Rev. D* **96** no. 7, (2017) 072001, arXiv:1501.00705 [hep-ex].

[51] J. Back *et al.*, "LAURA^{++}: A Dalitz plot fitter," *Comput. Phys. Commun.* **231** (2018) 198–242, arXiv:1711.09854 [hep-ex].

[52] R. J. Barlow, *Statistics: A Guide to the Use of Statistical Methods in the Physical Sciences*. Wiley, 1989.

[53] "LHC Machine," *JINST* **3** (2008) S08001.

[54] E. Mobs, "The CERN accelerator complex - 2019. Complexe des accélérateurs du CERN - 2019,". General Photo.

[55] **ATLAS** Collaboration, G. Aad *et al.*, "The ATLAS Experiment at the CERN Large Hadron Collider," *JINST* **3** (2008) S08003.

[56] **CMS** Collaboration, S. Chatrchyan *et al.*, "The CMS Experiment at the CERN LHC," *JINST* **3** (2008) S08004.

[57] **ALICE** Collaboration, K. Aamodt *et al.*, "The ALICE experiment at the CERN LHC," *JINST* **3** (2008) S08002.

[58] **LHCb** Collaboration, A. A. Alves, Jr. *et al.*, "The LHCb Detector at the LHC," *JINST* **3** (2008) S08005.

[59] L. collaboration, "Lhcb reoptimized detector design and performance: Technical design report,".

[60] **LHCb** Collaboration, R. Aaij *et al.*, "Measurement of the track reconstruction efficiency at LHCb," *JINST* **10** no. 02, (2015) P02007, arXiv:1408.1251 [hep-ex].

[61] R. Aaij *et al.*, "Performance of the LHCb Vertex Locator," *JINST* **9** (2014) P09007, arXiv:1405.7808 [physics.ins-det].

[62] R. Aaij *et al.*, "Performance of the LHCb Vertex Locator," *JINST* **9** (2014) P09007, arXiv:1405.7808 [physics.ins-det].

[63] **LHCb Collaboration** Collaboration, L. Collaboration, *LHCb inner tracker: Technical Design Report*. Technical design report. LHCb. CERN, Geneva, 2002. revised version number 1 submitted on 2002-11-13 14:14:34.

[64] **LHCb Collaboration** Collaboration, L. Collaboration, *LHCb outer tracker: Technical Design Report*. Technical design report. LHCb. CERN, Geneva, 2001.

[65] **LHCb Outer Tracker Group** Collaboration, R. Arink *et al.*, "Performance of the LHCb Outer Tracker," *JINST* **9** no. 01, (2014) P01002, arXiv:1311.3893 [physics.ins-det].

[66] **LHCb** Collaboration, R. Aaij *et al.*, "Design and performance of the LHCb trigger and full real-time reconstruction in Run 2 of the LHC," *JINST* **14** no. 04, (2019) P04013, arXiv:1812.10790 [hep-ex].

[67] **LHCb RICH Group** Collaboration, M. Adinolfi *et al.*, "Performance of the LHCb RICH detector at the LHC," *Eur. Phys. J. C* **73** (2013) 2431, arXiv:1211.6759 [physics.ins-det].

[68] M. Williams, V. Gligorov, C. Thomas, H. Dijkstra, J. Nardulli, and P. Spradlin, "The HLT2 Topological Lines," tech. rep., 1, 2011.

[69] T. Sjostrand, S. Mrenna, and P. Z. Skands, "A Brief Introduction to PYTHIA 8.1," *Comput. Phys. Commun.* **178** (2008) 852–867, arXiv:0710.3820 [hep-ph].

[70] **LHCb** Collaboration, I. Belyaev *et al.*, "Handling of the generation of primary events in Gauss, the LHCb simulation framework," *J. Phys. Conf. Ser.* **331** (2011) 032047.

[71] D. J. Lange, "The EvtGen particle decay simulation package," *Nucl. Instrum. Meth. A* **462** (2001) 152–155.

[72] P. Golonka and Z. Was, "PHOTOS Monte Carlo: A Precision tool for QED corrections in Z and W decays," *Eur. Phys. J. C* **45** (2006) 97–107, arXiv:hep-ph/0506026.

[73] **GEANT4** Collaboration, S. Agostinelli *et al.*, "GEANT4–a simulation toolkit," *Nucl. Instrum. Meth. A* **506** (2003) 250–303.

[74] J. Allison *et al.*, "Geant4 developments and applications," *IEEE Trans. Nucl. Sci.* **53** (2006) 270.

[75] **LHCb** Collaboration, M. Clemencic, G. Corti, S. Easo, C. R. Jones, S. Miglioranzi, M. Pappagallo, and P. Robbe, "The LHCb simulation application, Gauss: Design, evolution and experience," *J. Phys. Conf. Ser.* **331** (2011) 032023.

[76] **LHCb** Collaboration, R. Aaij *et al.*, "Test of lepton universality in beauty-quark decays," arXiv:2103.11769 [hep-ex].

[77] **LHCb** Collaboration, R. Aaij *et al.*, "Measurement of CP Violation in the Decay $B^+ \to K^+\pi^0$," *Phys. Rev. Lett.* **126** no. 9, (2021) 091802, arXiv:2012.12789 [hep-ex].

[78] **LHCb** Collaboration, R. Aaij *et al.*, "Measurement of the $B^0_s \to \mu^+\mu^-$ decay properties and search for the $B^0 \to \mu^+\mu^-$ and $B^0_s \to \mu^+\mu^-\gamma$ decays," arXiv:2108.09283 [hep-ex].

[79] **LHCb** Collaboration, R. Aaij *et al.*, "Observation of CP Violation in Charm Decays," *Phys. Rev. Lett.* **122** no. 21, (2019) 211803, arXiv:1903.08726 [hep-ex].

[80] **LHCb** Collaboration, "LHCb Tracker Upgrade Technical Design Report,".

[81] **LHCb** Collaboration, R. Aaij *et al.*, "Physics case for an LHCb Upgrade II - Opportunities in flavour physics, and beyond, in the HL-LHC era," tech. rep., 8, 2018. arXiv:1808.08865 [hep-ex].

[82] L. Witola, "Calibration and performance studies of thereadout ASIC for the LHCb SciFi Tracker,".

[83] V. V. Gligorov, C. Thomas, and M. Williams, "The HLT inclusive B triggers," tech. rep., 9, 2011.

[84] R. Aaij *et al.*, "The LHCb Trigger and its Performance in 2011," *JINST* **8** (2013) P04022, arXiv:1211.3055 [hep-ex].

[85] W. D. Hulsbergen, "Decay chain fitting with a Kalman filter," *Nucl. Instrum. Meth. A* **552** (2005) 566–575, arXiv:physics/0503191.

[86] E. Bertholet, "Search for new physics in charmless three-body decays of b mesons," 2019.

[87] T. Skwarnicki, *A study of the radiative CASCADE transitions between the Upsilon-Prime and Upsilon resonances*. PhD thesis, Cracow, INP, 1986.

[88] K. S. Cranmer, "Kernel estimation in high-energy physics," *Comput. Phys. Commun.* **136** (2001) 198–207, arXiv:hep-ex/0011057.

[89] M. Pivk and F. R. Le Diberder, "SPlot: A Statistical tool to unfold data distributions," *Nucl. Instrum. Meth. A* **555** (2005) 356–369, arXiv:physics/0402083.

[90] A. Rogozhnikov, "hep_ml ." https://arogozhnikov.github.io/hep_ml/index.html.

[91] **Particle Data Group** Collaboration, P. A. Zyla *et al.*, "Review of Particle Physics," *PTEP* **2020** no. 8, (2020) 083C01.

[92] **BaBar** Collaboration, P. del Amo Sanchez *et al.*, "Observation of the Rare Decay $B^0 \to K^0_{(s)} K^{\pm}\pi^{\mp}$," *Phys. Rev. D* **82** (2010) 031101, arXiv:1003.0640 [hep-ex].

[93] **Belle** Collaboration, Y. T. Lai *et al.*, "Measurement of branching fraction and final-state asymmetry for the $\bar{B}^0 \to K^0_S K^{\mp}\pi^{\pm}$ decay," *Phys. Rev. D* **100** no. 1, (2019) 011101, arXiv:1904.06835 [hep-ex].

[94] **BaBar** Collaboration, J. P. Lees *et al.*, "Study of CP violation in Dalitz-plot analyses of $B^0 \to K^+K^-K^0_{(S)}$, $B^+ \to K^+K^-K^+$, and $B^+ \to K^0_{(S)}K^0_{(S)}K^+$," *Phys. Rev. D* **85** (2012) 112010, arXiv:1201.5897 [hep-ex].

[95] **Belle** Collaboration, A. Garmash *et al.*, "Study of B meson decays to three body charmless hadronic final states," *Phys. Rev. D* **69** (2004) 012001, arXiv:hep-ex/0307082.